Optimal-transport analysis of single-cell gene expression sheds light on reprogramming

Geoffrey Schiebinger,[1,11,*] Jian Shu,[12,*,†] Marcin Tabaka,[1,*] Brian Cleary,[1,3,*] Vidya Subramanian,[1] Aryeh Solomon,[1,@] Joshua Gould,[1] Siyan Liu,[1,15] Stacie Lin,[1,6] Peter Berube,[1] Lia Lee,[1] Jenny Chen,[1,4] Justin Brumbaugh,[5,7,8,9,10] Philippe Rigollet,[11,12] Konrad Hochedlinger,[7,8,9,13] Rudolf Jaenisch,[2,3] Aviv Regev,[1,6,13,†] Eric S. Lander[1,6,14,†,#]

***These authors contributed equally to this work.**

[†]Corresponding author.

[#]Lead contact.

Email: lander@broadinstitute.org (E.S.L.), aregev@broadinstitute.org (A.R.); jianshu@broadinstitute.org (J.S.)

[1]Klarman Cell Observatory, Broad Institute of MIT and Harvard, Cambridge, MA 02142, USA

[2]Whitehead Institute for Biomedical Research, Cambridge, MA 02142, USA

[3]Computational and Systems Biology Program, MIT, Cambridge, MA 02142, USA

[4]Harvard-MIT Division of Health Sciences and Technology, Cambridge, MA 02139 USA

[5]Cancer Center, Massachusetts General Hospital, Boston, MA 02114 USA

[6]Department of Biology, Massachusetts Institute of Technology, Cambridge, MA 02139, USA

[7]Department of Molecular Biology, Center for Regenerative Medicine and Cancer Center, Massachusetts General Hospital, Boston, MA 02114, USA

[8]Department of Stem Cell and Regenerative Biology, Harvard University, Cambridge, MA 02138, USA

[9]Harvard Stem Cell Institute, Cambridge, MA 02138, USA

[10]Harvard Medical School, Boston, MA 02115, USA

[11]MIT Center for Statistics, Massachusetts Institute of Technology, Cambridge, MA 02139, USA

[12]Department of Mathematics, Massachusetts Institute of Technology, Cambridge, MA 02139, USA

[13]Howard Hughes Medical Institute, Chevy Chase, MD, USA

[14]Department of Systems Biology Harvard Medical School, Boston, MA 02125, USA

[15]Biochemistry Program, Wellesley College, Wellesley, 02481, MA, USA

Present Address: [@]Weizmann Institute of Science, Rehovot, Israel

Summary

Understanding the molecular programs that guide differentiation during development is a major challenge. Here, we introduce Waddington-OT, a new approach for studying developmental time courses to infer ancestor-descendant fates and model the regulatory programs that underlie them. We apply Waddington-OT to reconstruct the landscape of reprogramming from 315,000 scRNA-seq profiles, collected mostly at half-day intervals across 18 days. We reveal a wider range of developmental programs than previously characterized. Cells gradually adopt either a terminal stromal state or a mesenchymal-to-epithelial transition state. The latter gives rise to populations related to pluripotent, extra-embryonic, and neural cells, with each harboring multiple finer subpopulations. We predict transcription factors and paracrine signals that affect fates, and experimentally validate that the TF *Obox6* and the cytokine GDF9 enhance reprogramming efficiency. Our approach sheds new light on the process and outcome of reprogramming and provides a framework applicable to diverse temporal processes in biology.

Introduction

Waddington introduced two metaphors that shaped biological thinking about cellular differentiation: first, trains moving along branching railroad tracks and, later, marbles rolling through a developmental landscape (Waddington, 1936, 1957). Studying the actual landscapes, fates and trajectories associated with cellular differentiation and de-differentiation — in development, physiological responses, and reprogramming — requires us to answer questions such as: What classes of cells are present at each stage? What was their origin at earlier stages? What are their likely fates at later stages? What regulatory programs control their dynamics?

Approaches based on bulk analysis of cell populations are not well suited to address these questions, because they do not provide general solutions to two challenges: discovering cell classes in a population and tracing the development of each class.

The first challenge has been largely solved by the advent of single-cell RNA-Seq (scRNA-seq) (Tanay and Regev, 2017). The second remains a work-in-progress. Because scRNA-seq destroys cells in the course of recording their profiles, one cannot follow expression the same cell and its direct descendants across time. While various approaches can record information about cell lineage, they currently provide only very limited information about a cell's state at earlier time points (Kester and van Oudenaarden, 2018; McKenna et al., 2016).

Comprehensive studies of cell trajectories thus rely heavily on computational approaches to connect discrete 'snapshots' into continuous 'movies.' Pioneering work to infer trajectories (Saelens et al., 2018) has shed light on various biological systems, including whole-organism development (Briggs et al., 2018; Farrell et al., 2018; Fincher et al., 2018; Plass et al., 2018; Wagner et al., 2018), but many important challenges remain. First, with few exceptions (Lönnberg et al., 2017; Marco et al., 2014; Rashid et al., 2017; Wagner et al., 2018), most methods do not explicitly leverage temporal information in a time course. Historically, most were designed to extract information about stationary processes, such as adult stem cell differentiation, in which all stages exist simultaneously. However, time-courses are becoming commonplace. Second, many methods model trajectories in terms of graph theory, which imposes strong constraints on the model, such as one-dimensional trajectories ("edges") and zero-dimensional branch points ("nodes"). Thus, gradual divergence of fates is not captured well by these models (Briggs et al., 2018; Farrell et al., 2018; Wagner et al., 2018). Third, few methods (Weinreb et al., 2017) account for cellular growth and death during development.

Here, we describe a conceptual framework, implemented in a method called Waddington-OT, that aims to capture the notion that cells at any time are drawn from a probability distribution in gene-expression space, and each cell has a *distribution* of both probable origins and probable fates (**Figure 1**). It uses scRNA-seq data collected across a time-course to infer how these probability distributions evolve over time, by using the mathematical approach of Optimal Transport (OT).

We apply this framework to the challenge of understanding cellular reprogramming, following transient overexpression of a set of transcription factors (TFs) (Takahashi and Yamanaka, 2016). We aim to address questions such as: What classes of cells arise in reprogramming? What are the developmental paths that lead to reprogramming and to any alternative fates? Which cell intrinsic factors and cell-cell interactions drive progress along these paths? Can the information gleaned be used to improve the efficiency of reprogramming toward a desired destination?

Reprogramming of fibroblasts to induced pluripotent stem cells (iPSCs) (Takahashi and Yamanaka, 2006) has been largely characterized to date by fate-tracing of cells based on a handful of markers, together with genomic profiling studies of bulk populations (Hussein et al., 2014; O'Malley et al., 2013; Polo et al., 2012). Some studies (Mikkelsen et al., 2008; O'Malley et al., 2013; Parenti et al., 2016) have noted strong upregulation of several lineage-specific genes from unrelated lineages (*e.g.*, neurons), but it has been unclear whether this reflects coherent differentiation of specific cell types or disorganized gene expression (Kim et al., 2015; Mikkelsen et al., 2008). A recent study (Zhao et al., 2018) profiled ~36,000 cells with scRNA-seq in chemical rather than TF-based reprogramming, but identified only a single bifurcation event.

Analyzing >315,000 cells sampled densely across 18 days of reprogramming mouse embryonic fibroblasts (MEFs) into iPSCs, we find that reprogramming unleashes a much wider range of developmental programs and subprograms than previously characterized. Using Waddington-OT to reconstruct the landscape of differentiation trajectories and intermediate states that give rise to these diverse fates, we describe a gradual transition to either stroma-like cells or a mesenchymal-to-epithelial transition (MET) state. Trajectories emerge from the MET state to iPSCs, extraembryonic cells and neural cells. Based on the trajectories, we infer TFs predictive of various fates and suggest paracrine interactions between the stromal cells and other cell types. We experimentally showed that two top predictions indeed enhance reprogramming efficiency.

Results

Reconstruction of probabilistic trajectories by Optimal Transport

Our goal is to learn the relationship between ancestor cells at one time point and descendant cells at another time point: given that a cell has a specific expression profile at one time point, where will its descendants likely be at a later time point and where are its likely ancestors at an earlier time point? We model a differentiating population of cells as a time-varying probability distribution (*i.e.*, stochastic process) on a high-dimensional expression space. By sampling this probability distribution $\mathbb{P}_t$ at various time points t, we wish to infer how the differentiation process evolves over time (**Figure 1A**). From a large number of cells at a given time point (**Figure 1B**), we can approximate the distribution at that time point, but, because different cells are sampled independently at different time points, we lose the joint distribution of expression between pairs of time points, called *temporal coupling*. Absent any constraint on cellular transitions, we cannot infer the temporal coupling, but if we assume that cells move short distances over short time periods, then we can infer the temporal coupling by using the mathematical technique of optimal transport (**Figure 1A**, **STAR Methods**).

Optimal transport was originally developed to redistribute earth for the purpose of building fortifications with minimal work (Monge, 1781) and soon applied by Napoleon in Egypt. Kantorovich generalized it to identify an optimal coupling of probability distributions via linear programming (Kantorovich, 1942), minimizing the total squared distance that earth travels, subject to conservation of mass constraints.

However, the application to cells differs in one key respect: unlike earth, cells can proliferate. We therefore modify the classical conservation of mass constraints to accommodate cell growth and death (**STAR Methods**). Leveraging techniques from unbalanced transport (Chizat et al., 2018), we estimate cellular growth and death rates based on prior estimates from signatures of cellular proliferation and apoptosis (**STAR Methods**).

Using optimal transport, we calculate couplings between consecutive time points and then infer couplings over longer time-intervals by composing the transport maps between every pair of consecutive intermediate time points. The optimal-transport calculation (i) implicitly assumes that a cell's fate depends on its current position but not on its previous history (i.e., the stochastic process is Markov) and (ii) captures only the time-varying components of the distribution (see Discussion).

We define trajectories in terms of "descendant distributions" and "ancestor distributions". For any set C of cells at time t_i, its "descendant distribution" at a later time t_{i+1} is the *mass distribution* over all cells at time t_{i+1} given by transporting C according to the temporal coupling (**Figure 1C**). Conversely, its "ancestor distribution" at an earlier time t_{i-1} is the mass distribution over all cells at time t_{i-1}, obtained by "rewinding" time according to the temporal coupling (**Figure 1D**). Shared ancestry between two cell sets is revealed by convergence of the ancestor distributions (**Figure 1E**). The trajectory *from* C is the sequence of descendant distributions at each subsequent time point, and similarly the trajectory *to* C is the sequence of ancestor distributions (**Figure 1C,D**). Thus, we use the inferred coupling to calculate a distribution over representative ancestors and descendants at any other time. We can then determine the expression of any gene or gene signature along a trajectory by computing the mean expression level weighted by the distribution over cells at each time point.

To identify TFs that regulate the trajectory, we sample cells from the joint distribution given by the couplings to train regulatory models. One approach uses 'local' information, identifying TFs that are enriched in cells having many *vs*. few descendants in a target cell population. A second approach builds a global regulatory model, composed of modules of TFs and modules of target genes, to predict expression levels of gene signatures at later time points from expression levels of TFs at earlier ones (**Figure 1F**).

We implemented our approach in a method, Waddington-OT, for exploratory analysis of developmental landscapes and trajectories, including a public software package (**STAR Methods**). The method: (**1**) Performs optimal-transport analyses on scRNA-seq data from a time course, by calculating temporal couplings and using them to find ancestors, descendants and trajectories; (**2**) Infers regulatory models that drive the temporal dynamics; (**3**) Uses Force-Directed Layout Embedding (FLE) to visualize the cells in 2D (Jacomy et al., 2014; Weinreb et al., 2016; Zunder et al., 2015), and (**4**) Annotates cells by types, ancestors, descendants, trajectories, expression, and more.

A dense scRNA-seq time course of iPS reprogramming

We generated iPSCs via a secondary reprogramming system (**Figure 2A**). We obtained MEFs from a single female embryo which constitutively expresses a Dox-inducible polycistronic cassette carrying *Pou5f1* (*Oct4*), *Klf4*, *Sox2*, and *Myc (OKSM)*, and an EGFP reporter incorporated into the endogenous *Oct4* locus (Oct4-IRES-EGFP). We plated MEFs in serum, added Dox on day 0 to induce the OKSM cassette (Phase-1(Dox)), withdrew Dox at day 8, and transferred cells to either serum-free N2B27 2i medium (Phase-2(2i)) or maintained them in serum (Phase-2(serum)). Oct4-EGFP^{+} cells emerged on day 10 as a reporter for successful reprogramming to endogenous Oct4 expression (**Figure 2A, S1A**).

We performed two time-course experiments. In the first, we collected 65,781 scRNA-seq profiles at 10 time points across 16 days, with samples taken every 48 hours. In the second, we profiled 259,155 cells collected at 39 time points across 18 days, with samples taken every 12 hours (every 6 hours between days 8 and 9) (**Figure 2A**, **STAR Methods**, **Table S1**). The two experiments were consistent (**STAR Methods, Figure S1B, Figure S1C**). We focused on the second experiment (**Table S1**), retaining 251,203 high quality cells, sequenced at a depth enabling robust analysis, as shown by downsampling (**STAR Methods**). Comparison to bulk RNA-seq indicated that, with few exceptions, there is minimal sampling bias among cell types (**STAR Methods**).

Overview of the developmental landscape

We visualized the 251,203 cells in a two-dimensional FLE (**Figure 2B**), annotated according to condition (**Figure 2C**) sampling time (**Figure 2D, Movie S1**), and expression scores of gene signatures (**Figure 2E**). We identified notable features, discussed below, including sets of cells classified as pluripotent-, epithelial-, trophoblast-, neural-, and stromal-like by expression of characteristic signatures (**Figure 2E,F, Table S2**). The proportions of these subsets differ between serum and 2i conditions (**Figure 2G**).

Using Waddington-OT, we identified trajectories to these cell sets (**Figure 2H**). The ancestors of stromal-like cells begin to diverge from the rest as early as day 1.5, and the distinction sharpens over the next several days (**Figure 2I**). By contrast, the ancestors of the pluripotent-, epithelial-, trophoblast-, and neural-like populations are indistinguishable until after day 8, when the cells appear to undergo a mesenchymal-to-epithelial transition (MET), as we detail below.

The model is predictive and robust

Because current experimental approaches for tracing cell lineage do not describe the transcriptional profile of a cell set's ancestors, we developed a computational approach to validate the model. Given three time-points $t_1 < t_2 < t_3$, we used OT to predict the distribution of cells at time t_2, by interpolating the trajectory from t_1 to t_3 (**STAR Methods**). We compared our prediction to batches of observed cells at time t_2, they were are roughly as good as could be expected given batch-to-batch variation (**Figure 2J and S1D-F**). As expected, the quality of interpolation decreases over longer intervals (**Figure S1D**).

Our analysis is robust to data perturbations and parameter settings. We down-sampled the cells and reads at each time point, perturbed our initial estimates for cellular growth and death rates, and perturbed the parameters for entropic regularization and unbalanced transport (**Figure S1G-I, STAR Methods**). In all cases, the interpolation results are stable across wide range.

In initial stages of reprogramming, cells progress toward stromal or MET fates

Reprogramming begins with all cells exhibiting a rapid increase in cell-cycle signatures and a decrease in MEF identity (**Figure 2E**). Over time, cells assume either Stromal or MET identities (**Figure 3A,B,C**). Cells in the Stromal Region (SR) show distinctive signatures of extracellular matrix (ECM) rearrangement, senescence, cell cycle inhibitors, and a secretory phenotype (SASP) (**Figure 3D,E**). By contrast, the MET Region contains cells with increased proliferation and loss of fibroblast identity (**Figure 3D,F**).

While expressing signatures of embryonic mesenchyme and long-term cultured MEFs (**Figure S2A**), the SR does not simply reflect "MEF reversion" (**Figure S2B**). In particular, signatures of neonatal muscle and neonatal skin are enriched 20 to 30-fold in the SR.

The proportion of stromal cells peaks on days 10.5 to 11 and then declines through day 18 (**Figure 2G**). This is not due to cells exiting the SR (**Figure S2C**), but rather low proliferation and expression of an apoptosis signature.

Among the differentially expressed genes along the two trajectories were early markers of successful MET, including known markers such as *Fut9* (which synthesizes the glycoantigen SSEA-1) and novel candidates such as *Shisa8,* the most differentially expressed gene at day 1.5. It is expressed in 50% of cells most likely to transition to MET (top quartile) but only 5% of cells in the bottom quartile (**Table S3**). At later time points, both *Shisa8* and *Fut9* are strongly expressed along the trajectory toward successful reprogramming, and lowly expressed in other lineages (**Figure S2D**). *Shisa8* is a little-studied mammalian-specific member of the single-transmembrane, adapter-like *Shisa* family, that play developmental roles (Pei and Grishin, 2012).

Trajectory analysis allows us to trace how these fates are gradually established: the ancestor distributions of cells in the Stromal and MET Regions differ by 30% at day 3 and by 60% at day 6 (**Figure 2I**). A powerful predictor of a cell's fate is its expression level of the OKSM transgene, whose expression level explains ~50% of the variance in the log fate ratio between MET *vs*. stromal fate by day 2 and 75% by day 5 (**Figure S2E**). The divergence is gradual rather than a sharp branch point.

Regulatory analysis identifies TFs associated with the two trajectories. Three TFs (*Dmrtc2, Zic3, and Pou3f1*) show higher expression along the trajectory to the MET Region (**Figure 3C,F,G**).

Zic3 is required for maintenance of pluripotency (Lim et al., 2007), *Pou3f1* for self-renewal of spermatogonial stem cells (Wu et al., 2010), and *Dmrtc2* for germ cell development (Gegenschatz-Schmid et al., 2017). Four TFs (*Id3, Nfix, Nfic, and Prrx1*) show higher expression in cells with stromal fate (**Figure 3B,E,G**) which is maintained only in stromal cells following dox withdrawal. *Nfix* represses embryonic expression programs in early development, while *Nfic* and *Prrx1* are associated with mesenchymal programs (Froidure et al., 2016; Messina et al., 2010). Higher expression of *Id3* along the trajectory toward stromal cells may seem surprising, because its forced expression increases reprogramming efficiency (Liu et al., 2015). *Id3* might cause increased efficiency by acting in stromal cells, which secrete factors that enhance iPSC reprogramming (below), or in non-stromal cells, in which it is expressed through day 8, albeit at lower levels.

iPSCs emerge through a tight bottleneck from cells in the MET Region

The iPSC trajectory encompasses ~40% of all cells at day 8.5, but only ~10% of cells at day 10 in 2i conditions and only ~1% at day 11 in serum conditions. This suggests that only a small and distinct subset of cells transitioning out of the MET Region has the potential to become iPSCs. These iPSC progenitors have not yet fully acquired the pluripotency signature but are changing rapidly toward this fate. They reside along certain thin 'strings' in the FLE representation (**Figure 2H,** white arrow and **4A**, green). While the FLE shows what appears to be alternate paths (*e.g.*, through trophoblasts), the vast majority of ancestors of iPSCs do not go through these routes by our model (especially in 2i), highlighting a key difference between the OT-model and visualization-based interpretation.

By day 11.5-12.5, some cells begin to show a clear signature of pluripotency, including canonical marker genes such as *Nanog*, *Zfp42*, *Dppa4*, *Esrrb* and an elevated cell-cycle signature (**Figure 4B,C**). In 2i conditions, these iPS-like cells account for 12% of cells by day 11.5 and 80-90% from days 15 through 18 (**Figure 2G**), reflecting rapid proliferation. In serum conditions, the trend is similar, but the process is delayed and less efficient: the pluripotency signature is found in 3.5% of cells by day 12.5 and peaks at just 10-15% from days 15.5 through 18.

Recent studies reported that a small subset of cells in 2i conditions show a signature characteristic of the embryonic 2-cell (2C) stage (Kolodziejczyk et al., 2015). In our data ~1% of iPSCs showed a 2C signature in both 2i and serum conditions (**Table S2, Figure S3A**).

Clustering genes by expression trend along the trajectory to iPSCs revealed groups of activated genes regulating pluripotency and repressed genes involved in metabolic changes and RNA processing (**Figure S3B**). We identified 24 candidate markers of fully reprogrammed cells (including *Ooep*, *Fmr1nb*, *Lncenc1*, and *Tcl1*) (**Table S4**).

Regulatory analysis identifies a sequence of TF activity along the trajectory to iPSCs (**Figure 4C**). The earliest predictive TFs are expressed on days 9-10 (*Nanog*, *Sox2*, *Mybl2*, *Elf3*, *Tgif1*, *Klf2*, *Etv5*, *Cdc5l*, *Klf4*, *Esrrb*, *Spic*, *Zfp42*, *Hesx1*, and *Msc*). Of these 14 TFs, 9 have previously described roles in regulation of pluripotency (*Nanog*, *Sox2*, *Mybl2*, *Klf2*, *Cdc5l*, *Klf4*, *Esrrb*, *Zfp42*, and *Hesx1*) (Aaronson et al., 2016; Boheler, 2009; Buganim et al., 2012; Hu et al., 2009; Jeon et al., 2016; Li et al., 2015; Shi et al., 2006). A second wave is activated on days 12-14, including *Obox6*, *Sohlh2*, *Ddit3*, and *Bhlhe40*. Notably, *Obox6* and *Sohlh2* are not expressed in the trajectories to any other cell fate, and have roles in maintenance and survival of germ cells (Park et al., 2016; Rajkovic et al., 2002), but have not been previously implicated in pluripotency.

Finally, our trajectory analysis directly identifies the correct order of events in X-chromosome reactivation (Pasque et al., 2014): *Xist* is downregulated, then pluripotency-associated proteins are expressed, and finally the X-chromosome is reactivated (**Figure 4D,E, STAR Methods**).

Development of extra-embryonic-like cells during reprogramming

Another cell subset emerges from the MET Region, gains a strong epithelial signature by day 9, and expresses a trophoblast signature (**Figure 5A-C**) by day 10.5, peaking at day 12.5 (~20% of all cells) (**Figure 2G and 5B**).

Previous studies have noted the expression of some trophoblast-related genes (Cacchiarelli et al., 2015), but trophoblasts have not previously been characterized in reprogramming. We observe a remarkable diversity of subtypes. In normal development, the extraembryonic trophoblast progenitors (TPs) give rise to the chorion, which forms labyrinthine trophoblasts (LaTBs), and the ectoplacental cone, which forms spongiotrophoblasts (SpTBs) subtypes and trophoblast giant cells (TGCs), including spiral artery trophoblast giant cells (SpA-TGCs). Scoring our cells for signatures and markers of these cells (**Figure S4A**, **Table S2**, **Figure 5C**), we find TPs and SpTBs in 2i and serum and SpATGs in serum (**Figure S4A**), with cells that express LaTBs markers in a separate cluster (~200 cells in 2i but not serum) (**Figure S4A**). Another 181 cells from a single collection expressed a signature for primitive endoderm (XEN-like cells) (**Figure S4B**), as previously reported (Parenti et al., 2016).

Regulatory analysis identified TFs at day 10.5 that are predictive of subsequent trophoblast fate (**Figure 5B**). Several regulate trophoblast self-renewal *(Gata3, Elf5, Mycn, Mybl2)* (Kidder and Palmer, 2010) and early trophoblast differentiation *(Ovol2, Ascl2, Phlda2, Cited2)* (Latos and Hemberger, 2016; Tunster et al., 2016; Withington et al., 2006). Others are known to be expressed in trophoblasts, but have no known roles in trophoblast differentiation *(Rhox6, Rhox9, Batf3 and Elf3)*.

Other TFs are predictive of specific subtype fates. Ancestors of TP-like cells expressed *Gata3*, *Pparg*, *Rhox9*, *Myt1l*, *Hnf1b*, and *Prdm11*. *Gata3* is necessary for trophoblast progenitor differentiation (Ralston et al., 2010) and *Pparg* is necessary for trophoblast proliferation and differentiation of labyrinthine trophoblasts (Parast et al., 2009). Others are known to be expressed in placenta, but roles in differentiation has not been studied in most cases. Ancestors of SpTB- or LaTB-like cells expressed *Gata2*, *Gcm1*, *Msx2*, *Hoxd13*, and *Nr1h4*. *Gata2* is necessary for regulation of trophoblast programs (Ma et al., 1997). *Gcm1* and *Msx2* have roles in LaTB differentiation, EMT and trophoblast invasion (Liang et al., 2016; Simmons and Cross, 2005), respectively. *Nr1h4* is expressed in placenta. Ancestors of SpA-TGC-like cells expressed *Hand1*, *Bbx*, *Rhox6*, *Rhox9*, and *Gata2*. *Hand1* is necessary for trophoblast giant cell differentiation and invasion (Scott et al., 2000). *Bbx* is a core trophoblast gene induced by *Gata3* and *Cdx2* (Ralston et al., 2010).

RNA expression reveals genomic aberrations in trophoblast-like and stromal cells

Trophoblasts are known to selectively amplify specific functional genomic regions by endocycles of replication (Hannibal and Baker, 2016), and we hypothesized that they might harbor detectable genomic aberrations. Similarly, because our stromal cells express stress and apoptosis genes that are often associated with DNA damage, we speculated they too may have aberrations.

We thus analyzed the scRNA-seq data to infer large copy number aberrations from coherent increases or decreases in gene expression, as previously done for tumor cells (Patel et al., 2014), but requiring no consistency across cells (**STAR Methods**). We found evidence for whole-chromosome aneuploidy in 4.0% of trophoblast cells and 2.1% of stromal cells (*vs*. 1.1% of all other cells), mostly suggesting loss or gain of a single copy (**Figure 5D**).

We next searched for evidence of sub-chromosomal aberrations. We found evidence for events in 6.9% of trophoblasts and 3.2% of stromal cells (vs. 1.2% in most other cell types and 0.4% in neural cells) (**Figure 5E**). Our method has high specificity, but only 45% sensitivity (**Figure S4C, STAR Methods**).

In trophoblasts, one region, containing 74 genes appears to be highly enriched for sub-chromosomal aberrations (**Figure 5F;** 8.6% of trophoblasts); it includes *Wnt7b*, required for normal placental development (Parr et al., 2001); *Prr5*, which mediates *Pdfgb* signaling required for labyrinthine cell development (Ohlsson et al., 1999; Woo et al., 2007); and several 'core trophoblast genes' (*Cyb5r3*, *Cenpm*, *Srebf2*, *Pmm1*). The top 15 recurrent events also included the amplification of the prolactin gene cluster on chromosome 13 in 1% of cells. Thus, the trophoblast-associated mechanisms of genomic alteration may occur in the trophoblast-like cells.

Stromal cells frequently amplified a region containing cell cycle inhibitors *Cdkn2a*, *Cdkn2b*, and *Cdkn2c*, and frequently lost a region contained *Cdk13*, which promotes cell cycling, and *Mapk9*, loss of which promotes apoptosis. These genomic alterations may reflect and contribute to stromal cell function.

Neural-like cells also emerge from the MET Region during reprogramming in serum

In serum (but not 2i) conditions, neural-like cells also emerge from the MET Region, forming a prominent spike in the FLE (**Figure 5G**). Their ancestors diverge from the ancestors of trophoblasts and iPSCs by day 9 (**Figure 2I**), and undergo a rapid transition at day 12.5, losing epithelial signatures, gaining neural signatures, and entering the "neural spike" (**Figure 5G,H**). Cells near the base of the spike express radial glial and neural stem-cell markers, and cells further out along the spike express markers of neuronal differentiation (**Figure S4D,E**).

In normal development, neuroepithelial cells lose their epithelial identity and turn into radial glial cells (RGCs), which then give rise to astrocytes, oligodendrocytes, and neurons. We used scRNA-seq from mouse brain to derive signatures for these three mature cell types (**Table S2**), as well as three types of RGCs expressing *Id3*, *Gdf10*, or *Neurog2* (**Figure S4D**) (**STAR Methods**).

About 70% of neural-like cells express at least one of the six signatures. Cells with the three radial glial signatures appear first, concurrent with the loss of epithelial identity and gain of neural lineage identity on day 12.5 (**Figure 5I**). Cells expressing mature neurons and glia signatures emerge on day 14 and increase thereafter. Their ancestors are concentrated in the RGCs on day 13.5, especially *Gdf10* RGCs. While the glial populations overlap substantially, the neurons form a distinct population with substantial substructure, including excitatory and inhibitory neurons (**Figure 5J** and **S4C-E, STAR Methods**).

Regulatory analysis identified TFs predictive of neural fate, many with known roles in early neurogenesis (*Rarb*, *Foxp2*, *Emx1*, *Pou3f2*, *Nr2f1*, *Myt1l*, *Neurod4*), late neurogenesis (*Scrt2*, *Nhlh2*, *Pou2f2*), survival of neural subtypes (*Onecut1*, *Tal2*, *Barhl1*, *Pitx2*), and neural tube formation (*Msx1*, *Msx3*).

The developmental landscape highlights potential paracrine signals

We next asked how these cell types might affect each other as they reprogram concurrently. Paracrine signaling plays a key role in normal development and secretion of inflammatory cytokines has been shown to enhance reprogramming (Mosteiro et al., 2016). In our data, concurrent expression of ligand-receptor pairs across cell sets reveals rich potential for paracrine signaling (**Figure 6A,B, Figure S5A, Table S5**). We defined an interaction score based on the product of the fractions of (**1**) cells of type A expressing ligand X and (**2**) cells of type B expressing the cognate receptor Y, at the same time *t* (**Figure 6A,B** and **S5A,B**, **STAR Methods**). We observed high interaction scores for several SASP ligands in stromal cells with receptors expressed in iPSCs, such as *Gdf9* with *Tdgf1* and *Cxcl12* with *Dpp4* (**Figure 6C,F, S5C**).

Neural-like cells exhibit potential interactions involving *Cntfr* (**Figure 6D,G, S5D**), an *Il6*-family co-receptor whose activation plays critical roles in neural differentiation and survival (Elson et al., 2000; Nakashima et al., 1999). On day 11.5 in serum conditions, one day before the neural-like cells appear, their ancestors upregulate expression of *Cntfr*; expression is 4.6-fold higher in epithelial cells that are neural ancestors versus those that are not. One day earlier stromal cells begin expressing three activating ligands for *Cntfr* (*Crlf1*, *Lif*, *Clcf1*). These events may help trigger the program of neural differentiation in a subset of epithelial cells in serum. The same ligand-receptor interactions are seen in 2i conditions, but the MEK inhibitor in 2i medium would be expected to block *Cntfr* signaling and subsequent neural differentiation.

Trophoblast-like cells also show notable interaction scores, including *Csf1* and *Csf1r* (**Figure 6E,H, S5E**). In early placental development, *Csf1* is expressed in maternal columnar epithelial cells and *Csf1r* is expressed in fetal trophoblasts, suggesting a functional role of this interaction in trophoblast development. Many other top-ranked interactions for trophoblasts are between a single receptor (*Cxcr2*) and a multi-member ligand family (*Cxcl5*, *Cxcl1*, *Cxcl2*, *Cxcl3*, and *Cxcl15*) (**Figure 6E,H, S5E**). *Cxcr2* is necessary for trophoblast invasion in human (Wu et al., 2016).

Experimental validation confirms that transcription factor *Obox6* and cytokine GDF9 enhance reprogramming

We experimentally tested one of the TFs and one of the paracrine interactions that our analyses predicted might promote reprogramming.

We first tested the TF *Obox6*, which was the TF most strongly correlated with reprogramming success among those not previously implicated in the process (**Figure 7A, S6A**). *Obox6* is a homeobox gene of unknown function that is preferentially expressed in the oocyte, zygote, early embryos and embryonic stem cells (Rajkovic et al., 2002). While it is expressed in a small fraction of cells (<1%) before day 12, almost all cells expressing it (94%) are biased toward the MET Region (**Figure 7A, S6A**).

To test whether *Obox6* can boost reprogramming efficiency, we expressed it together with OKSM during days 0-8. We infected our secondary MEFs with a Dox-inducible lentivirus carrying either *Obox6*, the positive control *Zfp42* (Rajkovic et al., 2002; Shi et al., 2006), or no insert as a negative control. Both *Obox6* and *Zpf42* increased reprogramming efficiency of secondary MEFs by ~2-fold in 2i and even more so in serum (**Figure 7B,C**, and **Figure S6B-F**). Assays in primary MEFs showed similar increases (**Figure S6E,F**). Our results support a potential role for *Obox6* in reprogramming.

We next tested the cytokine GDF9, the ligand with the highest paracrine interaction score for the iPSC lineage, which is predicted to interact with the receptor *Tdgf1* (**Figure 6C,F**). *Tdgf1* is known to help maintain the pluripotent state (Klauzinska et al., 2014), but a role in the *establishment* of pluripotency has not been reported, and efforts to increase reprogramming efficiency through addition of GDF9 at the initial stages of reprogramming (days 0-2) were unsuccessful (Gonzalez-Muñoz et al. 2014).

In our reprogramming landscape, *Gdf9* and *Tdgf1* are expressed in the ancestors of iPSCs and stromal cells, respectively, beginning at day 8. The strength of the predicted interaction increases until day 14 (**Figure S5C**). We tested whether addition of recombinant mouse GDF9 enhances reprogramming in serum by adding the cytokine daily, starting at day 8 (**STAR Methods**). We measured the abundance of cell types at day 15 (**STAR Methods**).

In multiple independent experiments, GDF9 substantially increased reprogramming efficiency in a dose-dependent manner, with the highest dosage producing an average increase of 4-to-5-fold as assayed by (i) counting number of Oct4-GFP positive colonies, (ii) bulk RNA-seq and (iii) scRNA-seq (**Figure 7D-F** and **S6G-I**). These results support a role for *Gdf9* in reprogramming.

Interestingly, GDF9 also increased the fraction of cells with neural fates (**Figure 7F, S6I**), possibly in a competitive way with iPSCs. While *Gdf9* has no reported function in neurogenesis, the *Tgfβ* superfamily has been reported to play important roles in various neural lineages specification and maintenance (Aigner and Bogdahn, 2008); this observation warrants further attention.

Discussion

Understanding the trajectories of cellular differentiation is essential for studying development and for regenerative medicine. Here, we describe a new analytical approach to reconstructing trajectories, and its application to a dataset of 315,000 cells from dense time-courses of reprogramming fibroblasts into iPSCs, shedding new light on this problem, and providing a template for studies in other systems.

An optimal transport framework to model cell differentiation

Waddington-OT describes transitions between time points in terms of stochastic couplings, derived from optimal transport. This yields a natural concept of trajectories in terms of ancestor and descendant distributions, without strict structural constraints on the nature of these processes. This allows us to recover shared *vs*. distinct ancestry between two cell sets, and to infer TFs involved in activating expression programs (**Figure 1**). Moreover, it can be applied to even a single pair of time points. We validated Waddington-OT by its ability to accurately infer cellular populations at held-out time points and its results are robust across wide variation in parameters.

To set Waddington-OT in context, we comprehensively reviewed 62 other approaches (**Table S6**), which fall into three classes: category 1 (33 tools) is not applicable to developmental time-courses with scRNA-seq; category 2 (25 tools) is applicable but does not incorporate time information; and category 3 (4 tools) leverages time information, but does not model cell growth rates over time. When we applied several of the most widely used methods from categories 2 and 3 on our data, the results revealed key limitations (**STAR Methods**, **Figure S7**). Category 2 methods produced trajectories that are completely inconsistent with the time course—making huge leaps across time points and, in some cases, going backward in time. For example, Monocle2 produced trajectories in which Day 0 cells give rise to Day 18 cells, which then give rise to Day 8 cells.

Similar problems are evident in a Monocle2 analysis in a recent analysis of chemical reprogramming (Zhao et al., 2018), in which the program places late-stage cells at the beginning of the trajectory. Category 3 methods encounter a distinct challenge, as they do not account for the higher growth of iPSCs and consequently infer that many apoptotic stromal cells must transition to iPSCs. In addition, two of these Category 3 tools produced trajectories to incoherent final destinations, consisting of mixtures of very different cell types.

Waddington-OT is the only approach that incorporates temporal information and models cell growth over time (which we can consider a new Category 4). It is the only approach that produced reasonable trajectories on our data, suggesting that these features are critical for robust analysis of developmental processes. Moreover, it brings the powerful framework of optimal transport to biology and is the first application of OT to estimate the temporal coupling of a stochastic processes in any field.

Optimal-transport analysis is only intended to capture the *time-varying* components of a distribution $\mathbb{P}_t$. For systems in dynamic equilibrium, $\mathbb{P}_t$ does not change over time and optimal transport would infer that each cell is stationary. (An example would be cells that are asynchronously undergoing cell division. Although each cell is changing, the overall distribution $\mathbb{P}_t$ is constant across time.) Our focus is on out-of-equilibrium systems, where the distribution $\mathbb{P}_t$ undergoes major changes over time.

Tracking cell differentiation trajectories and fates in a diverse reprogramming landscape

Although the reprogramming of fibroblasts to iPSCs has been intensively studied, our work provides new insights that could only be obtained from large-scale profiling of single cells across dense time courses and appropriate analysis.

We uncovered remarkable diversity in the reprogramming landscape, with large classes of cells having distinct biological programs related to distinct states and tissues. Earlier studies based on bulk RNA analysis have detected expression of individual lineage-specific genes, but could not identify coherent cell types (Mikkelsen et al., 2008; O'Malley et al., 2013; Parenti et al., 2016). Further work will be need to characterize the cells' full identity and relation to natural types.

This extensive diversity raises several key questions, including: (**1**) What are the differentiation and fate trajectories that span these cell subsets? What are their ancestors and when do they diverge? (**2**) What cell intrinsic regulatory mechanisms may drive each fate, especially TFs? (**3**) How do cells of different types affect each other's development through paracrine signaling?

Our trajectory and regulatory analyses provide a systematic view of differentiation trajectories (**Figure 7G**). Cells gradually progress towards two initial fates: MET or Stromal (**Figure 7G**, blue and purple). There is an explosion of diversity following dox withdrawal at day 8: the MET state gives rise to iPSC-, trophoblast-, neural-, and epithelial-like cells. The ancestors of iPSCs pass through a narrow bottleneck before proliferating into iPSCs. Other cells in the MET region first assume an epithelial-like state which gives rise to trophoblasts and neural cells (in serum).

By characterizing events that occur along the trajectory toward any cell class, we identify TFs that regulate cell fates (**Figure 7G**). Along each trajectory, we rediscover known TFs known to play a role in the differentiation or reprogramming process, validating our approach, but also identify several new TFs not previously implicated in the process. We demonstrate the role of *Obox6* in increasing reprogramming efficiency.

Finally, we identify a rich potential for paracrine interactions with stromal cells which may play key roles in the initial differentiation and maintenance of iPS-, neural- and trophoblast-like cells. Of these interactions, we experimentally validated that GDF9 increases reprogramming efficiency.

Future prospects for models and studies of differentiation and development

Our method can be extended to capture additional features of differentiation. First, the framework currently assumes that a cell's trajectory depends only on its current gene-expression levels. One could incorporate other types of information like epigenomic state. Second, our framework for learning regulatory models assumes that trajectories are cell autonomous, but might be extended to incorporate intercellular interactions, such paracrine signaling, by using optimal transport for interacting particles (Ambrosio et al., 2008; Santambrogio, 2015) (**STAR Methods**). Third, various methods exist for obtaining lineage information about cells, based on the introduction of barcodes at discrete time points or continuously (Frieda et al., 2017; McKenna et al., 2016). Barcodes can be used to recognize cells that descend from a recent common ancestor cell, but do not currently directly reveal the full gene-expression state of the ancestral cell. However, they might be incorporated into our optimal-transport framework to better estimate temporal couplings. Finally, our method can be refined to analyze all time points simultaneously, rather than just consecutive pairs; this can be particularly useful for situations where the number of cells at different time points varies significantly.

In summary, our findings indicate that the process of reprogramming fibroblasts to iPSCs unleashes a much wider range of developmental programs and subprograms than previously characterized. In Waddington's metaphor, the reprogrammed cells roll through a rich landscape of valleys. Ultimately, the analysis of natural and artificial trajectories has much to teach us about the genetic circuits that control organismal development and regulate cellular homeostasis.

Acknowledgements:
We thank M. Kowalczyk, D. Przybylski, S. Markoulaki, J. Drotar, D. Rooney, R. Flannery for advice and reagents; L. Gaffney and A. Hupalowska for help with figures; D. Robin for help with software design; and J. Buenrostro and L. Chizat for discussions. Work was supported by funds from Broad Institute (E.S.L, A.R.), NIH grants HD045022, R01 MH104610-15, and R01NS088538 (R.J.), and R01HD058013 (K.H.). J.S. is supported by the Helen Hay Whitney Foundation and NIH Pathway to Independence Award K99HD096049. G.S., M.T., B.C., and A.R. are supported by Klarman Cell Observatory at Broad Institute and a CEGS grant from the NIH. G.S. is supported by a Career Award at the Scientific Interface from the Burroughs Wellcome Fund. P.R. is supported in part by NSF grants DMS-1712596, TRIPODS-1740751 and IIS-1838071; ONR grant N00014-17-1-2147; Chan Zuckerberg Initiative DAF 2018-182642; and MIT Skoltech Seed Fund.

Author Contributions:
J.S. and E.S.L. conceived and designed the study of reprogramming in single-cell resolution. G.S. and E.S.L. conceived the application of optimal transport; P.R., A.R., M.T., and B.C. provided input on the development of the approach. M.T., G.S., B.C., and J.G. developed WADDINGTON-OT. M.T., G.S., B.C., E.S.L. and A.R. analyzed the data, with assistance from J.S. All experiments were designed and performed by J.S., with input from R.J. and assistance from AS, SL, SL, PB, LL, JB, KH and VS. The manuscript was written by ESL, AR, GS, BC, MT, JS, and VS.

Declaration of Interests:

G.S., J.S., M.T., B.C., A.R., E.L. and P.R. are named inventors on International Patent Application No. PCT/US2018/051808 relating to work of this manuscript.

A.R. is a founder of Celsius Therapeutics and a member of the SAB of Syros Pharmaceuticals, Driver Group and ThermoFisher Scientific.

E.S.L. serves on the Board of Directors for Codiak BioSciences and Neon Therapeutics, and serves on the Scientific Advisory Board of F-Prime Capital Partners and Third Rock Ventures; he is also affiliated with several non-profit organizations including serving on the Board of Directors of the Innocence Project, Count Me In, and Biden Cancer Initiative, and the Board of Trustees for the Parker Institute for Cancer Immunotherapy. He has served and continues to serve on various federal advisory committees.

References

Aaronson, Y., Livyatan, I., Gokhman, D., and Meshorer, E. (2016). Systematic identification of gene family regulators in mouse and human embryonic stem cells. Nucleic Acids Research *44*, 4080-4089.

Aigner, L., and Bogdahn, U. (2008). TGF-beta in neural stem cells and in tumors of the central nervous system. Cell and Tissue Research *331*, 225-241.

Ambrosio, L., Gigli, N., and Savaré, G. (2008). Gradient flows: in metric spaces and in the space of probability measures (Springer Science & Business Media).

Boheler, K.R. (2009). Stem cell pluripotency: a cellular trait that depends on transcription factors, chromatin state and a checkpoint deficient cell cycle. Journal of cellular physiology *221*, 10-17.

Briggs, J.A., Weinreb, C., Wagner, D.E., Megason, S., Peshkin, L., Kirschner, M.W., and Klein, A.M. (2018). The dynamics of gene expression in vertebrate embryogenesis at single-cell resolution. Science.

Buganim, Y., Faddah, D.A., Cheng, A.W., Itskovich, E., Markoulaki, S., Ganz, K., Klemm, S.L., van Oudenaarden, A., and Jaenisch, R. (2012). Single-cell expression analyses during cellular reprogramming reveal an early stochastic and a late hierarchic phase. Cell *150*, 1209-1222.

Butler, A., Hoffman, P., Smibert, P., Papalexi, E., and Satija, R. (2018). Integrating single-cell transcriptomic data across different conditions, technologies, and species. Nature Biotechnology *36*, 411.

Cacchiarelli, D., Trapnell, C., Ziller, M.J., Soumillon, M., Cesana, M., Karnik, R., Donaghey, J., Smith, Z.D., Ratanasirintrawoot, S., Zhang, X*., et al.* (2015). Integrative Analyses of Human Reprogramming Reveal Dynamic Nature of Induced Pluripotency. Cell *162*, 412-424.

Chizat, L., Peyré, G., Schmitzer, B., and Vialard, F.-X. (2018). Scaling algorithms for unbalanced transport problems. Mathematics of Computation.

Cuturi, M. (2013). Sinkhorn distances: Lightspeed computation of optimal transportation distances. In Neural Information Processing Systems (NIPS).

Elson, G.C., Lelièvre, E., Guillet, C., Chevalier, S., Plun-Favreau, H., Froger, J., Suard, I., de Coignac, A.B., Delneste, Y., and Bonnefoy, J.-Y. (2000). CLF associates with CLC to form a functional heteromeric ligand for the CNTF receptor complex. Nature neuroscience *3*, 867.

Farrell, J.A., Wang, Y., Riesenfeld, S.J., Shekhar, K., Regev, A., and Schier, A.F. (2018). Single-cell reconstruction of developmental trajectories during zebrafish embryogenesis. Science.

Fincher, C.T., Wurtzel, O., de Hoog, T., Kravarik, K.M., and Reddien, P.W. (2018). Cell type transcriptome atlas for the planarian Schmidtea mediterranea. Science.

Frieda, K.L., Linton, J.M., Hormoz, S., Choi, J., Chow, K.-H.K., Singer, Z.S., Budde, M.W., Elowitz, M.B., and Cai, L. (2017). Synthetic recording and in situ readout of lineage information in single cells. Nature *541*, 107.
Froidure, A., Marchal-Duval, E., Ghanem, M., Gerish, L., Jaillet, M., Crestani, B., and Mailleux, A. (2016). Mesenchyme associated transcription factor PRRX1: A key regulator of IPF fibroblast. European Respiratory Journal *48*.
Gegenschatz-Schmid, K., Verkauskas, G., Demougin, P., Bilius, V., Dasevicius, D., Stadler, M.B., and Hadziselimovic, F. (2017). DMRTC2, PAX7, BRACHYURY/T and TERT Are Implicated in Male Germ Cell Development Following Curative Hormone Treatment for Cryptorchidism-Induced Infertility. Genes *8*, 267.
Hannibal, Roberta L., and Baker, Julie C. (2016). Selective Amplification of the Genome Surrounding Key Placental Genes in Trophoblast Giant Cells. Current Biology *26*, 230-236.
Heinz, S., Benner, C., Spann, N., Bertolino, E., Lin, Y.C., Laslo, P., Cheng, J.X., Murre, C., Singh, H., and Glass, C.K. (2010). Simple combinations of lineage-determining transcription factors prime cis-regulatory elements required for macrophage and B cell identities. Mol Cell *38*, 576-589.
Herman, J.S., Sagar, and Grün, D. (2018). FateID infers cell fate bias in multipotent progenitors from single-cell RNA-seq data. Nature Methods *15*, 379.
Hu, G., Kim, J., Xu, Q., Leng, Y., Orkin, S.H., and Elledge, S.J. (2009). A genome-wide RNAi screen identifies a new transcriptional module required for self-renewal. Genes & development *23*, 837-848.
Hussein, S.M., Puri, M.C., Tonge, P.D., Benevento, M., Corso, A.J., Clancy, J.L., Mosbergen, R., Li, M., Lee, D.-S., and Cloonan, N. (2014). Genome-wide characterization of the routes to pluripotency. Nature *516*, 198.
Jacomy, M., Venturini, T., Heymann, S., and Bastian, M. (2014). ForceAtlas2, a continuous graph layout algorithm for handy network visualization designed for the Gephi software. PloS one *9*, e98679.
Jeon, H., Waku, T., Azami, T., Khoa le, T.P., Yanagisawa, J., Takahashi, S., and Ema, M. (2016). Comprehensive Identification of Kruppel-Like Factor Family Members Contributing to the Self-Renewal of Mouse Embryonic Stem Cells and Cellular Reprogramming. PloS one *11*, e0150715.
Jordan, R., Kinderlehrer, D., and Otto, F. (1998). The variational formulation of the fokker. SIAM J. Math. Anal., 29(1):1–17.
Kantorovich, L. (1942). On the transfer of masses (in russian).
Kester, L., and van Oudenaarden, A. (2018). Single-Cell Transcriptomics Meets Lineage Tracing. Cell Stem Cell.
Kidder, B.L., and Palmer, S. (2010). Examination of transcriptional networks reveals an important role for TCFAP2C, SMARCA4, and EOMES in trophoblast stem cell maintenance. Genome Res *20*, 458-472.
Kim, D.H., Marinov, G.K., Pepke, S., Singer, Z.S., He, P., Williams, B., Schroth, G.P., Elowitz, M.B., and Wold, B.J. (2015). Single-cell transcriptome analysis reveals dynamic changes in lncRNA expression during reprogramming. Cell stem cell *16*, 88-101.
Klauzinska, M., Castro, N.P., Rangel, M.C., Spike, B.T., Gray, P.C., Bertolette, D., Cuttitta, F., and Salomon, D. (2014). The multifaceted role of the embryonic gene Cripto-1 in cancer, stem cells and epithelial-mesenchymal transition. Seminars in cancer biology *0*, 51-58.
Kolodziejczyk, Aleksandra A., Kim, Jong K., Tsang, Jason C., Ilicic, T., Henriksson, J., Natarajan, Kedar N., Tuck, Alex C., Gao, X., Bühler, M., Liu, P.*, et al.* (2015). Single Cell RNA-Sequencing of Pluripotent States Unlocks Modular Transcriptional Variation. Cell Stem Cell *17*, 471-485.
Latos, P.A., and Hemberger, M. (2016). From the stem of the placental tree: trophoblast stem cells and their progeny. Development *143*, 3650-3660.

Le´onard, C. (2014). A survey of the schro¨dinger problem and some of its connections with optimal transport. Discrete and Continuous Dynamical Systems - Series A (DCDS-A), 34(4):1533–1574.
Li, W.-Z., Wang, Z.-W., Chen, L.-L., Xue, H.-N., Chen, X., Guo, Z.-K., and Zhang, Y. (2015). Hesx1 enhances pluripotency by working downstream of multiple pluripotency-associated signaling pathways. Biochemical and Biophysical Research Communications *464*, 936-942.
Liang, H., Zhang, Q., Lu, J., Yang, G., Tian, N., Wang, X., Tan, Y., and Tan, D. (2016). MSX2 Induces Trophoblast Invasion in Human Placenta. PloS one *11*, e0153656.
Lim, L.S., Loh, Y.H., Zhang, W., Li, Y., Chen, X., Wang, Y., Bakre, M., Ng, H.H., and Stanton, L.W. (2007). Zic3 is required for maintenance of pluripotency in embryonic stem cells. Molecular biology of the cell *18*, 1348-1358.
Liu, J., Han, Q., Peng, T., Peng, M., Wei, B., Li, D., Wang, X., Yu, S., Yang, J., Cao, S.*, et al.* (2015). The oncogene c-Jun impedes somatic cell reprogramming. Nature cell biology *17*, 856-867.
Liu, L.L., Brumbaugh, J., Bar-Nur, O., Smith, Z., Stadtfeld, M., Meissner, A., Hochedlinger, K., and Michor, F. (2016). Probabilistic Modeling of Reprogramming to Induced Pluripotent Stem Cells. Cell reports *17*, 3395-3406.
Lönnberg, T., Svensson, V., James, K.R., Fernandez-Ruiz, D., Sebina, I., Montandon, R., Soon, M.S.F., Fogg, L.G., Nair, A.S., Liligeto, U.N.*, et al.* (2017). Single-cell RNA-seq and computational analysis using temporal mixture modeling resolves Th1/Tfh fate bifurcation in malaria. Science Immunology *2*.
Ma, G.T., Roth, M.E., Groskopf, J.C., Tsai, F.Y., Orkin, S.H., Grosveld, F., Engel, J.D., and Linzer, D.I. (1997). GATA-2 and GATA-3 regulate trophoblast-specific gene expression in vivo. Development *124*, 907-914.
Marco, E., Karp, R.L., Guo, G., Robson, P., Hart, A.H., Trippa, L., and Yuan, G.C. (2014). Bifurcation analysis of single-cell gene expression data reveals epigenetic landscape. Proceedings of the National Academy of Sciences of the United States of America *111*, E5643-5650.
McKenna, A., Findlay, G.M., Gagnon, J.A., Horwitz, M.S., Schier, A.F., and Shendure, J. (2016). Whole-organism lineage tracing by combinatorial and cumulative genome editing. Science *353*, aaf7907.
Mertins, P., Przybylski, D., Yosef, N., Qiao, J., Clauser, K., Raychowdhury, R., Eisenhaure, T.M., Maritzen, T., Haucke, V., Satoh, T.*, et al.* (2017). An Integrative Framework Reveals Signaling-to-Transcription Events in Toll-like Receptor Signaling. Cell reports *19*, 2853-2866.
Messina, G., Biressi, S., Monteverde, S., Magli, A., Cassano, M., Perani, L., Roncaglia, E., Tagliafico, E., Starnes, L., Campbell, C.E.*, et al.* (2010). Nfix regulates fetal-specific transcription in developing skeletal muscle. Cell *140*, 554-566.
Mikkelsen, T.S., Hanna, J., Zhang, X., Ku, M., Wernig, M., Schorderet, P., Bernstein, B.E., Jaenisch, R., Lander, E.S., and Meissner, A. (2008). Dissecting direct reprogramming through integrative genomic analysis. Nature *454*, 49.
Monge, G. (1781). Mémoire sur la théorie des déblais et des remblais. Mém de l'Ac R des Sc, 666–704.
Mosteiro, L., Pantoja, C., Alcazar, N., Marión, R.M., Chondronasiou, D., Rovira, M., Fernandez-Marcos, P.J., Muñoz-Martin, M., Blanco-Aparicio, C., and Pastor, J. (2016). Tissue damage and senescence provide critical signals for cellular reprogramming in vivo. Science *354*, aaf4445.
Nakashima, K., Wiese, S., Yanagisawa, M., Arakawa, H., Kimura, N., Hisatsune, T., Yoshida, K., Kishimoto, T., Sendtner, M., and Taga, T. (1999). Developmental requirement of gp130 signaling in neuronal survival and astrocyte differentiation. The Journal of neuroscience : the official journal of the Society for Neuroscience *19*, 5429-5434.

O'Malley, J., Skylaki, S., Iwabuchi, K.A., Chantzoura, E., Ruetz, T., Johnsson, A., Tomlinson, S.R., Linnarsson, S., and Kaji, K. (2013). High resolution analysis with novel cell-surface markers identifies routes to iPS cells. Nature *499*, 88.
Parast, M.M., Yu, H., Ciric, A., Salata, M.W., Davis, V., and Milstone, D.S. (2009). PPARgamma regulates trophoblast proliferation and promotes labyrinthine trilineage differentiation. PloS one *4*, e8055.
Parenti, A., Halbisen, M.A., Wang, K., Latham, K., and Ralston, A. (2016). OSKM induce extraembryonic endoderm stem cells in parallel to induced pluripotent stem cells. Stem cell reports *6*, 447-455.
Park, M., Lee, Y., Jang, H., Lee, O.H., Park, S.W., Kim, J.H., Hong, K., Song, H., Park, S.P., Park, Y.Y*., et al.* (2016). SOHLH2 is essential for synaptonemal complex formation during spermatogenesis in early postnatal mouse testes. Scientific reports *6*, 20980.
Pasque, V., Tchieu, J., Karnik, R., Uyeda, M., Dimashkie, A.S., Case, D., Papp, B., Bonora, G., Patel, S., and Ho, R. (2014). X chromosome reactivation dynamics reveal stages of reprogramming to pluripotency. Cell *159*, 1681-1697.
Patel, A.P., Tirosh, I., Trombetta, J.J., Shalek, A.K., Gillespie, S.M., Wakimoto, H., Cahill, D.P., Nahed, B.V., Curry, W.T., Martuza, R.L*., et al.* (2014). Single-cell RNA-seq highlights intratumoral heterogeneity in primary glioblastoma. Science (New York, NY) *344*, 1396-1401.
Pei, J., and Grishin, N.V. (2012). Unexpected diversity in Shisa-like proteins suggests the importance of their roles as transmembrane adaptors. Cellular signalling *24*, 758-769.
Plass, M., Solana, J., Wolf, F.A., Ayoub, S., Misios, A., Glažar, P., Obermayer, B., Theis, F.J., Kocks, C., and Rajewsky, N. (2018). Cell type atlas and lineage tree of a whole complex animal by single-cell transcriptomics. Science.
Polo, J.M., Anderssen, E., Walsh, R.M., Schwarz, B.A., Nefzger, C.M., Lim, S.M., Borkent, M., Apostolou, E., Alaei, S., and Cloutier, J. (2012). A molecular roadmap of reprogramming somatic cells into iPS cells. Cell *151*, 1617-1632.
Rajkovic, A., Yan, C., Yan, W., Klysik, M., and Matzuk, M.M. (2002). Obox, a Family of Homeobox Genes Preferentially Expressed in Germ Cells. Genomics *79*, 711-717.
Ralston, A., Cox, B.J., Nishioka, N., Sasaki, H., Chea, E., Rugg-Gunn, P., Guo, G., Robson, P., Draper, J.S., and Rossant, J. (2010). Gata3 regulates trophoblast development downstream of Tead4 and in parallel to Cdx2. Development *137*, 395-403.
Rashid, S., Kotton, D.N., and Bar-Joseph, Z. (2017). TASIC: determining branching models from time series single cell data. Bioinformatics *33*, 2504-2512.
Saelens, W., Cannoodt, R., Todorov, H., and Saeys, Y. (2018). A comparison of single-cell trajectory inference methods: towards more accurate and robust tools. bioRxiv.
Santambrogio, F. (2015). Optimal transport for applied mathematicians. Birkäuser, NY, 99-102.
Satija, R., Farrell, J.A., Gennert, D., Schier, A.F., and Regev, A. (2015). Spatial reconstruction of single-cell gene expression data. Nature Biotechnology *33*, 495.
Scott, I.C., Anson-Cartwright, L., Riley, P., Reda, D., and Cross, J.C. (2000). The HAND1 basic helix-loop-helix transcription factor regulates trophoblast differentiation via multiple mechanisms. Molecular and cellular biology *20*, 530-541.
Schrodinger, E. (1932). Sur la theorie relativiste de l'electron et l'interpretation de la mecanique quan- tique. Ann. Inst. H. Poincare, 2:269–310.
Shi, W., Wang, H., Pan, G., Geng, Y., Guo, Y., and Pei, D. (2006). Regulation of the pluripotency marker Rex-1 by Nanog and Sox2. J Biol Chem *281*, 23319-23325.
Simmons, D.G., and Cross, J.C. (2005). Determinants of trophoblast lineage and cell subtype specification in the mouse placenta. Developmental biology *284*, 12-24.
Stadtfeld, M., Maherali, N., Borkent, M., and Hochedlinger, K. (2010). A reprogrammable mouse strain from gene-targeted embryonic stem cells. Nature methods *7*, 53-55.
Takahashi, K., and Yamanaka, S. (2006). Induction of pluripotent stem cells from mouse embryonic and adult fibroblast cultures by defined factors. cell *126*, 663-676.

Takahashi, K., and Yamanaka, S. (2016). A decade of transcription factor-mediated reprogramming to pluripotency. Nature Reviews Molecular Cell Biology *17*, 183.
Tanay, A., and Regev, A. (2017). Scaling single-cell genomics from phenomenology to mechanism. Nature *541*, 331-338.
Tibshirani, R., Walther, G., and Hastie, T. (2001). Estimating the Number of Clusters in a Data Set Via the Gap Statistic, Vol 63.
Tirosh, I., Venteicher, A.S., Hebert, C., Escalante, L.E., Patel, A.P., Yizhak, K., Fisher, J.M., Rodman, C., Mount, C., and Filbin, M.G. (2016). Single-cell RNA-seq supports a developmental hierarchy in human oligodendroglioma. Nature *539*, 309-313.
Tunster, S.J., Creeth, H.D.J., and John, R.M. (2016). The imprinted Phlda2 gene modulates a major endocrine compartment of the placenta to regulate placental demands for maternal resources. Developmental biology *409*, 251-260.
Villani, C. (2008). Optimal Transport Old and New. Springer.
Waddington, C.H. (1936). How animals develop (New York).
Waddington, C.H. (1957). The strategy of the genes; a discussion of some aspects of theoretical biology (London, Allen & Unwin [1957]).
Wagner, D.E., Weinreb, C., Collins, Z.M., Briggs, J.A., Megason, S.G., and Klein, A.M. (2018). Single-cell mapping of gene expression landscapes and lineage in the zebrafish embryo. Science.
Weinreb, C., Wolock, S., and Klein, A. (2016). SPRING: a kinetic interface for visualizing high dimensional single-cell expression data. bioRxiv.
Weinreb, C., Wolock, S., Tusi, B.K., Socolovsky, M., and Klein, A.M. (2017). Fundamental limits on dynamic inference from single cell snapshots. bioRxiv.
Withington, S.L., Scott, A.N., Saunders, D.N., Lopes Floro, K., Preis, J.I., Michalicek, J., Maclean, K., Sparrow, D.B., Barbera, J.P., and Dunwoodie, S.L. (2006). Loss of Cited2 affects trophoblast formation and vascularization of the mouse placenta. Developmental biology *294*, 67-82.
Wolf, F.A., Hamey, F., Plass, M., Solana, J., Dahlin, J.S., Gottgens, B., Rajewsky, N., Simon, L., and Theis, F.J. (2017). Graph abstraction reconciles clustering with trajectory inference through a topology preserving map of single cells. bioRxiv.
Wu, D., Hong, H., Huang, X., Huang, L., He, Z., Fang, Q., and Luo, Y. (2016). CXCR2 is decreased in preeclamptic placentas and promotes human trophoblast invasion through the Akt signaling pathway. Placenta *43*, 17-25.
Wu, X., Oatley, J.M., Oatley, M.J., Kaucher, A.V., Avarbock, M.R., and Brinster, R.L. (2010). The POU domain transcription factor POU3F1 is an important intrinsic regulator of GDNF-induced survival and self-renewal of mouse spermatogonial stem cells. Biology of reproduction *82*, 1103-1111.
Ying, Q.-L., Wray, J., Nichols, J., Batlle-Morera, L., Doble, B., Woodgett, J., Cohen, P., and Smith, A. (2008). The ground state of embryonic stem cell self-renewal. Nature *453*, 519.
Zhao, T., Fu, Y., Zhu, J., Liu, Y., Zhang, Q., Yi, Z., Chen, S., Jiao, Z., Xu, X., Xu, J.*, et al.* (2018). Single-Cell RNA-Seq Reveals Dynamic Early Embryonic-like Programs during Chemical Reprogramming. Cell Stem Cell *23*, 31-45.e37.
Zunder, E.R., Lujan, E., Goltsev, Y., Wernig, M., and Nolan, G.P. (2015). A continuous molecular roadmap to iPSC reprogramming through progression analysis of single-cell mass cytometry. Cell Stem Cell *16*, 323-337.

MAIN FIGURE LEGENDS

Figure 1

Modeling developmental processes with optimal transport.

(**A**) A temporal progression of a time-varying distribution $\mathbb{P}_t$ (left) can be sampled to obtain finite empirical distributions of cells $\widehat{\mathbb{P}}_{t_i}$ at various time points t_1, t_2, t_3 (right). Over short time scales, the unknown true coupling, γ_{t_1,t_2}, is assumed to be close to the optimal transport coupling, π_{t_1,t_2}, which can be approximated by $\hat{\pi}_{t_1,t_2}$ computed from the empirical distributions $\widehat{\mathbb{P}}_{t_1}$ and $\widehat{\mathbb{P}}_{t_2}$. (**B**) Single-cell profiles (individual dots) are colored by the time of collection. (**C**) Descendants of a cell set (black) at later times. (**D**) Ancestors at earlier times. (**E**) Shared ancestry of two cell sets (black). Ancestors of each population shown in red and blue, shared ancestors in purple. (**F**) Expression of gene signatures (left; green, high expression; grey, low expression) can be predicted from earlier expression of transcription factors (middle; black, high expression; grey, low expression) in a gene regulatory model by analyzing trends along ancestor trajectories (right).

Figure 2.

A single cell RNA-Seq time course of iPSC reprogramming.

(A) Reprogramming of secondary (2°) MEFs from E13.5 embryos. Each dot represents a collection time-point. **(B-F)** FLE visualization of scRNA-seq profiles (individual dots). (**B**) Intensity indicates density of cells in the 2D FLE. (**C**) Cells colored by condition, with Phase-1 (dox) in black and Phase 2 in blue (serum) and red (2i). (**D**) Cells colored by time point, with Phase-2 points from only either 2i condition (left) or serum condition (right). Grey points represent Phase-2 cells from the other condition. (**E**) Patterns of gene signature scores on the FLE. (**F**) Cell set membership. (**G**) Relative abundance (y-axis) of each cell set (colored lines) plotted over time in 2i (top) and serum (bottom). (**H**) Schematic representation of trajectories. (**I**) Ancestor divergence for pairs of trajectories. Divergence (y-axis) is quantified as 0.5 times the total variation distance between ancestor distributions. **(J)** Quality of interpolation in serum for OT (red), null models with growth (blue) and without growth (teal). Shaded regions indicate 1 standard deviation. Note that OT is almost as accurate as the batch-to-batch baseline (green). See also Figure S1, S7, Table S1, S2, S6 and Movie S1.

Figure 3

In initial stages of reprogramming, cells progress toward stromal or MET fates

(**A**) The log-likelihood of obtaining stromal vs. MET fate shows a gradual emergence of fates from day 0 through 8. (**B**) Ancestors of day 18 stromal cells in serum. Color shows day, intensity shows probability. (**C**) Ancestors of day 8 MET cells have a distinct trajectory. (**D**) Activity of gene signatures and individual gene expression (log(TPM+1)) that are associated with stromal activity and senescence. (**E**) and **(F)** Gene signature trends along indicated trajectories. (**G**) TF expression trends along stromal and MET trajectories. See also Figure S2 and Table S2, S3.

Figure 4

iPSCs emerge from cells in the MET Region

(**A**) Ancestor trajectory of day 18 iPSCs in 2i (left) and serum (right) (color shows day, intensity shows probability). (**B**) Expression (log(TPM+1)) of pluripotency marker genes. (**C**) Expression trends along ancestor trajectory in serum for gene signatures (top) and TFs (bottom). (**D**) X-reactivation signature (mean z-score) and *Xist* expression (log(TPM + 1)) on the FLE. (**E**) Trends

in X-inactivation, X-reactivation and pluripotency (**Table S4**) along the iPSC trajectory in 2i. Each curve has a different y-axis, indicated by color. See also Figure S3 and Table S2, S4.

Figure 5

Extra-embryonic and neural-like cells emerge during reprogramming

(**A**) Ancestor trajectory of day 18 trophoblasts in 2i (left) and serum (right) (color shows day, intensity shows probability). (**B**) Expression trends along trophoblast trajectory in serum for gene signatures (left) and individual TFs (right). (**C**) An embedding of trophoblasts, colored by signature scores (-log10(FDR q-value)) of TPs, SpA-TGCs, and SpTBs, or by expression of LaTB marker gene *Gcm1* (log(TPM + 1)). (**D**) Average expression of housekeeping genes on chromosomes in single cells (dots) with evidence of genomic amplification (left) or loss (right), relative to all cells without evidence of aberrations (y-axis). (**E**) Cells are colored by statistical significance (-log10(q-value)) of sub-chromosomal aberrations. (**F**) Average expression of genes on chromosome 15 in trophoblast-like cells with evidence of a recurrent sub-chromosomal amplification (y-axis, fold change (FC) in expression relative to other cells). (**G**) Ancestors of day 18 cells in the neural region. (**H**) Expression trends along the neural trajectory for gene signatures (left) and individual TFs (right). (**I**) Abundance of neural subtypes. (**J**) A Neural FLE colored by significance of signature scores ($-\log_{10}$(FDR q-value)) and expression of markers (log(TPM + 1)). See also Figure S4 and Table S2.

Figure 6

Paracrine signaling

(**A**) High paracrine signaling interactions occur between groups of cells with high expression of ligand in one group and cognate receptor in the other group. (**B**) Net paracrine signaling interaction scores in serum. Each dot shows the net score for a pair of cell clusters (Figure S5A). (**C**-**E**) Potential ligand-receptor pairs between ancestors of stromal cells and iPSCs (**C**), neural-like cells (**D**), and trophoblasts (**E**). (**F**-**H**) Expression level (log(TPM+1)) of ligands (above) and receptors (below) for top interacting pairs between stromal cells and iPSCs (**F**), neural-like cells (**G**), and trophoblasts (**H**). See also Figure S5 and Table S5.

Figure 7

***Obox6* and GDF9 enhance reprogramming**

(A) Log-likelihood ratio of obtaining iPSC vs non-iPSC fate on each day (x-axis) in 2i. *Obox6*$^+$ cells in red. **(B)** Bright field and fluorescence images of iPSC colonies generated in 2i by overexpression of OKSM with either *Zfp42 or Obox6* (or negative control). **(C)** Percentage of Oct4-EGFP$^+$ colonies in 2i on day 16, for one of five experiments (**Figure S6D**). Error bars show standard deviation of three biological replicates. (**D-F**) Effect of varying concentration of GDF9 (red) vs control (grey) on (**D**) Oct4-EGFP$^+$ colonies (error bars show standard deviation); (**E**) the strength of iPSC signature score in bulk RNA-Seq; and (**F**) cellular composition assayed by scRNA-seq. **(G)** Schematic of the reprogramming landscape in serum. Color indicates cell-set membership. Color of TFs indicates which cell set they regulate. Color of cytokine indicates the cell class to which they signal. See also Figure S6.

Figure 1

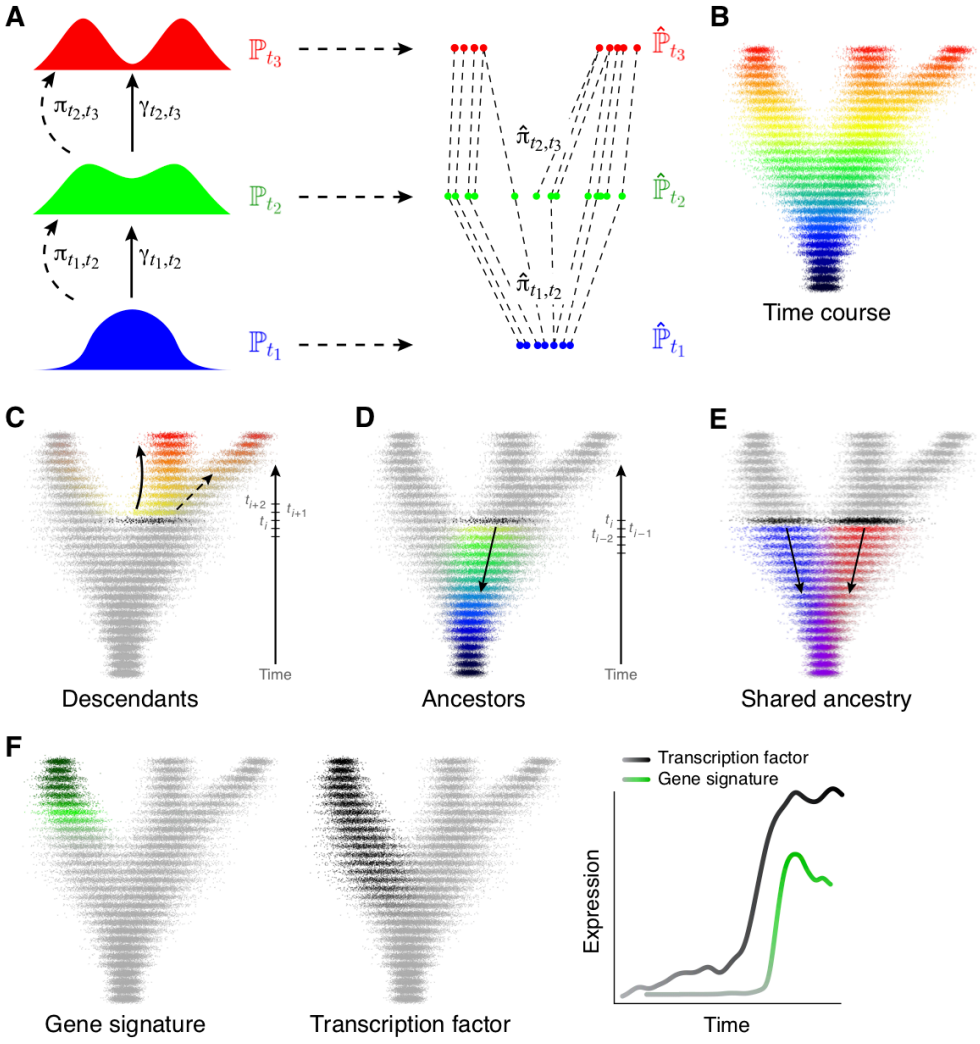
A
B
C
D
E
F
Time course
Descendants
Ancestors
Shared ancestry
Time
Gene signature
Transcription factor
Transcription factor
Gene signature
Expression
Time

Figure 2

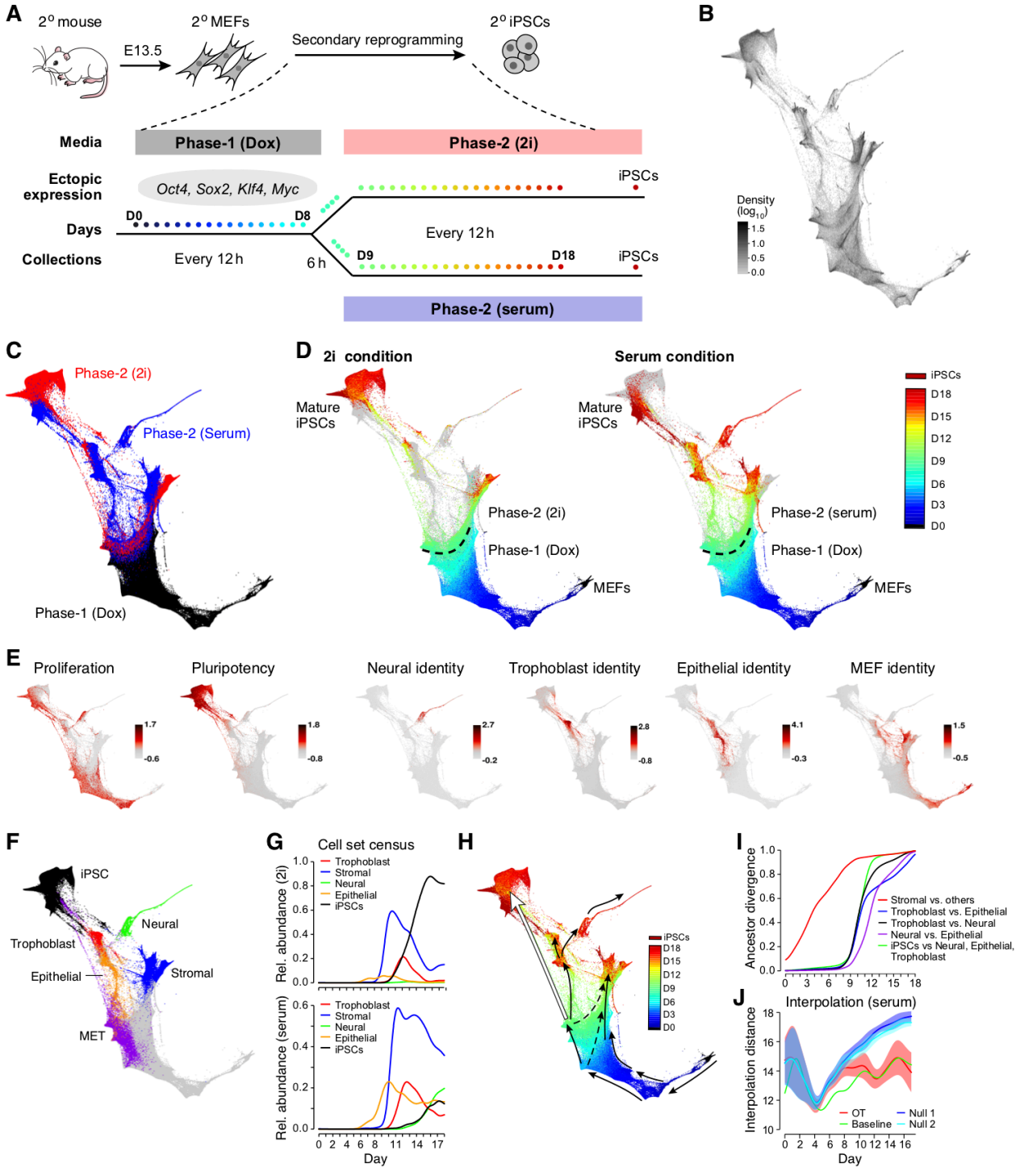
A
2° mouse
E13.5
2° MEFs
Secondary reprogramming
2° iPSCs
Media
Phase-1 (Dox)
Phase-2 (2i)
Ectopic expression
Oct4, Sox2, Klf4, Myc
iPSCs
Days
D0
D8
Every 12 h
Collections
Every 12 h
6 h
D9
D18
iPSCs
Phase-2 (serum)
B
Density (log10)
1.5
1.0
0.5
0.0
C
Phase-2 (2i)
Phase-2 (Serum)
Phase-1 (Dox)
D
2i condition
Serum condition
Mature iPSCs
Mature iPSCs
Phase-2 (2i)
Phase-1 (Dox)
MEFs
Phase-2 (serum)
Phase-1 (Dox)
MEFs
iPSCs
D18
D15
D12
D9
D6
D3
D0
E
Proliferation
Pluripotency
Neural identity
Trophoblast identity
Epithelial identity
MEF identity
1.7
-0.6
1.8
-0.8
2.7
-0.2
2.8
-0.8
4.1
-0.3
1.5
-0.5
F
iPSC
Neural
Trophoblast
Epithelial
Stromal
MET
G
Cell set census
Trophoblast
Stromal
Neural
Epithelial
iPSCs
Rel. abundance (2i)
Rel. abundance (serum)
0 2 4 6 8 11 14 17
Day
H
iPSCs
D18
D15
D12
D9
D6
D3
D0
I
Ancestor divergence
Stromal vs. others
Trophoblast vs. Epithelial
Trophoblast vs. Neural
Neural vs. Epithelial
iPSCs vs Neural, Epithelial, Trophoblast
0 3 6 9 12 15 18
J
Interpolation (serum)
Interpolation distance
OT
Baseline
Null 1
Null 2
0 2 4 6 8 10 12 14 16
Day

Figure 3

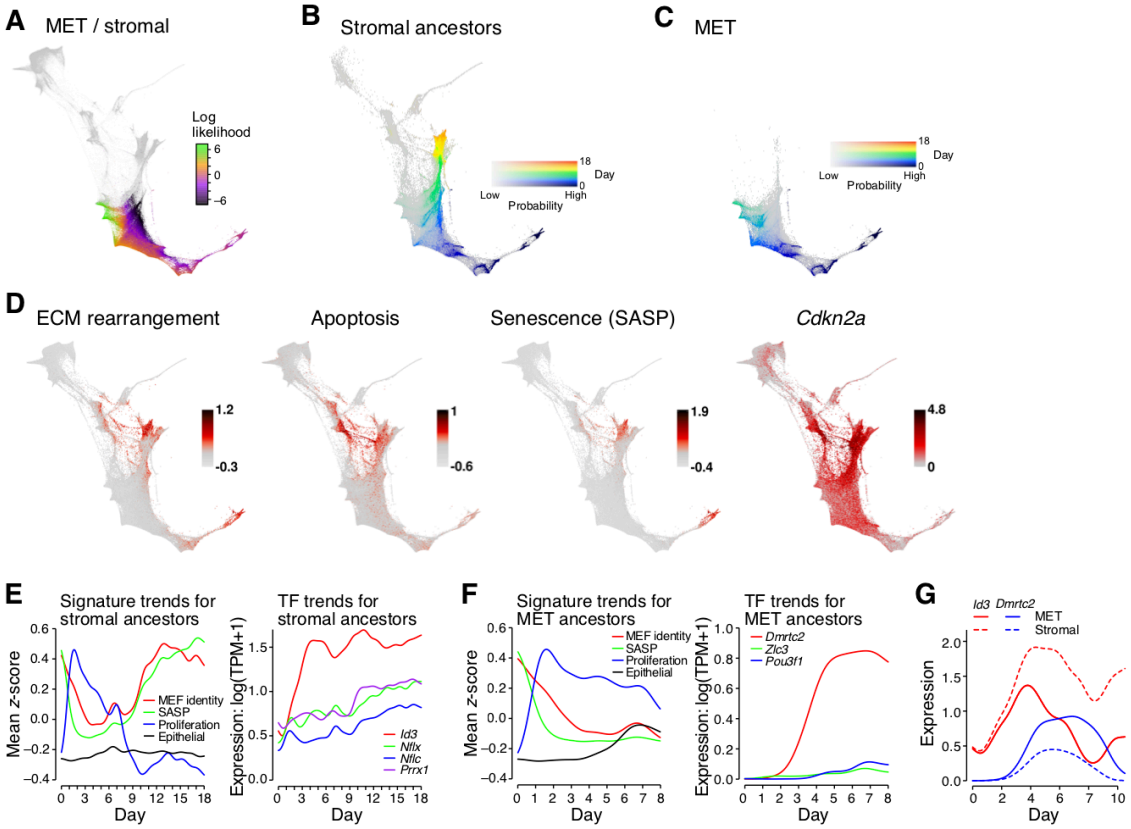
A
MET / stromal
Log likelihood
6
0
−6
B
Stromal ancestors
18
Day
0
Low
High
Probability
C
MET
18
Day
0
Low
High
Probability
D
ECM rearrangement
1.2
-0.3
Apoptosis
1
-0.6
Senescence (SASP)
1.9
-0.4
Cdkn2a
4.8
0
E
Signature trends for stromal ancestors
Mean z-score
MEF identity
SASP
Proliferation
Epithelial
Day
TF trends for stromal ancestors
Expression: log(TPM+1)
Id3
Nfix
Nfic
Prrx1
Day
F
Signature trends for MET ancestors
Mean z-score
MEF identity
SASP
Proliferation
Epithelial
Day
TF trends for MET ancestors
Expression: log(TPM+1)
Dmrtc2
Zic3
Pou3f1
Day
G
Id3 Dmrtc2
MET
Stromal
Expression
Day

Figure 4

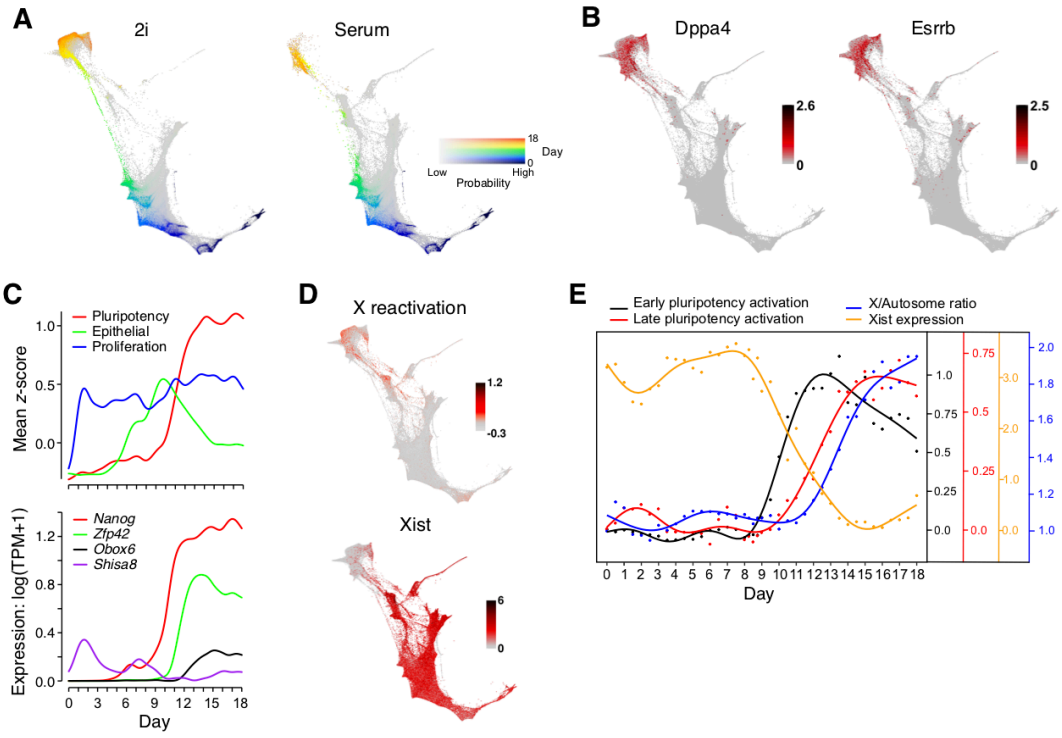
A
2i
Serum
18
Day
0
Low
High
Probability
B
Dppa4
2.6
0
Esrrb
2.5
0
C
Pluripotency
Epithelial
Proliferation
Mean z-score
1.0
0.5
0.0
Nanog
Zfp42
Obox6
Shisa8
Expression: log(TPM+1)
1.2
0.8
0.4
0.0
0 3 6 9 12 15 18
Day
D
X reactivation
1.2
-0.3
Xist
6
0
E
Early pluripotency activation
Late pluripotency activation
X/Autosome ratio
Xist expression
1.0
0.75
0.5
0.25
0.0
0.75
0.5
0.25
0.0
-3.0
-2.0
-1.0
-0.0
2.0
1.8
1.6
1.4
1.2
1.0
0 1 2 3 4 5 6 7 8 9 10 11 12 13 14 15 16 17 18
Day

Figure 5

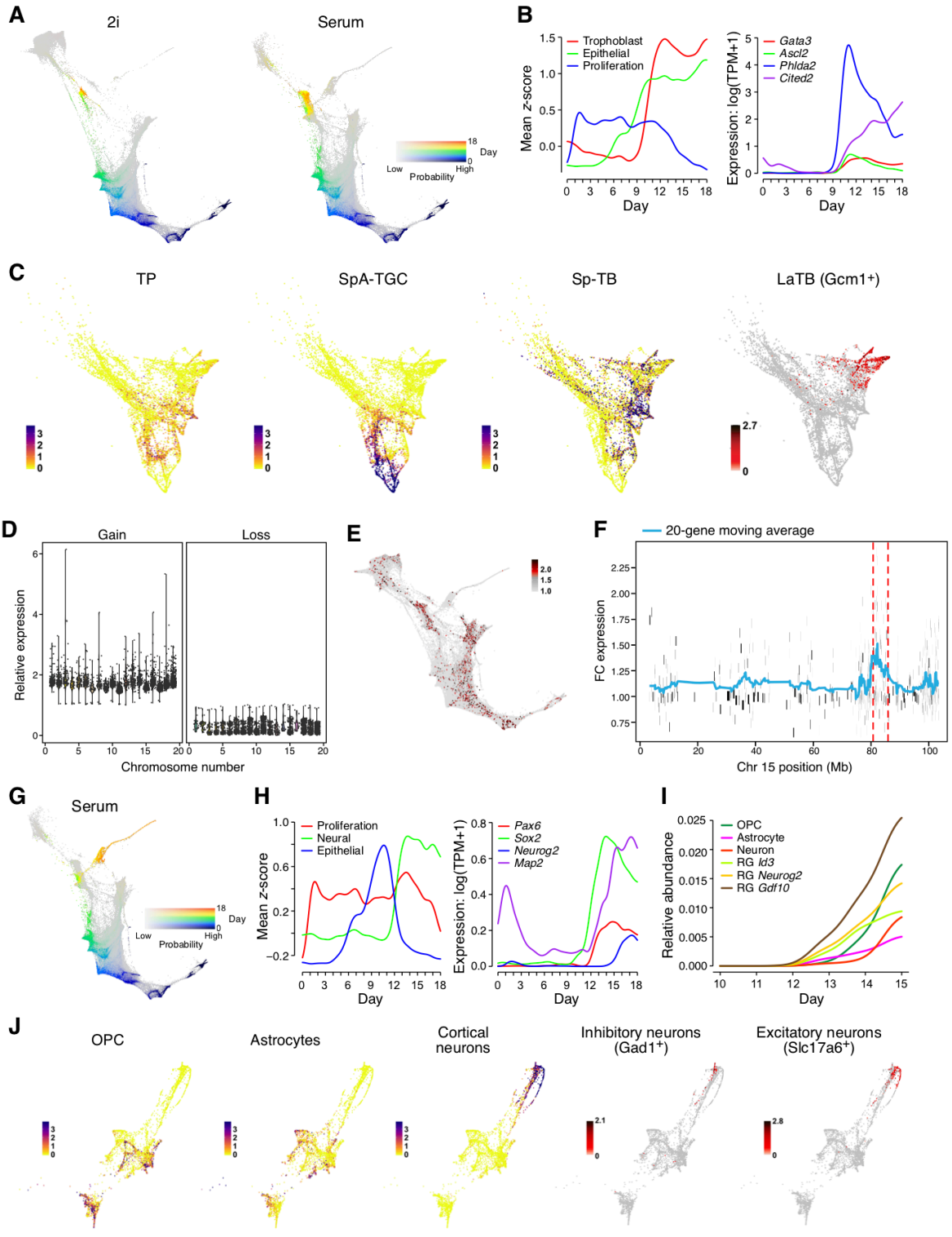
A
2i
Serum
Day
Low
High
Probability
B
Trophoblast
Epithelial
Proliferation
Mean z-score
Day
Gata3
Ascl2
Phlda2
Cited2
Expression: log(TPM+1)
C
TP
SpA-TGC
Sp-TB
LaTB (Gcm1+)
D
Gain
Loss
Relative expression
Chromosome number
E
F
20-gene moving average
FC expression
Chr 15 position (Mb)
G
Serum
H
Proliferation
Neural
Epithelial
Pax6
Sox2
Neurog2
Map2
I
OPC
Astrocyte
Neuron
RG Id3
RG Neurog2
RG Gdf10
Relative abundance
J
OPC
Astrocytes
Cortical neurons
Inhibitory neurons (Gad1+)
Excitatory neurons (Slc17a6+)

Figure 6

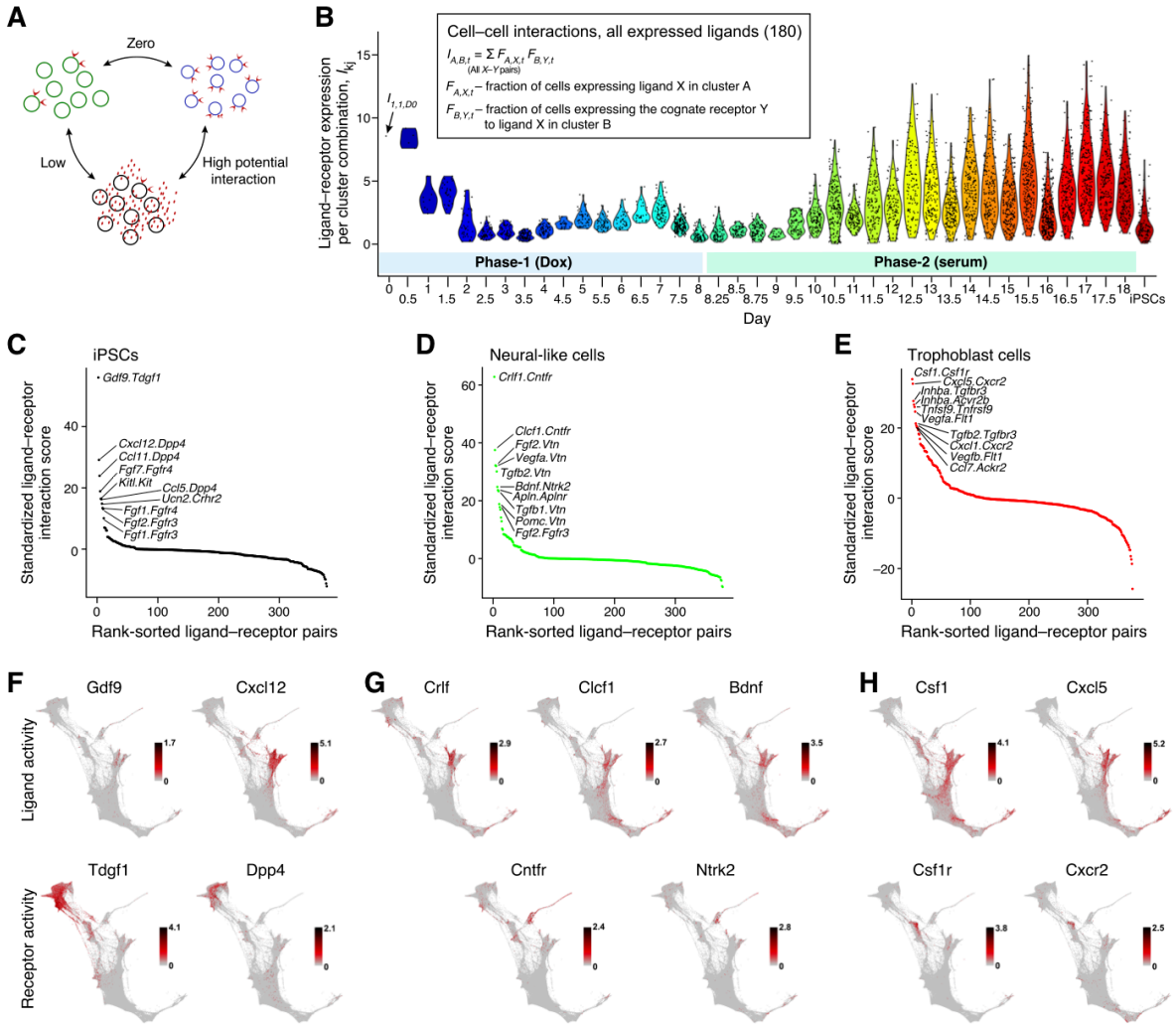
A
Zero
Low
High potential interaction
B
Cell–cell interactions, all expressed ligands (180)
$I_{A,B,t} = \sum_{(All\ X–Y\ pairs)} F_{A,X,t}\ F_{B,Y,t}$
$F_{A,X,t}$ – fraction of cells expressing ligand X in cluster A
$F_{B,Y,t}$ – fraction of cells expressing the cognate receptor Y to ligand X in cluster B
Ligand–receptor expression per cluster combination, I_{kj}
$I_{1,1,D0}$
Phase-1 (Dox)
Phase-2 (serum)
Day
iPSCs
Gdf9.Tdgf1
Cxcl12.Dpp4
Ccl11.Dpp4
Fgf7.Fgfr4
Kitl.Kit
Ccl5.Dpp4
Ucn2.Crhr2
Fgf1.Fgfr4
Fgf2.Fgfr3
Fgf1.Fgfr3
Standardized ligand–receptor interaction score
Rank-sorted ligand–receptor pairs
C
Neural-like cells
Crlf1.Cntfr
Clcf1.Cntfr
Fgf2.Vtn
Vegfa.Vtn
Tgfb2.Vtn
Bdnf.Ntrk2
Apln.Aplnr
Tgfb1.Vtn
Pomc.Vtn
Fgf2.Fgfr3
D
Trophoblast cells
Csf1.Csf1r
Cxcl5.Cxcr2
Inhba.Tgfbr3
Inhba.Acvr2b
Tnfsf9.Tnfrsf9
Vegfa.Flt1
Tgfb2.Tgfbr3
Cxcl1.Cxcr2
Vegfb.Flt1
Ccl7.Ackr2
E
F
Gdf9
Cxcl12
Ligand activity
Tdgf1
Dpp4
Receptor activity
G
Crlf
Clcf1
Bdnf
Cntfr
Ntrk2
H
Csf1
Cxcl5
Csf1r
Cxcr2

Figure 7

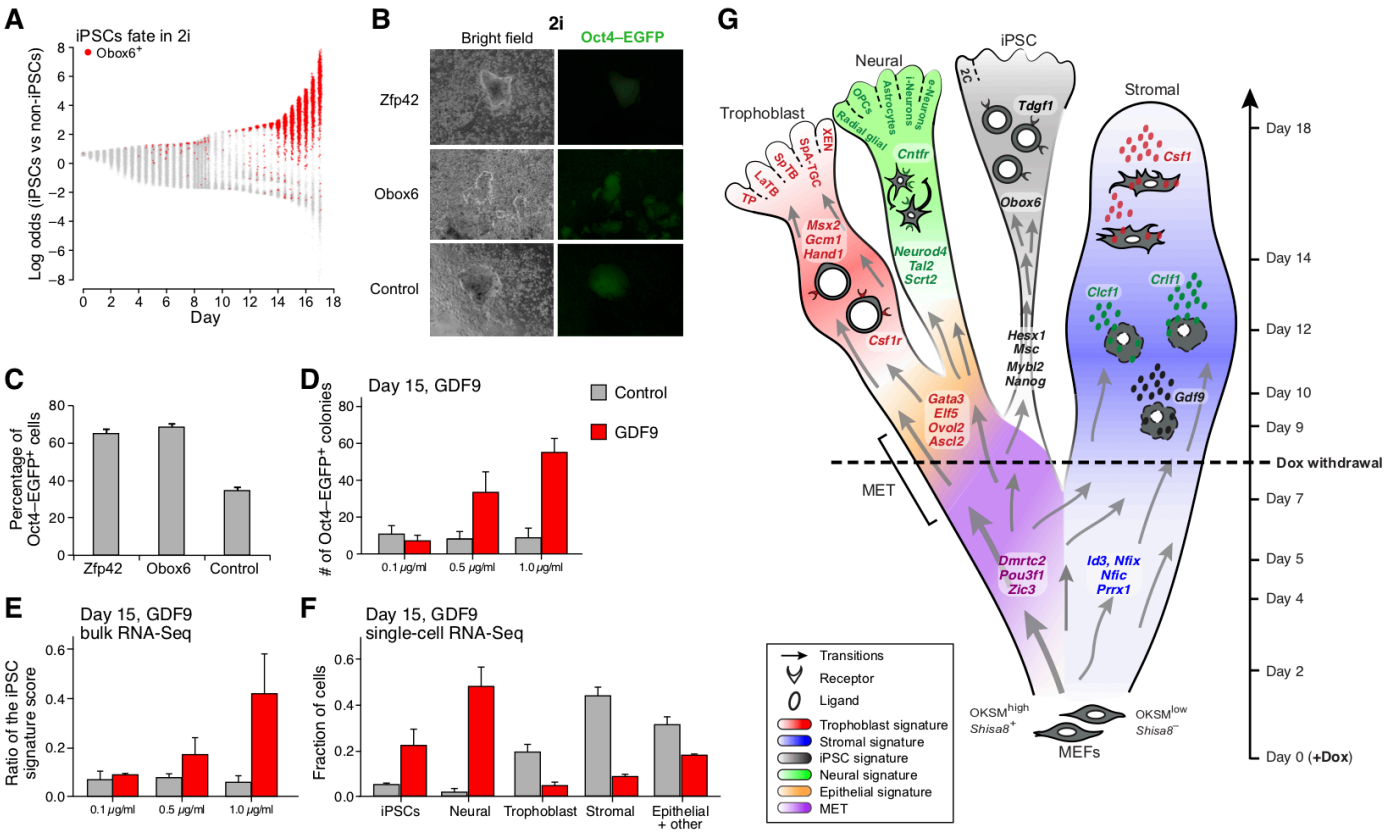
A
iPSCs fate in 2i
Obox6+
Log odds (iPSCs vs non-iPSCs)
Day
B
2i
Bright field
Oct4–EGFP
Zfp42
Obox6
Control
C
Percentage of Oct4–EGFP+ cells
Zfp42
Obox6
Control
D
Day 15, GDF9
# of Oct4–EGFP+ colonies
Control
GDF9
0.1 μg/ml
0.5 μg/ml
1.0 μg/ml
E
Day 15, GDF9
bulk RNA-Seq
Ratio of the iPSC signature score
F
Day 15, GDF9
single-cell RNA-Seq
Fraction of cells
iPSCs
Neural
Trophoblast
Stromal
Epithelial + other
G
Trophoblast
Neural
iPSC
Stromal
2C
Tdgf1
Obox6
Cntfr
Neurod4
Tal2
Scrt2
Msx2
Gcm1
Hand1
Csf1r
Gata3
Elf5
Ovol2
Ascl2
Hesx1
Msc
Mybl2
Nanog
Csf1
Clcf1
Crlf1
Gdf9
Dmrtc2
Pou3f1
Zic3
Id3, Nfix
Nfic
Prrx1
MET
Dox withdrawal
Day 18
Day 14
Day 12
Day 10
Day 9
Day 7
Day 5
Day 4
Day 2
Day 0 (+Dox)
OKSMhigh
Shisa8+
OKSMlow
Shisa8−
MEFs
Transitions
Receptor
Ligand
Trophoblast signature
Stromal signature
iPSC signature
Neural signature
Epithelial signature
MET

STAR Methods Outline

CONTACT FOR REAGENT AND RESOURCE SHARING

EXPERIMENTAL MODEL AND SUBJECT DETAILS

METHOD DETAILS

I. Modeling developmental processes with optimal transport

- *1. Developmental processes in gene expression space*
- *2. The optimal transport principle for developmental processes*
- *3. Inferring temporal couplings from empirical data*
- *4. Interpreting transport maps*

II. WADDINGTON-OT: Concepts and Implementation

- *1. Overview*
- *2. Computing transport maps*
- *3. Ancestors, descendants, and trajectories*
- *4. Learning gene regulatory models*
- *5. Geodesic interpolation for validation*

III. Experimental methods

- *1. Deriving secondary MEFs*
- *2. Deriving primary MEFs*
- *3. Reprogramming assay*
- *4. Sample collection*
- *5. Single-cell RNA sequencing*
- *6. Lentivirus Vector Construction and Particle Production*
- *7. Paracrine signaling assay*
- *8. Reprogramming efficiency of secondary MEFS together with individual TFs*
- *9. Reprogramming efficiency of primary MEFS with individual TFs and OKSM*

IV. Preparation of expression matrices

- *1. Read alignment*
- *2. Downsampling and filtering expression matrix*
- *3. Selecting variable genes*

V. Visualization: force-directed layout embedding (FLE)

VI. Creating gene signatures and cell sets

- *1. Gene signatures*
- *2. Cell sets*

VII. Estimating growth and death rates and computing transport maps

- *1. Initial estimate of growth rates*

CONTACT FOR REAGENT AND RESOURCE SHARING

Further information and requests for resources and reagents should be directed to the Lead Contact Eric Lander at lander@broadinstitute.org.

EXPERIMENTAL MODEL AND SUBJECT DETAILS

METHOD DETAILS

I. Modeling developmental processes with optimal transport

We developed a method to model development based on Optimal Transport. Section 1 reviews the concept of gene expression space and introduces our probabilistic framework for time series of expression profiles. Section 2 introduces our key modeling assumption to infer temporal couplings over short time scales. Section 3 shows how we can compute an optimal coupling between adjacent time points by solving a convex optimization problem, and how we can leverage an assumption of Markovity to compose adjacent time points and estimate temporal couplings over longer intervals. Section 4 describes how to interpret transport maps. Specifically, Section 4.1 shows how to compute ancestors and descendants of cells, and Section 4.3 shows how we learn gene regulatory networks to summarize the trajectories.

1. Developmental processes in gene expression space

A collection of mRNA levels for a single cell is called an *expression profile* and is often represented mathematically by a vector in *gene expression space*. This is a vector space that has dimension equal to the number of genes, with the value of the ith coordinate of an expression profile vector representing the number of copies of mRNA for the ith gene. Note that real cells only occupy an integer lattice in gene expression space (because the number of copies of mRNA is an integer), but we pretend that cells can move continuously through a real-valued G dimensional vector space.

As an individual cell changes the genes it expresses over time, it moves in gene expression space and describes a trajectory. As a population of cells develops and grows, a *distribution* on gene expression space evolves over time. When a single cell from such a population is measured with single cell RNA-seq, we obtain a noisy estimate of the number of molecules of mRNA for each gene. We represent the measured expression profile of this single cell as a sample from a probability distribution on gene expression space. This sampling captures both (a) the randomness in the measurement process (due to subsampling reads, technical issues, etc.) and (b) the random selection of a cell from the population. We treat this probability distribution as *nonparametric* in the sense that it is not specified by any finite list of parameters.

In the remainder of this section we introduce a precise mathematical notion for a *developmental process* as a special type of stochastic process (with a modified notion of coupling to accommodate cellular growth and death). Our primary goal is to infer the ancestors and descendants of subpopulations evolving according to an unknown developmental process. This information is encoded in the *temporal coupling* of the process, which is lost because we kill the cells when we perform scRNA-Seq. We claim it is possible to recover the temporal coupling over short time scales provided that cells don't change too much. We show in the remainder of this appendix how to do this with *optimal transport.*

1.1. A mathematical model of developmental processes

We begin by formally defining a precise notion of the developmental trajectory of an individual cell and its descendants. Intuitively, it is a continuous path in gene expression space that bifurcates with every cell division. Formally, we define it as follows:

Definition 1 (single-cell developmental trajectory)**.** *Consider a cell $x(0) \in \mathbb{R}^G$. Let $k(t) \geq 0$ specify the number of descendants at time t, where $k(0) = 1$. A single-cell developmental trajectory is a continuous*

function

$$x : [0, T) \to \underbrace{\mathbb{R}^G \times \mathbb{R}^G \times \ldots \times \mathbb{R}^G}_{k(t) \text{ times}}.$$

This means that $x(t)$ is a $k(t)$-tuple of cells, each represented by a vector in $\mathbb{R}^G$:

$$x(t) = \big(x_1(t), \ldots, x_{k(t)}(t)\big).$$

We refer to the cells $x_1(t), \ldots, x_{k(t)}(t)$ as the descendants of $x(0)$.

Note that we cannot directly measure the temporal dynamics of an individual cell because scRNA-Seq is a destructive measurement process: scRNA-Seq lyses cells so it is only possible to measure the expression profile of a cell at a single point in time. As a result, it is not possible to directly measure the descendants of that cell, and the full trajectory is unobservable. However, one can hope to learn something about the probable trajectories of individual cells by measuring snapshots from an evolving population.

Published methods typically represent the aggregate trajectory of a population of cells by means of a graph structure. While this recapitulates the branching path traveled by the descendants of an individual cell, it may over-simplify the stochastic nature of developmental processes. Individual cells have the potential to travel through different paths, but any given cell travels one and only one such path. Our goal is to assign a likelihood to the set of possible paths, which in general are not finite and therefore cannot be a represented by a graph.

We define a developmental process to be a time-varying probability distribution on gene expression space. One simple example of a distribution of cells is that we can represent a set of cells $x_1, \ldots, x_n$ by the distribution

$$\mathbb{P} = \frac{1}{n} \sum_{i=1}^{n} \delta_{x_i},$$

where δ_x denote the Dirac delta (a distribution placing unit mass on x). Similarly, we can represent a set of single-cell trajectories $x_1(t), \ldots, x_n(t)$ with a distribution over trajectories. This is a special case of a developmental process, which we define as follows:

Definition 2 (developmental process)**.** *A developmental process $\mathbb{P}_t$ is a time-varying distribution (i.e. stochastic process) on gene expression space.*

Recall that a stochastic process is determined by its temporal dependence structure. This is specified by the coupling (i.e. joint distribution) between random variables at different time points. Given that a cell has a particular expression profile y at time t_2, where did it come from at time t_1? This is precisely the information lost by not tracking individual cells over time.

Definition 3 (temporal coupling)**.** *Let $\mathbb{P}_t$ be a developmental process and consider two time points $s < t$. Let $X_t \sim \mathbb{P}_t$ denote the expression profile of a random cell at time t and let X_s denote the expression profile of its cell of origin at time s.*

The temporal coupling $\gamma_{s,t}$ is defined as the law of the joint distribution:

$$\gamma_{s,t} = \mathcal{L}(X_s, X_t).$$

Equivalently,

$$\int_{x \in A} \int_{y \in B} \gamma_{s,t}(x, y) dx dy = \Pr\{X_s \in A, X_t \in B\}$$

for any sets $A, B \subset \mathbb{R}^G$.

The temporal coupling $\gamma_{s,t}$ is not technically a coupling of $\mathbb{P}_s$ and $\mathbb{P}_t$ in the standard sense because it does not necessarily have marginals $\mathbb{P}_s$ and $\mathbb{P}_t$:

$$\int \gamma_{s,t}(x,y)dx = \mathbb{P}_t(y), \quad \text{but} \quad \int \gamma_{s,t}(x,y)dy \neq \mathbb{P}_s(x).$$

Biologically, this is the case when cells grow at different rates. Then proliferative cells from the earlier time point will be over-represented when we look for the origin of cells at the later time point. In the following definition, we introduce a relative growth rate function to describe the relationship between the expression profile of a cell and the average number of living descendants it gives rise to after certain amount of time.

Definition 4. *A relative growth rate function associated with a temporal coupling is a function $g(x)$ satisfying*

$$\int \gamma_{s,t}(x,y)dy = \mathbb{P}_s(x)\frac{g(x)^{t-s}}{\int g(x)^{t-s}d\mathbb{P}_s(x)}.$$

The integral on the left-hand side represents the amount of mass coming out of x and going to any y. The term $\mathbb{P}(x)$ on the right hand side accounts for the abundance of cells with expression profile x, and the function $g(x)$ represents the exponential increase in mass per unit time.

Having defined the notion of developmental processes and temporal couplings, we now turn to estimating these from data.

2. The optimal transport principle for developmental processes

ScRNA-Seq allows us to sample cells from a developmental process at various time points, but it does not give any information about the coupling between successive time points. Without making any assumptions, it is impossible to recover the temporal coupling even given infinite data in the form of the full distributions $\mathbb{P}_s$ and $\mathbb{P}_t$. However, we claim that it is reasonable to assume that cells don't change expression by large amounts over short time scales. This assumption allows us to estimate the coupling and infer which cells go where.

We begin with a simple one-dimensional example to build intuition.

Example 1. *Let $X_0 \sim \mathcal{N}(0,\sigma^2)$ and $X_1 \sim \mathcal{N}(\mu,\sigma^2)$ be one dimensional Gaussian variables representing the location of a particle at time 0 and at time 1. If we believe that the particle cannot move very far over a short amount of time, then how can we infer the coupling γ specifying the joint distribution of the pair (X_0, X_1)? One simple heuristic to estimate $\hat{\gamma}$ is to minimize the squared distance that the particle moves from time 0 to time 1:*

$$\hat{\gamma} \leftarrow \arg\min_{\pi} \ \mathbb{E}_\pi \|X_0 - X_1\|^2.$$

We minimize over all couplings π with marginals $\mathcal{N}(0,\sigma^2)$ and $\mathcal{N}(\mu,\sigma^2)$. One can check that the optimal joint distribution is a two dimensional Gaussian with the following dependence structure:

$$X_1 = X_0 + \mu.$$

This heuristic to couple marginals is called *optimal transport* (OT) (Villani, 2008). If $c(x,y)$ denotes the cost of transporting a unit mass from x to y, and the amount we transfer from x to y is $\pi(x,y)$, then the total cost of transporting mass according to such a transport plan π is given by

$$\iint c(x,y)\pi(x,y)dxdy.$$

In this paper we focus exclusively on the cost defined by the squared-Euclidean distance

$$c(x, y) = \|x - y\|^2,$$

on an appropriate input space (see the section **Waddington-OT: Concepts and Implementation** for details). We make this choice to focus on this cost function because of the many well-known attractive theoretical properties it enjoys over other cost functions (Villani, 2008).

The *optimal* transport plan minimizes the expected cost subject to marginal constraints:

$$\begin{aligned} \pi(\mathbb{P}, \mathbb{Q}) = \underset{\pi}{\text{minimize}} \quad & \iint c(x, y)\pi(x, y)dxdy \\ \text{subject to} \quad & \int \pi(x, \cdot)dx = \mathbb{Q} \\ & \int \pi(\cdot, y)dy = \mathbb{P}. \end{aligned} \tag{1}$$

Note that this is a linear program in the variable π because the objective and constraints are both linear in π. The optimal objective value defines the *transport distance* between $\mathbb{P}$ and $\mathbb{Q}$ (it is also called the Earthmover's distance or Wasserstein distance). Unlike many other ways to compare distributions (such as KL-divergence or total variation), optimal transport takes the geometry of the underlying space into account. For example, the KL-Divergence is infinite for any two distributions with disjoint support, but the transport distance depends on the separation of the support. For a comprehensive treatment of the rich mathematical theory of optimal transport, we refer the reader to (Villani, 2008).

2.1. The optimal transport principle

We propose to use optimal transport to estimate the temporal coupling of a developmental process. We make two modifications to classical optimal transport to adapt it to our biological setting.

1. Classical optimal transport has conservation of mass built into the constraints (1). We account for growth by rescaling the distribution $\mathbb{P}_t$ before applying OT.

2. The coupling identified by classical optimal transport is purely deterministic in the sense that each point is transported to a single point[1]. However, for cells whose fates are not completely determined, the true coupling should have a degree of entropy to it. We therefore add a term to the objective to promote entropy in the transport coupling.

   Injecting a small amount of entropy also makes sense even for a population of cells with truly deterministic descendant distribution. When we sample finitely many cells at time t_2, the true descendants of any given t_1 cell are not captured. Therefore entropy in the transport map can be used to represent our statistical uncertainty in the inferred descendant distribution.

In order to state the optimal transport principle, we first introduce some notation. Let $\mathbb{P}_t$ denote a developmental process with temporal coupling $\gamma_{s,t}$ and with relative growth function $g(x)$. Let $\mathbb{Q}_s$ denote the distribution obtained by rescaling $\mathbb{P}_s$ by the relative growth rate:

$$\mathbb{Q}_s(x) = \mathbb{P}_s(x)\frac{g^{t-s}(x)}{\int g^{t-s}(z)d\mathbb{P}_s(z)}.$$

[1] There may be non-deterministic plans achieving the same cost (e.g. if all points are equidistant), but there is always an optimal plan that is deterministic.

Finally, let $\pi_{s,t}(\epsilon)$ denote the entropy-regularized optimal transport coupling of $\mathbb{Q}_s$ and $\mathbb{P}_t$, defined as the solution to the following optimization problem:

$$\begin{aligned} \pi_{s,t}(\epsilon) = \underset{\pi}{\text{minimize}} \quad & \iint c(x,y)\pi(x,y)dxdy - \epsilon \iint \pi(x,y)\log\pi(x,y)dxdy \\ \text{subject to} \quad & \int \pi(x,\cdot)dx = \mathbb{Q}_s \\ & \int \pi(\cdot,y)dy = \mathbb{P}_t. \end{aligned} \tag{2}$$

We now state the optimal transport principle for developmental processes:

$$s \approx t \implies \pi_{s,t}(\epsilon) \approx \gamma_{s,t}.$$

In words, over short time scales, the true coupling is well approximated by the OT coupling. In section 3, we show how to estimate $\pi_{s,t}(\epsilon)$ from data (we occasionally omit the dependence on ϵ and write $\pi_{s,t}$). This in turn gives us an estimate of $\gamma_{s,t}$.

3. Inferring temporal couplings from empirical data

In this section we show how to estimate the temporal couplings of a developmental process from data.

Definition 5 (developmental time series)**.** *A developmental time series is a sequence of samples from a developmental process $\mathbb{P}_t$ on $\mathbb{R}^G$. This is a sequence of sets $S_1, \ldots, S_T \subset \mathbb{R}^G$ collected at times $t_1, \ldots, t_T \in \mathbb{R}$. Each S_i is a set of expression profiles in $\mathbb{R}^G$ drawn independently from $\mathbb{P}_{t_i}$.*

From this input data, we form an empirical version of the developmental process. Specifically, at each time point t_i we form the empirical probability distribution supported on the data $x \in S_i$. We summarize this in the following definition:

Definition 6 (Empirical developmental process)**.** *An empirical developmental process $\hat{\mathbb{P}}_t$ is a time varying distribution constructed from a developmental time course $S_1, \ldots, S_T$:*

$$\hat{\mathbb{P}}_{t_i} = \frac{1}{|S_i|}\sum_{x \in S_i} \delta_x. \tag{3}$$

The empirical developmental process is undefined for $t \notin \{t_1, \ldots, t_T\}$.

In order to estimate the coupling from time t_1 to time t_2, we first construct an initial estimate of the growth rate function $g(x)$. In practice, we form an initial estimate $\hat{g}(x)$ as the expectation of a birth-death process on gene expression space with birth-rate $\beta(x)$ and death rate $\delta(x)$ defined in terms of expression levels of genes involved in cell proliferation and apoptosis (see **Estimating birth and death rates and computing transport maps**). We ultimately leverage techniques from *unbalanced transport* (Chizat et al., 2018) to refine this initial estimate to learn cellular growth and death rates automatically from data (see **Waddington-OT: Concepts and Implementation**).

We then form the rescaled empirical distribution

$$\hat{\mathbb{Q}}_{t_1}(x) = \hat{\mathbb{P}}_{t_1}(x)\frac{\hat{g}(x)^{t_1 - t_2}}{\int \hat{g}(z)^{t_1-t_2} d\hat{\mathbb{P}}_{t_i}(z)},$$

and compute the optimal transport map $\hat{\pi}_{t_1,t_2}$ between $\hat{\mathbb{Q}}_{t_1}$ and $\hat{\mathbb{P}}_{t_2}$.

3.1. Estimating couplings between adjacent time points

In order to identify an optimal transport plan connecting $\hat{\mathbb{Q}}_{t_1}$ and $\hat{\mathbb{P}}_{t_2}$, we must solve an optimization problem with a matrix-valued optimization variable. In the classical zero-entropy setting, the optimization problem (2) is a linear program (when $\epsilon = 0$). While the classical optimal transport linear program can be difficult to solve for large numbers of points, fast algorithms have been recently developed (Cuturi, 2013) to solve the entropically regularized version of the transport program. Entropic regularization speeds up the computations because it makes the optimization problem strongly convex, and gradient ascent on the dual can be realized by successive diagonal matrix scalings called Sinkhorn iterations (Cuturi, 2013). These are very fast operations.

The scaling algorithm for entropically regularized transport has also been extended to work in the setting of **unbalanced transport** (Chizat et al., 2018), where the equality constraints are relaxed to bounds on the marginals of the transport plan (in terms of KL-divergence or total variation or a general f-divergence). In our application this is very attractive from a modeling perspective for the following reasons:

1. We may have misspecified the growth rate function $\hat{g}(x)$. Unbalanced transport adjusts the input growth rate in order to reduce the transport cost. This allows us to automatically learn growth rates from scratch (see **Waddington-OT: Concepts and Implementation**).

2. Even if the growth rates are completely uniform, the random sampling can introduce what looks like growth. For example, suppose there is a rare subpopulation of cells consisting of 5% of the total. If at one time point, we randomly sample fewer of these cells so that they comprise 4% of the total, and at the next time point we sample 6%, then it will look like this population has increased by 50%. Unbalanced transport can automatically adjust for this apparent growth.

We use both entropic regularization and unbalanced transport. To compute the transport map between the empirical distributions of expression profiles observed at time t_i and t_{i+1}, we solve the following optimization problem:

$$\begin{aligned}\hat{\pi}_{t_i,t_{i+1}} \;=\; \arg\min_{\pi} \quad & \sum_{x\in S_i}\sum_{y\in S_{i+1}} c(x,y)\pi(x,y) - \epsilon \iint \pi(x,y)\log\pi(x,y)dxdy \\ & + \lambda_1 \mathrm{KL}\left[\sum_{x\in S_i}\pi(x,y)\middle\| d\hat{\mathbb{P}}_{t_{i+1}}(y)\right] + \lambda_2 \mathrm{KL}\left[\sum_{y\in S_{i+1}}\pi(x,y)\middle\| d\hat{\mathbb{Q}}_{t_i}(x)\right]\end{aligned} \tag{4}$$

where ϵ, λ_1 and λ_2 are regularization parameters. We provide guidelines for tuning these parameters in **Waddington-OT: Concepts and Implementation**.

This is a convex optimization problem in the matrix variable $\pi \in \mathbb{R}^{N_i \times N_{i+1}}$, where $N_i = |S_i|$ is the number of cells profiled at time t_i. It takes about 5 seconds to solve this unbalanced transport problem using the scaling algorithm of (Chizat et al., 2018) on a standard laptop with $N_i \approx 5000$.

Note that by default the densities (on the discrete set S_i) of the empirical distributions specified in equation (3) are simply $d\hat{\mathbb{P}}_{t_i}(x) = \frac{1}{N_i}$. However, in principle one could use nonuniform empirical distributions (e.g. if one wanted to include information about cell quality).

To summarize: given a sequence of expression profiles $S_1, \ldots, S_T$, we solve the optimization problem (4) for each successive pair of time points S_i, S_{i+1}. For the pair of time-points (t_i, t_{i+1}), this gives us a transport map $\hat{\pi}_{t_i,t_{i+1}}$. When we have enough data, this is a good estimate of $\pi_{t_i,t_{i+1}}$ because it is well known that transport maps are consistent in the sense that

$$\lim_{N_i,N_{i+1}\to\infty} \hat{\pi}_{t_i,t_{i+1}} = \pi_{t_i,t_{i+1}}.$$

Taken together with the optimal transport principle:

$$\pi_{t_i,t_{i+1}} \approx \gamma_{t_i,t_{i+1}},$$

we therefore can estimate $\gamma_{t_i,t_{i+1}}$ from $\hat{\pi}_{t_i,t_{i+1}}$ when N_i is large enough.

3.2. Estimating long-range couplings

We rely on an assumption of Markovity (or memorylessness) in order to estimate couplings over longer time intervals. Recall that a stochastic process is Markov if the future is independent of the past, given the present. Equivalently, it is fully specified by the couplings between pairs of time points. We define Markov developmental processes in a similar spirit:

Definition 7 (Markov developmental process)**.** *A Markov developmental process $\mathbb{P}_t$ is a time-varying distribution on $\mathbb{R}^G$ that is completely specified by couplings between pairs of time points in the following sense. For any three time points $s < t < \tau$, the long-range coupling $\gamma_{s,\tau}$ is equal to the composition of short-range couplings:*

$$\gamma_{t,\tau} \circ \gamma_{s,t} = \gamma_{s,\tau}.$$

Note that the optimal transport maps $\hat{\pi}_{s,t}$ do **not** necessarily have this compositional property! Composing the OT coupling from time s to t and then from t to τ is not the same as optimally transporting from s directly to τ. In general, we do not recommend computing OT maps directly between distant time points.

We leverage the Markovity assumption to estimate couplings over long time intervals by composing estimates over shorter intervals. Formally, for any pair of time points t_i, t_{i+k}, we estimate the coupling $\hat{\gamma}_{t_i,t_{i+k}}$ by composing as follows:

$$\hat{\gamma}_{t_i,t_{i+k}} = \hat{\pi}_{t_i,t_{i+1}} \circ \hat{\pi}_{t_{i+1},t_{i+2}} \circ \ldots \circ \hat{\pi}_{t_{i+k-1},t_{i+k}}.$$

These compositions are computed via ordinary matrix multiplication.

It is an interesting question to what extent developmental processes are Markov. On gene expression space, they are likely not strictly Markov because, for example, the history of gene expression can influence chromatin modifications, which may not themselves be fully reflected in the observed expression profile but could still influence the subsequent evolution of the process. However, it is possible that developmental processes could be considered Markov on some augmented space.

4. Interpreting transport maps

In the previous section we introduced the principle of optimal transport for time series of gene expression profiles. Given a time series of expression profiles $S_1, \ldots, S_T$, we use this principle to compute a sequence of transport maps between subsequent time slices. In this section we define the *ancestors* and *descendants* of any subset of cells from this sequence of transport maps in section 4.1. Finally, in section 4.3 we describe a connection between optimal transport, gradient flows, and Waddington's landscape.

4.1. Defining ancestors, descendants and trajectories

We now define the descendants and ancestors of subgroups of cells evolving according to a Markov (i.e. memoryless) developmental process.

Our definition of ancestors and descendants relies on a notion of *pushing* sets of cells through a transport map. Before defining ancestors and descendants, we introduce this terminology. As a distribution on the product space $\mathbb{R}^G \times \mathbb{R}^G$, a coupling γ assigns a number $\gamma(A, B)$ to any pair of sets $A, B \subset \mathbb{R}^G$

$$\gamma(A, B) = \int_{x \in A} \int_{y \in B} \gamma(x, y) dx dy.$$

This number $\gamma(A, B)$ represents the amount of mass coming from A and going to B. When we don't specify a particular destination, the quantity $\gamma(A, \cdot)$ specifies the full distribution of mass coming from A. We refer to this action as *pushing* A through the transport plan γ. More generally, we can also push a *distribution* μ forward through the transport plan γ via integration

$$\mu \mapsto \int \gamma(x, \cdot) d\mu(x).$$

We refer to the reverse operation as pulling a set B back through γ. The resulting distribution $\gamma(\cdot, B)$ encodes the mass ending up at B. We can also pull distributions μ back through γ in a similar way:

$$\mu \mapsto \int \gamma(\cdot, y) d\mu(y).$$

We sometimes refer to this as *back-propagating* the distribution μ (and to pushing μ forward as *forward propagation*).

Equipped with this terminology, we define ancestors and descendants as follows:

Definition 8 (descendants in a Markov developmental process)**.** *Consider a set of cells $C \subset \mathbb{R}^G$, which live at time t_1 are part of a population of cells evolving according to a Markov developmental process $\mathbb{P}_t$. Let γ_{t_1,t_2} denote the coupling from time t_1 to time t_2. The descendants of C at time t_2 are obtained by pushing C through γ.*

Definition 9 (ancestors in a Markov developmental process)**.** *Consider a set of cells $C \subset \mathbb{R}^G$, which live at time t_2 and are part of a population of cells evolving according to a Markov developmental process $\mathbb{P}_t$. Let π denote the transport map for $\mathbb{P}_t$ from time t_2 to time t_1. The ancestors of C at time t_1 are obtained by pulling C back through γ.*

Trajectories: We define to the *ancestor trajectory* to a set C as the sequence of ancestor distributions at earlier time points. Similarly, we refer to the *descendant trajectory* from a set C as the sequence of descendant distributions at later time points.

4.2. Interpreting the entropy regularization parameter

In this section we explain a physical interpretation of entropy-regularized optimal transport.

Consider a collection of N indistinguishable particles undergoing Brownian motion with diffusion coefficient ϵ. Suppose we observe the positions of N particles at times 0 and 1. But because the particles are indistinguishable, we don't know which particle at time 0 corresponds to each particle at time 1. If $N = 1$, this is of course not an issue, and the distribution on paths connecting the starting and ending point is called a *Brownian bridge*.

For $N > 1$, the distribution over possible paths connecting the starting and ending points involves two components:

1. A coupling of the particles specifying which particle goes where (because the particles are indistinguishable, this is not uniquely specified by the observations).

2. Given a matching, the distribution on paths for each matched pair is a Brownian bridge.

The coupling is a random permutation that matches points at time 0 to points at time 1. The distribution of this random permutation depends on the variance (or diffusion coefficient) of the Brownian motion. If the diffusion coefficient is larger, then it is more likely that particles will swap positions over larger distances. It turns out that the expected (i.e. average) coupling can be computed by maximum entropy optimal transport. These ideas can be traced back to Schrodinger's 1932 work in statistical electrodynamics (Schrodinger, 1932), but the connection to optimal transport was not made explicit until recently (Cuturi, 2013; Léonard, 2014). We summarize this in the following theorem:

Theorem 1. *Entropy regularized optimal transport gives the expectation of the distribution over couplings induced by Brownian motion, when the diffusion coefficient of the Brownian motion is equal to the entropy regularization parameter.*

4.3. Gradient flow and Waddington's landscape

In this section we show how optimal transport can be interpreted as a gradient flow in gene expression space (capturing cell-autonomous processes) or in the space of distributions (capturing cell-nonautonomous processes). For a full treatment of the rich OT theory of gradient flows, we refer the reader to (Ambrosio et al., 2005; Santambrogio, 2015).

We begin by considering the simple setting described by Waddington's landscape, which describes a gradient flow in gene expression space and is a special case of what we can capture with optimal transport. Mathematically, Waddington's landscape defines a potential function Φ assigning potential energy $\Phi(x)$ to a cell with expression profile x. The cells roll downhill according to the gradient of Φ to describe a trajectory $x(t)$ satisfying the differential equation

$$\frac{dx}{dt} = -\nabla\Phi(x). \tag{5}$$

This equation governing the trajectory of individual cells induces a flow in the distribution of the population of cells:

$$\frac{d\mathbb{P}_t}{dt} = \text{div}[\nabla\Phi(x)\mathbb{P}_t]. \tag{6}$$

Intuitively, this equation states that the change in mass for each small volume of space (on the left-hand side) is equal to the flux of mass in and out (given by the divergence on the right hand side).

Optimal transport can capture this type of potential driven dynamics: the true coupling specified by (5) is close to the optimal transport coupling over short time scales. To motivate this, we appeal to a classical theorem establishing a dynamical formulation of optimal transport.

Theorem 2 (Benamou and Brenier, 2001)**.** *The optimal objective value of the transport problem* (1) *is equal to the optimal objective value of the following optimization problem:*

$$\begin{aligned} \underset{\rho,v}{\text{minimize}} \quad & \int_0^1 \int_{\mathbb{R}^G} \|v(t,x)\|^2 \rho(t,x)\,dt\,dx \\ \text{subject to} \quad & \rho(0,\cdot) = \mathbb{P}, \quad \rho(1,\cdot) = \mathbb{Q} \\ & \nabla\cdot(\rho v) = \frac{\partial\rho}{\partial t} \end{aligned} \quad . \tag{7}$$

In this theorem, v is a vector-valued velocity field that advects[2] the distribution ρ from $\mathbb{P}$ to $\mathbb{Q}$, and the objective value to be minimized is the kinetic energy of the flow (mass $\times$ squared velocity). In our

[2] *Advection*, a term borrowed from fluid mechanics, refers to the transport of a substance by bulk motion. The constraint that the divergence of the flow is equal to the rate of change of ρ means that ρ flows according to the velocity field v, without gaining or losing mass.

setting, the two distributions are snapshots $\mathbb{P}_s$ and $\mathbb{P}_t$ of a developmental process at two time points, and the theorem shows that the transport map $\pi_{s,t}$ can be seen as a point-to-point summary of a least-action continuous time flow, according to an unknown velocity field. In the special case when the velocity field is the gradient of a potential Φ (i.e. Waddington landscape), the theorem implies that the coupling (5) achieves the optimal transport cost. In other words, OT can capture potential driven dynamics. In addition, optimal transport can also describe much more general settings. This velocity field could change over time and also depend on the entire distribution of cells, so optimal transport can describe very general developmental processes including those with cell-cell interactions, as we describe below.

We will show that the evolution (6) is a special case of a *Wasserstein gradient flow* to minimize the linear energy functional

$$E(\mathbb{P}) = \int \Phi(x) d\mathbb{P}(x).$$

We will then describe non-linear gradient flows, which can capture cell-cell interactions.

To understand gradient flows, let's start with the familiar notion of gradient descent:

$$x_{k+1} = -\eta \nabla E(x_k) + x_k.$$

This can be rewritten as a *proximal procedure*, where one seeks to minimize E over all x in the proximity of x_k:

$$x_{k+1} = \quad \arg\min_x \qquad E(x) + \frac{1}{2\eta}\|x - x_k\|^2. \tag{8}$$

We can perform a similar proximal procedure in the space of distributions, replacing the Euclidean norm $\|\cdot\|^2$ with the Wasserstein distance:

$$\mathbb{P}_{k+1} = \quad \arg\min_\rho E(\rho) + \frac{1}{2\eta} W_2^2(\rho, \mathbb{P}_k). \tag{9}$$

This produces a sequence of iterates $\mathbb{P}_0, \mathbb{P}_1, \ldots, \mathbb{P}_k$. The gradient flow is the limit obtained as we shrink the step-size $\eta \downarrow 0$. In (Jordan et al., 1998), it's proven that for the linear energy functional

$$E(\mathbb{P}) = \int \Phi(x) d\mathbb{P}(x),$$

the limiting gradient flow converges to a solution of (6).

Going beyond the linear energy functional associated with Waddington's landscape, one could describe cell-cell interactions with an interaction energy of the form

$$E(\mathbb{P}) = \iint I(x, y) d\mathbb{P}(x) d\mathbb{P}(y).$$

Gradient flows for interaction potentials are discussed in chapter 7 of (Santambrogio, 2015).

Learning models of gene regulation Motivated by this interpretation of optimal transport as a gradient flow according to an unknown vector field, we describe a strategy to estimate such a vector field from data in **Waddington-OT: Concepts and Implementation**. We interpret the vector field as a model of gene regulation – it predicts gene expression at later time points as a function of transcription factor expression at current time points. We assume that the vector field does not change over time, and describes a cell-autonomous flow, but we do not assume that it comes from a potential function.

II. WADDINGTON-OT : Concepts and Implementation

Building on the theoretical foundations developed in Modeling developmental processes with optimal transport, we developed WADDINGTON-OT: our method for computing ancestor and descendant trajectories, interpolating developmental processes, inferring gene regulatory models, and visualizing developmental landscapes. We begin with an overview in Section 1, and we then describe the specific details in Sections 2 - 8.

1. Overview

To apply WADDINGTON-OT to a dataset, we pursue the following steps. The code is available on GitHub:

`https://github.com/broadinstitute/wot/`

Specifically, in the sections below we describe our procedures for

- computing transport maps
- computing trajectories to cell sets
- fiting local and global regulatory models
- interpolating the distribution of cells at held-out time points.

To keep the focus here general-purpose, we defer all reprogramming-specific details to the subsequent sections of STAR Methods.

Input data: The input to our suite of methods is a temporal sequence of single cell gene expression matrices, prepared as described in **Preparation of expression matrices**.

Computing transport maps: Waddington-OT calculates transport maps between consecutive time points and automatically estimates cellular growth and death rates. In Section 2 below we provide guidelines for defining the cost function, selecting regularization parameters and (optionally) providing an initial estimate of growth and death rates.

Ancestors, descendants, and trajectories: We describe in Section 3 how we compute trajectories plot trends in gene expression. Briefly, the *developmental trajectory* of a subpopulation of cells refers to the sequence of ancestors coming before it and descendants coming after it. Using the transport maps, we can calculate the forward or backward transport probabilities between any two classes of cells at any time points. For example, we can take successfully reprogrammed cells at day 18 and use back-propagation to infer the distribution over their precursors at day 17.5. We can then propagate this back to day 17, and so on to obtain the ancestor distributions at each previous time point. This is the developmental trajectory to iPS cells. We can then readily plot trends in gene expression over time.

Fitting regulatory models: We describe our method to fit a regulatory model to the transport maps in Section 4. Transcription factors (TFs) that appear to play important roles along trajectories to key destinations are identified by two approaches. The first approach involves constructing a global regulatory model, related to the framework we describe in Section I.4.2. Pairs of cells at consecutive time points are sampled according to their transport probabilities; expression levels of TFs in the cell at time t are used to predict expression levels of all non-TFs in the paired cell at time $t + 1$, under the assumption that the regulatory rules are constant across cells and time points. (TFs are excluded from the predicted set to avoid cases of spurious self-regulation). The second approach involves local enrichment analysis. TFs are identified based on enrichment in cells at an earlier time point with a high probability ($> 80\%$) of transitioning to a given fate vs. those with a low probability ($< 20\%$).

Geodesic interpolation: To validate the temporal couplings, Waddington-OT can interpolate the distribution of cells at a held-out time point. The method is performing well if the interpolated distribution is close to the true held-out distribution (compared to the distance between different batches of the held-out distribution). Otherwise, it is possible that the method requires more data or finer temporal resolution.

Section 5 describes our method to interpolate the distribution of cells at a held-out time point. The specific application for validation of our method on iPS reprogramming data is presented in the subsequent section on **Validation by geodesic interpolation**. We performed extensive sensitivity analysis to show that our temporal couplings produce valid interpolations over a wide range of parameter settings perturbations to the data (downsampling cells or reads). See **QUANTIFICATION AND STATISTICAL ANALYSIS** for this sensitivity analysis.

2. Computing transport maps

Recall that for any pair of time points we compute a transport plan that minimizes the expected cost of redistributing mass, subject to constraints involving the relative growth rate (see **Modeling developmental processes with optimal transport** for a precise statement of the optimization problem).

The transport map $\hat{\pi}_{t_1,t_2}$ connecting cells from time t_1 to cells from time t_2 has a row for each cell x at time t_1 and a column for each cell y at time t_2. Each row specifies the *descendant distribution* of a single cell x from time t_1. The descendant mass is the sum of all the entries across a row. This row-sum is proportional to the number of descendants that x will contribute to the next time point. Intuitively, the descendant distribution specifies which cells at time t_2 are likely to be descendants of x (see section 4.1 of **Modeling developmental processes with optimal transport** for the formal definition of descendants in a developmental process).

Similarly, each column specifies the ancestor distribution of a cell y from time t_2. The ancestor mass is usually the same for each cell y. The ancestor distribution tells us which cells at time t_1 are likely to give rise to the cell y.

To compute these transport matrices, we need to specify a cost function, numerical values for the regularization parameters, and (optionally) an initial estimate for the relative growth rate.

2.1. Cost function

To compute the cost of transporting each individual point x from time t_1 to position y at time t_2, we first perform principal components analysis (PCA) on the data from this pair of time points. This dimensionality reduction is performed separately for each pair of adjacent time points. We define the cost function to be squared Euclidean distance in this 'local-PCA space'.

Finally, we normalize the cost matrix by dividing each entry by the median cost for that time interval. Here the cost matrix is the matrix with entries $C_{i,j} = c(x_i, y_j)$ for each x_i form time t_1 and y_j at time t_2. This rescaling of the cost allows us to refer to specific numerical values of the regularization parameters, without worrying about the global scale of distances.

2.2. Regularization parameters

The optimization problem (4) involves three regularization parameters:

- The *entropy* parameter ϵ controls the entropy of the transport map. An extremely large entropy parameter will give a maximally entropic transport map, and an extremely small entropy parameter will give a nearly deterministic transport map. The default value is 0.05.
- λ_1 controls the degree to which transport is unbalanced along the rows. Large values of λ_1 impose stringent constraints related to relative growth rates. Small values of λ_1 give the algorithm more flexibility to change the relative growth rates in order to improve the transport objective. The default value is 1. To visually inspect the degree of unbalancedness, we recommend plotting the input row-sums vs the output row-sums of the transport map **(Figure S1D-F)**.
- λ_2 controls the degree to which transport is unbalanced along the columns. The default value is $\lambda_2 = 50$. This large value essentially imposes equality constraints for the column marginals. A smaller value of λ_2 would allow different amounts of mass to transport to some cells at time t_2. We strongly recommend keeping a large value for λ_2 so that the results are balanced along the columns. To visually inspect the degree of unbalancedness, one can plot the input column-sums vs the output column-sums of the transport map.

As we demonstrate in **QUANTIFICATION AND STATISTICAL ANALYSIS**, our validation results are stable over a wide range of values for ϵ and λ_1.

2.3. Estimating relative growth rates

Our method solves the optimization problem (4) several times, using the output row-sums of the optimal transport map $\hat{\pi}_{t_1,t_2}$ as a new estimate for the relative growth rate function $\hat{g}(x)$. By default, we initialize with

$$\hat{g}(x) = 1,$$

so that all cells grow at the same rate. If one has some prior knowledge of growth rates (e.g. based on gene signatures of proliferation and apoptosis), this can be incorporated in the initial estimate for $\hat{g}(x)$. For our reprogramming data, we show how we formed an initial estimate for relative growth rates in **Estimating growth and death rates and computing transport maps**.

3. Ancestors, descendants, and trajectories

Given a set of cells C, we can compute the descendant distribution of the entire set by adding the descendant distributions of each cell in the set. This can be computed efficiently via matrix multiplication as follows: Let S_1 denote all the cells from time point t_1, and let

$$p(x) = \begin{cases} 1 & x \in C \\ 0 & \text{otherwise} \end{cases}$$

denote the uniform distribution on $C \subset S$. The descendant distribution of C is given by $\hat{\pi}_{t_1,t_2}p$. We compute ancestor distributions in a similar way, except instead of taking the sum we compute an average. In particular, we define a function $p(x)$ as above, then normalize it to sum to 1 and then form the matrix-vector product

$$p^T \hat{\pi}_{t_0,t_1}$$

to obtain the ancestor distribution on time t_0.

After computing the trajectory to or from a cell set C (in the form of a sequence of ancestor and descendant distributions), we compute trends in expression for any gene or gene signature of interest along the trajectory. For each time point, we compute the mean expression weighting each cell according to the probability distribution defined by the ancestor or descendant distribution.

4. Learning gene regulatory models

We employ two strategies to summarize the transport maps by learning models of gene regulation. The first model uses local enrichment analysis to identify transcription factors (TFs) enriched in ancestors of a set of cells. The second model is motivated by the dynamical systems formulation of optimal transport, as described above in Section I.4.3.

4.1. Local model: TF enrichment analysis of top ancestors

We perform local enrichment analysis as follows. Given a set of cells C at time t_2, we first compute the ancestor distribution of C at an earlier time t_1, as described in Section II.3 above. We then select cells contributing the most mass to the ancestor distribution, until a certain amount of mass is accounted for (e.g. 30% of the ancestor mass). We refer to these as the *top ancestors* at time t_1 of the cell set C. Finally, we compare the top ancestors to a null set of cells from the same time point. For example, this null cell set could be:

- all cells except for the top ancestors,
- the *bottom ancestors* (defined to be all cells except for the top ancestors of a less-strict cut-off),
- the bottom ancestors restricted to a specialized subset (e.g. all other trophoblasts when C is a specific subset of trophoblasts like spongiotrophoblasts).

4.2. Global model: learning a cell-autonomous gradient flow

To learn a simple description of the temporal flow, we assume that a cell's trajectory is cell-autonomous and, in fact, depends only on its own internal gene expression. We know this is wrong as it ignores paracrine signaling between cells, and we discuss models that include cell-cell communication below. However, this assumption is powerful because it exposes the time-dependence of the stochastic process $\mathbb{P}_t$ as arising from pushing an initial measure through a differential equation:

$$\dot{x} = f(x). \tag{10}$$

Here f is a vector field that prescribes the flow of a particle x. Our biological motivation for estimating such a function f is that it encodes information about the cell-autonomous regulatory networks that create the equations of motion in gene-expression space.

We propose to set up a regression to learn a regulatory function f that models the fate of a cell at time t_{i+1} as a function of its expression profile at time t_i. Our approach involves sampling pairs of points using the couplings from optimal transport:

- For each pair of time points t_i, t_{i+1}, we sample pairs of cells $\left(X_{t_i}, X_{t_{i+1}}\right)$ from the joint distribution specified by the transport map $\hat{\pi}_{t_i,t_{i+1}}$.
- Using the training data generated in the first step, we set up the following regression:

$$\min_{f \in \mathcal{F}} \quad \mathbb{E}_{\hat{\pi}_{t_i,t_{i+1}}} \left\| X_{t_{i+1}} - f(X_{t_i}) \right\|^2,$$

where $\mathcal{F}$ is a rectified-linear function class defined in terms of a specific generalized logistic function $\ell : \mathbb{R} \mapsto \mathbb{R}$:

$$\ell(x; k, b, y_0, x_0) = \frac{k y_0}{y_0 + (k - y_0) e^{-b(x - x_0)}},$$

where $k, b, y_0, x_0 \in \mathbb{R}$ are parameters of the generalized logistic function $\ell(x)$.

We define a function class $\mathcal{F}$ consisting of functions $f : \mathbb{R}^G \to \mathbb{R}^G$ of the form

$$f(x) = U\ell(WTx),$$

where ℓ is applied entry-wise to the vector $WTx \in \mathbb{R}^M$ to obtain a vector that we multiply against $U \in \mathbb{R}^{G \times M}$. Here $T \in \mathbb{R}^{G_{\text{TF}} \times G}$ denotes a projection operator that selects only the coordinates of x that are transcription factors, and G_{TF} is the number of transcription factors. Intuitively, this gives a set of low-rank, linear functions with sparse factors. Each rank-1 component can be interpreted as a regulatory module of transcription factors acting on a module of regulated genes.

We set up the following optimization over matrices $U \in \mathbb{R}^{G \times M}$ and $W \in \mathbb{R}^{M \times G_{\text{TF}}}$:

$$\begin{aligned} \min_{U,W} \quad & \mathbb{E}_r \left\| X_{t_{i+1}} - U\ell(WTX_{t_i}) \right\|^2 + \eta_1 \|U\|_1 + \eta_2 \|W\|_1, + \eta_3 \|W\|_2^2 \\ \text{s.t.} \quad & U \geq 0. \end{aligned} \tag{11}$$

where $(X_{t_i}, X_{t_{i+1}})$ is a pair of random variables distributed according to the normalized transport map r, and $\|U\|_1$ denotes the sparsity-promoting ℓ_1 norm of U, viewed as a vector (that is, the sum of the absolute value of the entries of U). Each rank one component (row of U or column of W) gives us a group of genes controlled by a set of transcription factors. The regularization parameters η_1 and η_2 control the sparsity level (i.e. number of genes in these groups).

Implementation: We designed a stochastic gradient descent algorithm to solve (11). Over a sequence of epochs, the algorithm samples batches of points $(X_{t_i}, X_{t_{i+1}})$ from the transport maps, computes the gradient of the loss, and updates the optimization variables U and W. The batch sizes are determined by the Shannon diversity of the transport maps: for each pair of consecutive time points, we compute the Shannon diversity S of the transport map, then randomly sample $\max(S \times 10^{-5}, 10)$ pairs of points to add to the batch. We run for a total of $10,000$ epochs.

Cell non-autonomous processes: The gradient flow (10) addresses cell-autonomous processes. Otherwise, the rate of change in expression $\dot{x}$ is not just a function of a cell's own expression vector $x(t)$, but also of other expression vectors from other cells. We can accommodate cell non-autonomous processes by allowing f to also depend on the full distribution $\mathbb{P}_t$:

$$\frac{dx}{dt} = f(x, \mathbb{P}_t). \tag{12}$$

Concretely, we could allow f to depend on the mean expression levels of specific genes (expressed by any cell) encoding, for example, secreted factors or direct protein measurements of the factors themselves. For a theoretical description of gradient flows with interactions, see Section 4.3 of **Modeling developmental processes with optimal transport**.

5. Geodesic interpolation for validation

Optimal transport provides an elegant way to interpolate distribution-valued data, analogous to how linear regression can be used to interpolate numerical or vector-valued data. Given two numerical data-points, the simplest way to interpolate is to connect them with a line; this is the shortest path connecting the observed data. Given two distributions, we interpolate by finding the shortest path in the space of distributions. To do this we need a notion of distance between distributions, and for this we use the metric induced by optimal transport. This metric space is called Wasserstein space, and this form of interpolation is called geodesic interpolation (Villani, 2008).

We derive a modified version of geodesic interpolation that takes into account cell growth. Ordinarily, an interpolating distribution is computed by first computing a transport map between the distributions, and then connecting each point in the first distribution to points in the second according to the transport map. Finally, an interpolating point cloud is produced by from the midpoints of those line segments. (More generally, instead of taking just midpoints, one one can also construct a family of interpolations that sweep from the first distribution to the second). We extend this framework to accommodate growth by changing the mass of the point we place at the midpoint (to account for the fact that cells will have a different number of descendants at time t_1 than they will at time t_2).

Specifically, to interpolate at time $s \in (t_1, t_2)$, we first renormalize the rows of the transport map so they sum to roughly $\frac{\hat{g}(x)^{s-t_1}}{\int \hat{g}(x)^{s-t_1} d\hat{\mathbb{P}}_{t_1}}$ instead of $\frac{\hat{g}(x)^{t_2-t_1}}{\int \hat{g}(x)^{t_2-t_1} d\hat{\mathbb{P}}_{t_1}(x)}$. This takes into account the descendant mass each cell will have by time s instead of by time t_2. We then sample points $z_1, \ldots, z_N$ as follows:

1. Sample a pair of points (x, y) from the joint distribution specified by the transport map.
2. Identify the point
$$z = \alpha x + (1 - \alpha) y$$
along the line segment connecting x and y. Here α is given by $s = \alpha t_1 + (1 - \alpha) t_2$.

By repeating the steps above, we accumulate a point-cloud of points $z_1, \ldots, z_N$. Finally, we define the interpolating distribution as
$$\hat{\mathbb{P}}(s) = \frac{1}{N} \sum_{i=1}^{N} \delta_{z_i}.$$

Equipped with this notion of interpolation, we can test the performance of optimal transport by comparing the interpolated distribution to held-out time points. Using the data from time t_i and t_{i+2}, we interpolate to estimate the distribution $\mathbb{P}_{t_{i+1}}$. We then compute the Wasserstein distance between the interpolated distribution and the observed distribution. We compare this distance to a null model generated from the independent coupling where we sample pairs (x, y) independently $x \sim \hat{\mathbb{P}}_{t_i}$ and $y \sim \hat{\mathbb{P}}_{t_{i+2}}$ in step 1 above. We also compare the interpolated distance to distance between batches of $\mathbb{P}_{t_{i+1}}$. Optimal transport is performing well if the interpolated point cloud is as close to the batches of the held out time point as the batches are to each other, and the null-interpolated point cloud is farther away.

We present our application for validation in the case of IPS reprogramming in **Validation by geodesic interpolation**.

III. Experimental methods

1. Derivation of secondary MEFs

OKSM secondary Mouse embryonic fibroblasts (MEFs) were derived from E13.5 female embryos with a mixed B6;129 background. The cell line used in this study was homozygous for ROSA26-M2rtTA, homozygous for a polycistronic cassette carrying *Oct4*, *Klf4*, *Sox2*, and *Myc* at the *Col1a1* locus and homozygous for an EGFP reporter under the control of the *Oct4* promoter (Stadtfeld et al., 2010). Briefly, MEFs were isolated from E13.5 embryos from timed-matings by removing the head, limbs, and internal organs under a dissecting microscope. The remaining tissue was finely minced using scalpels and dissociated by incubation at 37°C for 10 minutes in trypsin-EDTA (Thermo Fisher Scientific). Dissociated cells were then plated in MEF medium containing DMEM (Thermo Fisher Scientific), supplemented with 10% fetal bovine serum (GE Healthcare Life Sciences), non-essential amino acids (Thermo Fisher Scientific), and GlutaMAX (Thermo Fisher Scientific). MEFs were cultured at 37°C and 4% CO_2 and passaged until confluent. All procedures, including maintenance of animals, were performed according to a mouse protocol (2006N000104) approved by the MGH Subcommittee on Research Animal Care.

2. Derivation of Primary MEFs

Primary MEFs were derived from E13.5 embryos with a B6.Cg-*Gt(ROSA)26Sor*$^{tm1(rtTA*M2)Jae}$/J x B6;129S4-*Pou5f1*^{tm2Jae}/J background. The cell line was homozygous for ROSA26-M2rtTA, and homozygous for an EGFP reporter under the control of the *Oct4* promoter. MEFs were isolated as mentioned above.

3. Reprogramming assay

For the reprogramming assay, 20,000 low passage MEFs (no greater than 3-4 passages from isolation) were seeded in a 6-well plate. These cells were cultured at 37°C and 5% CO_2 in reprogramming medium containing KnockOut DMEM (GIBCO), 10% knockout serum replacement (KSR, GIBCO), 10% fetal bovine serum (FBS, GIBCO), 1% GlutaMAX (Invitrogen), 1% nonessential amino acids (NEAA, Invitrogen), 0.055 mM 2-mercaptoethanol (Sigma), 1% penicillin-streptomycin (Invitrogen) and 1,000 U/ml leukemia inhibitory factor (LIF, Millipore). Day 0 medium was supplemented with 2 μg/mL doxycycline Phase-1(Dox) to induce the polycistronic OKSM expression cassette. Medium was refreshed every other day. At day 8, doxycycline was withdrawn, and cells were transferred to either serum-free 2i medium containing 3 μM CHIR99021, 1 μM PD0325901, and LIF (Phase-2(2i)) (Ying et al., 2008) or maintained in reprogramming medium (Phase-2(serum)). Fresh medium was added every other day until the final time point on day 18. Oct4-EGFP positive iPSC colonies should start to appear on day 10, indicative of successful reprogramming of the endogenous Oct4 locus.

4. Sample collection

We profiled a total of 315,000 cells from two time-course experiments across 18 days in two different culture conditions: in the first we profiled 65,781 cells collected over 10 time points separated by ~48 hours; in the second we profiled 259,155 cells collected over 39 time points separated by ~12 hours across an 18-day time course (and every 6 hours between days 8 and 9). In the larger experiment, duplicate samples were collected at each time point. Cells were also collected from established iPSCs cell lines reprogrammed from the same MEFs, maintained either in Phase-2(2i) conditions or in Phase-2(serum) medium. For all time points, selected wells were trypsinized for 5 mins followed by inactivation of trypsin by addition of MEF medium. Cells were subsequently spun down and washed with 1X PBS supplemented with 0.1% bovine serum albumin. The cells were then passed through a 40 micron filter to remove cell debris and large clumps. Cell count was determined using Neubauer chamber hemocytometer to a final concentration of 1000 cells/μ1.

5. Single-cell RNA-seq

ScRNA-seq libraries were generated from each time point using the 10X Genomics Chromium Controller Instrument (10X Genomics, Pleasanton, CA) and Chromium™ Single Cell 3' Reagent Kits v1 (65,781 cells experiment) and v2 (259,155 cells experiment) according to manufacturer's instructions. Reverse transcription and sample indexing were performed using the C1000 Touch Thermal cycler with 96-Deep Well Reaction Module. Briefly, the suspended cells were loaded on a Chromium controller Single-Cell Instrument to first generate single-cell Gel Bead-In-Emulsions (GEMs). After breaking the GEMs, the barcoded cDNA was then purified and amplified. The amplified barcoded cDNA was fragmented, A-tailed and ligated with adaptors. Finally, PCR amplification was performed to enable sample indexing and enrichment of the 3' RNA-Seq libraries. The final libraries were quantified using Thermo Fisher Qubit dsDNA HS Assay kit (Q32851) and the fragment size distribution of the libraries were determined using the Agilent 2100 BioAnalyzer High Sensitivity DNA kit (5067-4626). Pooled libraries were then sequenced using Illumina Sequencing. All samples were sequenced to an average depth of 87 million paired-end reads per sample (see Experimental Methods), with 98 bp on the first read and 10 bp on the second read. In the larger experiment, we profiled 259,155 cells to an average depth of 46,523 reads per cell.

6. Lentivirus vector construction and particle production

To test whether transcription factors (TFs) improve late-stage reprogramming efficiency, we generated lentiviral constructs for the top candidates *Zfp42*, and *Obox6*. cDNAs for these factors were ordered from Origene (*Zfp42*-MG203929, and *Obox6*-MR215428) and cloned into the FUW Tet-On vector (Addgene, Plasmid #20323) using the Gibson Assembly (NEB, E2611S). Briefly, the cDNA for each TF was amplified and cloned into the backbone generated by removing *Oct4* from the FUW-Teto-*Oct4* vector. All vectors were verified by Sanger sequencing analysis. For lentivirus production, HEK293T cells were plated at a density of $2.6x10^6$ cells/well in a 10cm dish. The cells were transfected with the lentiviral packaging vector and a TF-expressing vector at 70-80% growth confluency using the Fugene HD reagent (Promega E2311), according to the

manufacturer's protocols. At 48 hours after transfection, the viral supernatant was collected, filtered and stored at -80°C for future use.

7. Paracrine signaling assay

To determine the effect of GDF9 on reprogramming, we plated secondary MEFs at a concentration of 5,000 cells per well of a 24-well plate and added either recombinant mouse GDF9 (R&D Systems, 739-G9-010, lot SOZ0516121) daily from day 8 onward, or control (0.1% Bovine Serum Albumin in 4 mM HCl, R&D Systems, RB04). We initially tested different doses (0, 0.1 μg/ml, 0.5 μg/ml, and 1 μg/ml) and then confirmed results seen at the highest dose in multiple independent experiments. We used three distinct approaches to determine the proportion of pluripotent cell at day 15: (i) counting the number of Oct4-EGFP^{+} colonies using a fluorescence microscope, (ii) bulk RNAseq (Quantseq, Lexogen) and (iii) scRNAseq (as above). For each assay, experiments were performed in biological triplicates (each assay using separate replicates).

8. Reprogramming efficiency of secondary MEFs together with individual TFs

We sought to determine the ability of the candidate TFs to augment reprogramming efficiency in secondary MEFs; the use of secondary MEFs for reprogramming overcomes limitations associated with random lentiviral integration events at variable genomic locations. Briefly, secondary MEFs were plated at a concentration of 20,000 cells per well of a 6-well plate. Cells were infected with virus containing ZFP42, OBOX6, or an empty vector and maintained in reprogramming medium as described above. At day 8 after induction, cells were switched to either Phase-2(2i) or Phase-2(serum). On day 16, reprogramming efficiency was quantified by measuring the levels of the EGFP reporter driven by the endogenous *Oct4* promoter. FACS analyses was performed using the Beckman Coulter CytoFLEX S, and the percentage of Oct4-EGFP^{+} cells was determined. Triplicates were used to determine average and standard deviation.

9. Reprogramming efficiency of primary MEFs with individual TFs and OKSM

We also independently tested the performance of TFs in primary MEFs. To this end, lentiviral particles were generated from four distinct FUW-Teto vectors, containing OCT4, SOX2, KLF4, and MYC, previously developed in the Jaenisch lab. MEFs from the background strain B6.Cg-*Gt(ROSA)26Sor*$^{tm1(rtTA*M2)Jae}$/J x B6;129S4-*Pou5f1*^{tm2Jae}/J were infected with these lentiviral particles, together with a lentivirus expressing tetracycline-inducible ZFP42, OBOX6 or no insert. Infected cells were then induced with 2 μg/mL doxycycline in ESC reprogramming medium (day 0). At day 8 after induction, cells were switched to either Phase-2(2i) or Phase-2(serum). On day 16, the number of Oct4-EGFP^{+} colonies were counted using a fluorescence microscope. Triplicates for each condition used to determine average values and standard deviation.

IV. Preparation of expression matrices

To compute an expression matrix from scRNA-seq data, we aligned sequenced reads to obtain a matrix U of UMI counts, with a row for each gene and a column for each cell. To reduce variation due to fluctuations in the total number of transcripts per cell, we divide the UMI vector for each cell by the total number of transcripts in that cell. Thus, we define the expression matrix E in terms of the UMI matrix U via:

$$E = \frac{U_{ij}}{\sum_{i=1}^{G} U_{ij}} \times 10^4.$$

In our subsequent analysis, we make use of two variance-stabilizing transforms of the expression matrix E. In particular, we define

1. $\tilde{E}$ to be the log-normalized expression matrix. The entries of $\tilde{E}$ are obtained via
$$\tilde{E} = log(E_{ij} + 1)$$
2. $\bar{E}$ to be the truncated expression matrix. The entries of $\bar{E}$ are obtained by capping the entries of $\bar{E}$ at the 99.5% quantile.

When we refer to an expression profile, by default we refer to a column of $\tilde{E}$ unless otherwise specified.

1. Read alignment

The 98 bp reads were aligned to the UCSC mm10 transcriptome, and a matrix of UMI counts was obtained using Cellranger from the 10X Genomics pipeline (v2.0.0) with default parameters (https://support.10xgenomics.com/single-cell-gene-expression/software/pipelines/latest/installation). Quality control metrics about barcoding and sequencing such as the estimated number of cells per collection and the median number of genes detected across cells are summarized in Table S1. To estimate expression of exogenous OKSM factors from OKSM cassette, we extracted RBGpA sequence (839 bp) from the OKSM cassette FASTA file, and generated a reference using the mkref function from the Cellranger pipeline.

2. Downsampling and filtering expression matrix

The expression matrix was downsampled to 15,000 UMIs per cell. Cells with less than 2000 UMIs per cell in total and all genes that were expressed in less than 50 cells were discarded, leaving 251,203 cells and G= 19,089 genes for further analysis. The elements of expression matrix were normalized by dividing UMI count by the total UMI counts per cell and multiplied by 10,000 i.e. expression level is reported as transcripts per 10,000 counts.

3. Selecting variable genes

We used the function MeanVarPlot from the Seurat package (v2.1.0) (Satija et al., 2015) to select 1,479 variable genes. First, we divided genes into 20 bins based on their average expression levels across all cells. Second, we compute Fano factor of gene expression in each bin and then z-scored. The Fano factor, defined as the variance divided by the mean, is a measure of dispersion. Finally, by thresholding the z-scored dispersion at 1.0, we obtained a set of 1479 variable genes. After

selecting variable genes, we created a variable gene expression matrix by renormalizing as described above.

V. Visualization: force-directed layout embedding

In this section we introduce our two dimensional visualization technique based on force-directed layout embedding (FLE) (Jacomy et al., 2014). FLE is large-scale graph visualization tool which simulates the evolution of a physical system in which connected nodes experience attractive forces, but unconnected nodes experience repulsive forces. It better captures global structures than tSNE. Initial FLE algorithms used simple electrostatic and spring forces, but modern FLE algorithms allow for more elaborate interactions that can depend on the degree of nodes or include gravity terms that attract all nodes to the center (this is especially important for disconnected graphs, which would otherwise fly apart). Starting from a random initial position of vertices, the network of nodes evolves in such a manner that at any iteration a new position of vertices is computed from the net forces acting on them.

We apply FLE to visualize the nearest neighbor graph generated from our data.

Implementation: Our visualization takes as input the expression matrix of highly-variable genes, selected as described in "Secion IV. Preparation of expression matrices". First, we reduce to 100 dimensions by computing a 100 dimensional diffusion component embedding of the dataset using SCANPY (v0.2.8) with default parameters. Second, for each cell we compute its 20 nearest neighbors in 100-dimensional diffusion component space to produce a nearest neighbor graph. For this step, we used the approximate k-NN algorithm Annoy from the R package RCPPANNOY (v0.0.10). Finally, we compute the force-directed layout on the k-NN graph using the ForceAtlas2 algorithm (Jacomy et al., 2014) from the Gephi Toolkit (v0.9.2).

VI. Creating gene signatures and cell sets

1. Gene signatures

We then constructed curated gene signatures from various databases of gene signatures. Given a set of genes, we score cells based on their gene expression. In particular, for a given cell we compute the z-score for each gene in the set. We then truncate these z-scores at 5 or −5, and define the signature of the cell to be the mean z-score over all genes in the gene set.

The table below summarizes the sources from which we obtained signatures. In two cases (neural identity and epithelial identity) we constructed signatures manually using marker genes. A pluripotency gene signature was determined in this work using the pilot dataset. We performed differential gene expression analysis between two groups of cells: mature iPSCs and cells along the time course D0 to D16 and took the top 100 genes with increased expression in mature iPSCs. A proliferation gene signature was obtained by combining genes expressed at G1/S and G2/M phases.

In several places, we also compute gene signatures based on co-expression with a given gene of interest. For instance, in the stromal region we noticed several genes (*Cxcl12*, *Ifitm1*, and *Matn4*) with expression patterns that were distinct from a signature of long-term cultured MEFs (**Figure S2B**). For each gene, we computed a co-expression signature by finding the set of genes with expression levels in stromal cells that were >15% correlated with the gene of interest. We found that these gene signatures were significantly overlapping (p-value < 0.01, hypergeometric test) with signatures of stromal cells in neonatal muscle and neonatal skin in the Mouse Cell Atlas. Similarly, in the neural region we derived signatures of genes co-expressed with *Gad1* and with *Slc17a6* (**Figure S4D**). These signatures significantly overlapped signatures of inhibitory and excitatory neurons, respectively, derived from the Allen Brain Atlas.

Gene Signature	**Source**
MEF identity	(Chen et al., 2013; Han et al., 2018; Lattin et al., 2008)
Pluripotency	This work.
Proliferation	(Tirosh et al., 2016)
ER stress	GO:0034976, Biological Process Ontology
Epithelial identity	This work. Marker genes: (Li et al., 2010; Takaishi et al., 2016; Whiteman et al., 2014)
ECM rearrangement	GO:0030198, Biological Process Ontology
Apoptosis	Hallmark P53 Pathway, MSigDB
Senescence	(Coppé et al., 2010)
Neural identity	This work. Marker gene sources: (Fonseca et al., 2013; Gouti et al., 2011; Kan et al., 2004; Lazarov et al., 2010; Sakakibara et al., 2001; Sansom et al., 2009; Watanabe et al., 2017)
Trophoblast	(Han et al., 2018)
X reactivation	chromosome X
XEN	(Lin et al., 2016)
Trophoblast progenitors	(Han et al., 2018)
Spiral Artery Trophpblast Giant Cells	(Han et al., 2018)
Oligodendrocyte precursor cells (OPC)	(Tasic et al., 2016)
Astrocytes	(Tasic et al., 2016)
Cortical Neurons	(Tasic et al., 2016)
RadialGlia-Id3	(Han et al., 2018)
RadialGlia-Gdf10	(Han et al., 2018)

RadialGlia-Neurog2	(Han et al., 2018)
Long-term MEFs	(Han et al., 2018)
Embryonic mesenchyme	(Han et al., 2018)
Cxcl12 co-expressed	This work.
Ifitm1 co-expressed	This work.
Matn4 co-expressed	This work.
2C	(Han et al., 2018)

2. Cell sets

Using the gene signatures described above, we created coarse cell sets defining the broad regions of the landscape (iPSC, Trophoblast, Neural, Stromal, Epithelial, and MET), and cell subtype sets defining different cell types within a region (stromal, trophoblast, and neural subtypes, along with 2-cell stage).

To define the coarse cell sets, we first computed a rough partitioning of the landscape by clustering cells using the Louvain method of spectral clustering to obtain 65 cell clusters using k=5 nearest neighbors (**Figure S5B**). By examining signature score activity levels over clusters, we grouped several clusters to form cell sets for the iPSC, Stromal and Neuronal regions. Because our densely sampled data does not always segregate into distinct clusters, we defined some additional coarse cell sets by signature scores. We define the trophoblast cell set to include all cells with Trophoblast signature greater than 0.7. We defined the epithelial cell set to include all cells with epithelial identity signature greater than 0.8, minus all cells included in other cell sets (mostly removing the trophoblasts with epithelial signature). Finally, we defined the MET Region as the ancestors of iPS, Trophoblast, Neural and Epithelial cells. In particular, we computed the top ancestors of each major cell set, then merged these cell sets and removed the cells *in* each major cell set.

Within the Stromal, Trophoblast, Neural and iPSC cell sets, we then conducted more sensitive statistical tests for cell subtype signatures. We did this by calculating empirical p-values for the subtype signature score for each (region-specific) subtype in each cell. In each of 100,000 permutation trials, we randomly and independently shuffled the expression levels of each gene across the cells within a region. In each cell, we then computed signature scores in the permuted data, and generated p-values by determining the frequency at which the permuted score was greater than the original score. While the results shown in figures and discussed in the main text are based on shuffling genes across cells, we similarly permuted the expression levels within each cell, and found consistent results. Finally, we controlled for multiple hypothesis testing by calculating FDR q-values, and used a threshold FDR of 10% to define cell subtype sets.

VII. Estimating growth and death rates and computing transport maps

1. Initial estimate of growth rates

We form an initial estimate of the relative growth rate as the expectation of a birth-death process on gene expression space with birth-rate β(x) and death rate δ(x) defined in terms of expression levels of genes involved in cell proliferation and apoptosis. Multi-state birth-death processes have been used before to model growth, death, and transitions in iPS reprogramming (Liu et al., 2016). A birth-death process is a classical model for how the number of individuals in a population can vary over time. The model is specified in terms of a birth rate β and death rate δ: During a time interval Δt, the probability of a birth is βΔt and the probability of a death is δΔt. The doubling time for a birth death process is defined as follows. Starting with N(0) = n, the time τ it would take to get to an expected population size of $\mathbb{E}N(t) = 2n$ is

$$\tau = \frac{\ln 2}{\beta - \delta}$$

The half-life can be computed in a similar way. We apply a sigmoid function to transform the proliferation score into a birth rate. The sigmoid function smoothly interpolates between maximal and minimal birth rates. We specify the maximal birth rate to be $\beta_{MAX} = 1.7$. Therefore the fastest cell doubling time is

$$\frac{\ln 2}{1.7} \approx 0.41\ days \approx 9.6\ hours,$$

by the doubling time equation above. We define the minimal birth rate as $\beta_{MIN} = 0.3$. Therefore the slowest cell doubling time is

$$\frac{\ln 2}{0.3} = 2.3\ days = 55\ hours.$$

Similarly, we transform the apoptosis signature into an estimate of cellular death rates by applying a sigmoid function to smoothly interpolate between minimal and maximal allowed death rates. We define the minimal death rate parameter to be $\delta_{MIN} = 0.3$, and the maximal death rate parameter as $\delta_{MAX} = 1.7$. By the calculations above, these correspond to half-lives of 55 and 9.6 hours respectively.

2. Learning growth rates and computing transport maps

Using the growth rates defined in the previous section as an initial estimate, we compute transport maps and automatically improve these growth rates using the Waddington-OT software package (see Section *Computing transport maps*). For the cost function, we use squared Euclidean distance in 30 dimensional local PCA space computed on the variable gene data from the relevant pair of time points. We use the following parameter settings:
$\epsilon = 0.05, \lambda_1 = 1, \lambda_2 = 50$, growth_iters = 3.
The parameters λ_1 and λ_2 control the degree to which the row-sums and column-sums are unbalanced. A larger value of λ_1 induces a greater correlation between the input and output growth rates. The Waddington-OT package iterates the procedure of computing transport maps based on

input growth rates, and then using the output growth rates as new input growth rates to recompute transport maps. We ran this for growth_iters = 3 total iterations.

This gives us a set of transport maps between each pair of time points, which can be used to estimate the temporal coupling. From this estimate of the temporal coupling, we compute ancestor and descendant distributions to each of the major cell sets defined in the previous section.

VIII. Regulatory analysis

We performed regulatory analysis to identify modules of transcription factors regulating modules of genes with our global regulatory model from the Waddington-OT software package, described in Section *Learning gene regulatory models*. The optimization begins by specifying the number of gene modules, and establishing an initial estimate for each. We used spectral clustering to initialize the modules: genes were clustered into 50 sets, with one module corresponding to each set, and weights set to 0 for genes outside the set, and 1 for genes within the set.

We then specify a time lag between TF and gene module expression. In order to test for potential regulatory interactions on different time scales, we computed global regulatory models with three time lags: 6hrs, 48hrs, and 96hrs. This allowed us to identify factors that are predictive several days in advance -- for instance, Nanog is a very early predictor of pluripotency and was found to be associated with a pluripotency associated gene expression module in the 96 hour model -- as well as those predictive on shorter time scales -- for instance, we TFs that are predictive of neural-associated expression modules in the 6 and 48 hour models, but do not find such predictive TFs in the 96 hour model.

Finally, we set regularization and stochastic block size parameters. Default values available in the code online were used in this study. Briefly, regularization parameters were tuned on small training datasets to enforce sparsity (l1 penalties) and reduce model complexity (l2 penalty) while still achieving a good fit (>60% correlation between predicted and observed expression) in training data. These parameters may have to be specifically tuned in new datasets. The stochastic block size and number of epochs were set according to available hardware resources.

IX. Validation by geodesic interpolation

We validate Waddington-OT by demonstrating that we can accurately interpolate the distribution of cells at held out time points. We applied geodesic interpolation (described in **Waddington-OT: Concepts and Implementation**) to our reprogramming data to predict the distribution of cells at each time point, using only the data from the previous and next time points. In other words, we sought to predict the distribution $\mathbb{P}_{t_2}$ at time t_2 from the distributions at neighboring time points: $\mathbb{P}_{t_1}$ and $\mathbb{P}_{t_3}$ (**Figure 2J, S1D-F**). To determine a baseline for performance, we examined the distance between the two different batches of the held-out distribution.

To compute the optimal transport coupling from $\mathbb{P}_{t_1}$ to $\mathbb{P}_{t_3}$, we used the Waddington-OT package with default parameters. For the cost function we compute 30 dimensional local PCA coordinates using only the points from time $t_1$and t_3. We then embedded the data from time t_2 into the 30

dimensional local PCA space which was computed using only the data from time t_1 and t_3. Finally, we use Wasserstein-2 distance to compute distance between point clouds.

We compare the performance of OT to four null models:

- Null 1 and Null 2: a point cloud is constructed by interpolating with the independent coupling. Null 1 uses growth in the interpolation. Null 2 does not use growth.
- Null 3 and Null 4: the observed distributions from earlier (Null 3) or later (Null 4) time points are used as the interpolating point cloud.

To estimate the standard deviation of the quality of interpolation, we interpolate using different batches of $\mathbb{P}_{t_1}$ and $\mathbb{P}_{t_3}$.

We investigated the time-scale over which optimal transport accurately recovers temporal couplings by interpolating over longer intervals. With 2-day intervals (**Figure S1D**) we see some performance degradation compared to 1-day intervals (**Figure 2J**).

X. Paracrine signaling

1. Predicting ligand-receptor interaction pairs

To characterize potential cell-cell interactions between contemporaneous cells during reprogramming, we first collected a list of ligands and receptors found in the GO database. The set of ligands (415 genes) is a union of three gene sets from the following GO terms:

1) *cytokine activity* (GO:0005125),
2) *growth factor activity* (GO:0008083), and
3) *hormone activity* (GO:0005179).

The set of receptors (2335 genes) is defined by the GO term *receptor activity* (GO:0004872). Next, we used a curated database of mouse protein-protein interactions (Mertins et al., 2017) and identified 580 potential ligand-receptor pairs.

First, we defined an interaction score $I_{A;B;X;Y;t}$ as the product of (1) the fraction of cells ($F_{A;X;t}$) in cell-set A expressing ligand X at time t and (2) the fraction of cells ($F_{B;Y;t}$) in cell-set B expressing the cognate receptor Y at time t. We define the aggregate interaction score $I_{A;B;t}$ as a sum of the individual interaction scores across all pairs:

$$I_{A;B;t} = \sum_{All\ X\text{-}Y\ pairs} I_{A;B;X;Y;t} = \sum_{All\ X\text{-}Y\ pairs} F_{A;X;t}\ F_{B;Y;t}$$

We depicted the aggregate interaction scores for all combinations of cell clusters in **Figure 6B**, **S5A**.

Second, we sought to explore individual ligand-receptor pairs at a given day and condition between cell ancestors of interest. For this purpose we define the interaction score $I_{A;B;X;Y;t}$ as the product of (1) the average expression of the ligand X in ancestors at time t of a cell set A and

(2) the average expression of the cognate receptor Y in ancestors at time t of a cell set B. Values of the interaction scores $I_{A;B;X;Y;t}$ are high for ubiquitously expressed ligands and receptors at a given day and may be nonspecific to a pair of cell ancestors of interest. Thus, we used permutations to generate an empirical null distribution of interaction scores. In each of the 10,000 permutations, we randomly shuffled the labels of cells and calculated the interaction score $I^s_{A;B;X;Y;t}$. We then standardized each ligand-receptor interaction score by taking the distance between the interaction score $I_{A;B;X;Y;t}$ and the mean interaction score in units of standard deviations from the permuted data $((I_{A;B;X;Y;t} - \text{mean}(I^s_{A;B;X;Y;t}))/\text{sd}(I^s_{A;B;X;Y;t}))$.

We depicted examples of standardized interaction scores ranked by their values in **Figure 6C-E** and **S5C-E**. Replacement of the average expression of the ligand with the total expression of the ligand in the calculation of the standardized interaction score does not affect the results.

2. Testing of Gdf9 effect on reprogramming efficiency

To experimentally test the impact of GDF9 on reprogramming efficiency, we added GDF9 daily (at 0, 0.1, 0.5, and 1 μg/ml) to cells grown under serum conditions, beginning at day 8. Samples on day 15 were assessed for the number of Oct4-GFP positive colonies and collected for bulk RNAseq (Moll et al., 2014) and scRNAseq (10X genomics), in three biological replicates.

Bulk RNAseq data were analyzed as follows: reads (83 bp) were aligned to the UCSC mm10 transcriptome, and a matrix of read counts was obtained using the QuantSeq processing pipeline (http://rpubs.com/chapmandu2/171024) with the reference genome sequence and gene annotations (GTF file) from the Cellranger 10X Genomics pipeline (v2.0.0) (https://support.10xgenomics.com/single-cell-gene-expression/software/pipelines/latest/installation). Bulk RNAseq data were used to compute the ratio of iPSC signature scores to the sum of signature scores of other major cell types (iPSC, trophoblast, neural, epithelial and stromal) in each sample (**Figure 7E**).

Single-cell RNAseq data were analyzed as follows: reads were aligned and processed as described in "Section IV: Preparation of expression matrices" and cells in which fewer than 1,000 genes were detected were filtered out, yielding 47,540 cells for further analysis. We assigned cells to the major cell sets (iPSC, trophoblast, neural, epithelial and stromal) by clustering and annotation with gene signature scores. (To remove batch effects, we used tools in Seurat (Butler et al., 2018).) Cell-type proportions are shown in **Figure 7F**, **S6H,I**.

XI. Classification of differential genes along the trajectory to iPSCs

To identify differential genes along the successful trajectory to iPSCs we computed the average expression (TPM) of all 19,089 genes in ancestors of iPSCs. The average expression values were log2 transformed and we filtered out genes for which the difference between maximal and minimal expression value between day 0 and day 18 is less than 1, leaving 2311 genes for further analysis. The genes were classified into 15 groups by k-means clustering as implemented in the R package stats. To identify the number of clusters we applied a gap statistic (Tibshirani et al., 2001) using the function clusGap from R package cluster v2.0.6.

We performed functional enrichment analysis on the identified gene clusters using the findGO.pl program from the HOMER suite (Hypergeometric Optimization of Motif Enrichment, v4.9.1) (Heinz et al., 2010) with Benjamini and Hochberg FDR correction for multiple hypothesis testing (retaining terms at FDR < 0.05). All genes that passed quality-control filters were used as a background set.

XII. Identifying large chromosomal aberrations

We have previously developed methods to identify copy number variations (CNVs) in scRNA-seq data from tumor samples (Patel et al., 2014; Tirosh et al., 2016). That analysis differed from our current study in two key aspects: (1) the data were based on full length scRNA-seq (SMART-Seq2), and sequenced to greater depth in each cell, and (2) there we could rely on the clonal expansion of CNVs to make it easier to identify recurring chromosomal aberrations.

We performed three types of analysis to detect aberrant expression in large chromosomal regions. First, we searched for cells with significant up- or down-regulation at the level of entire chromosomes. Second, we ran a coarse analysis to identify cells with significant net aberrant expression across windows spanning 25 broadly-expressed genes. Focusing on regions that were enriched for cells with significant aberrations found by this coarse filter, we then performed a more sensitive test to compute the significance of aberrations in each window in each cell.

Empirical p-values and false discovery rates (FDRs) were computed by randomly permuting the arrangement of genes in the genome, as described below. In each of 100,000 permutations we randomly shuffle the labels of genes in the entire dataset, while preserving the genomic coordinates of genes (with each position having a new label each time) and the expression levels in each cell (so that each cell has the same expression values, but with new labels). We then compute either whole chromosome or subchromosomal aberration scores for each cell.

To identify whole-chromosome aberrations scores in each cell, we begin by calculating the sum of expression levels in 25Mbp sliding windows along each chromosome, with each window sliding 1Mbp so that it overlaps the previous window by 24Mbp. For each window in each cell, we then calculate the Z-score of the net expression, relative to the same window in all other cells. We then count the fraction of windows on each chromosome with an absolute value Z-score > 2. This fraction serves as the whole-chromosome aberration score for each chromosome in each cell. To assign a p-value to the whole-chromosome score for cell(i) chromosome(j), we calculate the empirical probability that the score for cell(i) chromosome(j) in the randomly permuted data was at least as large as the score in the original data.

Subchromosomal aberration scores were computed as follows. We begin by identifying the 20% of genes with the most uniform expression across the entire dataset. This is done by calculating the Shannon Diversity $e^{-\sum_g E_{gc} \ln E_{gc}}$ for each gene g (where E_{gc} is the expression matrix as defined above in **Preparation of expression matrices**), and taking the 20% of genes with the largest values. Using these genes, we subset the expression matrix and renormalize by TPM, and then compute in each cell the sum of expression in sliding windows of 25 consecutive genes, with each window sliding by one gene and overlapping the previous window (on the same chromosome) by

24 genes. In each window, we calculate the Z-score relative to all cells at day 0. The net (coarse filter) subchromosomal aberration score for a cell is calculated as the l2-norm of the Z-scores across all windows. To assign a p-value to the subchromosomal aberration score for cell(i), we calculate the empirical probability that the score for cell(i) in the randomly permuted data was at least as large as the score in the original data.

Finally, to identify the specific region(s) of genomic aberrations in each cell, we conduct a more sensitive test using just the cells in the stromal and trophoblast regions. Again using 25 housekeeping gene windows, we compute the average z-score of gene expression for genes in each window in each cell. We then compare the scores in all windows in all cells to similar scores computed for each cell in 100,000 random permutation trials, and then assign p-values based on the frequency of extremely high (gain) or low (loss) expression values.

For each of the aberration scores and associated p-values described above, we controlled for multiple hypothesis testing by calculating FDR q-values, using a false discovery threshold of 10%.

We tested the sensitivity and specificity of our method using labeled data from Tirosh et al 2016 (**Figure S4C**).

QUANTIFICATION AND STATISTICAL ANALYSIS

I. Analyzing the stability of optimal transport

To test the stability of our optimal transport analysis to perturbations of the data and parameter settings, we downsampled the number of cells at each time point, downsampled the number of reads in each cell, perturbed our initial estimates for cellular growth and death rates, and perturbed the parameters for entropic regularization and unbalanced transport. We found that our geodesic interpolation results are stable to a wide range of perturbations, summarized in the following table:

Number of cells per batch	**Number of UMIs Per cell**	**Max Growth** β_{MAX}	**Min Growth** β_{MIN}	**Max Death** δ_{MAX}	**Min Death** δ_{MIN}	**Entropy regularization** ϵ	**Unbalanced transport** λ
Down to: 200	Down to: 1000	33 hrs to 5.5 hrs	None to 9.5 hrs	33 hrs to 5.5 hrs	None to 9.5hrs	5×10^{-5} to 0.5	0.1 to 32

To generate this table, we ran geodesic interpolation with all but one of these settings fixed to default values. The default parameter values that we used are:
$\epsilon = 0.05, \lambda_1 = 1, \lambda_2 = 50, \beta_{MAX} = 1.7, \delta_{MAX} = 1.7, \beta_{MIN} = 0.3, \delta_{MIN} = 0.3.$
Moreover, by default we use all reads per cell and all cells per batch.

II. Benchmarking: comparing to other trajectory inference methods

We compared Waddington-OT to other trajectory inference methods. While many algorithms have been proposed to recover trajectories from single cell RNA-seq data, Waddington-OT is unique in its ability to model cellular growth, death and development over time. The benchmarking results below demonstrate that these features are crucial for accurate analysis: the other approaches considered fail in key respects because they do not leverage measured information about time, or because they do not model cellular growth and death rates.

1. Categorizing single cell trajectory inference methods

We comprehensively reviewed 62 methods — consisting of 59 methods noted in the recent review by Saelens et al 2018, plus three more recent methods: FateID (Herman et al., 2018), STITCH (Wagner et al., 2018), and URD (Farrell et al., 2018).

The methods fall into four categories:

(1) methods that are not applicable to developmental time courses with scRNA seq— because they do not handle branching trajectories or apply only to systems at equilibrium;
(2) methods that do not use information about the time of collection;
(3) methods that use information about time of collection, but do not model cell growth rates over time;

From each category, we selected several of the best (most widely used) methods and applied them to our data.

Category	Defining feature	Number in category	Methods tested
Category 1	Not applicable to developmental time courses	33	None (because not applicable)
Category 2	Does not use information about time of sampling	25	FateID, URD, Approximate Graph Abstraction, Monocle2
Category 3	Uses information about sampling time, but does not model growth	4	STITCH, GPfates, scDiff

We describe the performance:

Category 1. (33 methods). These methods cannot be used to analyze developmental time courses.

Category 2. (25 methods). All the tested methods in category 2 produce trajectories that are inconsistent with the time course, make huge leaps across time points and in some cases go backward in time in the sense that late time point cells are inferred to be at early time point.
For example, Monocle2 produces trajectories with highly inconsistent temporal ordering — with Day 0 cells giving rise to Day 18 cells, which then give rise to Day 8 cells.

Category 3. (4 methods). All of the tested methods in category 3 are thrown off by the much higher growth rate of certain cell types (e.g., iPSCs) than others (e.g., apoptotic stromal cells). In order to account for the increase in iPSCs, the methods infer that a large fraction of apoptotic stromal cells must transition to iPSCs.

In addition, two of the methods (GPfates, scDiff) produced trajectories to incoherent final destinations (that is, sets composed of mixtures of radically different cell types).

2. Benchmarking details

2.1 Category 2 results

Monocle2. This program (Qiu et al., 2017) computes a graph embedding of scRNA-seq data. Applied to our data, Monocle2 produces a graph consisting of 5 segments (**Figure S7A**). The trajectories are problematic in several respects. First, the trajectories disagree with known information about time. For example, they put day 18 Stromal cells together with Day 0 MEFs at the root of the tree (Branch 1). This gives rise to a branch (Branch 3) consisting of a group of cells spanning days 1.5 to 8 that give rise to a subsequent branch (Branch 4) consisting of a group of cells from day 4 – 9. So, the progression is out of order (with day 18 cells giving rise to day 8 cells which then give rise to day 4 cells). Second, Monocle2 fails to distinguish iPS, Neuronal, and Trophoblast fates as distinct destinations: these populations are all assigned to a common branch (Branch 5). These problems appear to be due to the fact that the method does not leverage known information about time, and because its fully unsupervised approach does not identify meaningful cell sets in the data.

URD. This program (Farrell et al., 2018) computes a tree connecting a set of root cells to a set of terminal destinations by performing a large number of random walks. Applied to our data (40,000 serum cells, 1,000 per timepoint) with Day 18 iPSCs, Stromal, Neural, and Trophoblasts as terminal destinations, URD inferred a tree consisting of 7 segments (**Figure S7B**). The trajectories are problematic in several respects. First, fates are determined unreasonably early: the trophoblast lineage is specified by day 0.5 and all branches are specified by day 2. Second, URD predicts that the Neural and iPS lineages arise from Stromal cell set, which is unlikely because the Stromal population expresses signatures of senescence and apoptosis. Third, URD fails to assign over half of all cells to any trajectory. Over 85% of cells from days 4 through 8 are not assigned to any trajectory (96% of cells from day 6 and 94% from day 7). These problems appear to arise due to the failure to incorporate temporal information and to model rates of cellular growth and death. (It might be possible to modify the random walks of URD to account for this).

FateID. This program (Herman et al., 2018) takes as input a set of terminal destinations and computes a "fate-bias probability" for each cell by iteratively classifying cells with a random-forest classifier. When we applied it to our data (2i conditions), FateID showed serious problems with the trajectories (**Figure S7C**). First, the fates of iPSCs, Trophoblast, and Stromal remain divergent through the beginning of the time-course (cells do not seem to share a common ancestor at day 0). Second, the trajectories are inconsistent with the temporal information in the sense that trajectories essentially skip over time points. For example, the Stromal trajectory effectively leaps over days 3 through 5, and the iPSC and Stromal trajectories do not contain any cells on day 0.

These behaviors are likely due to the fact that FateID does not leverage time-course information in its present formulation. (It might be possible to modify FateID to connect individual pairs of time-points, as in our optimal transport approach).

Approximate graph abstraction. This program (Wolf et al., 2017) connects clusters to identify a graphical representation of trajectories. We ran the method to connect 65 clusters in our data (2i conditions). The clusters are visualized in the left pane of **Figure S7D** and the connections inferred by AGA are in the right pane below. The program yielded trajectories that are clearly inconsistent with the temporal information – for example, with cells of day 0 (cluster 1) going directly to late-stage Stromal cells at days 14 through 18 (clusters 63 and 58). In addition, AGA infers extensive transitions from the Stromal region to the iPSC region; this is not biologically plausible because the Stromal cells express strong senesce programs. These problems appear to arise due to the failure to incorporate temporal information and to model rates of cellular growth and death.

2.2 Category 3 results

STITCH. This method was developed by (Wagner et al., 2018), in an application to zebrafish embryonic development. The method constructs a k-NN graph within the cells at each time point and then stitches these together by connecting various cells from adjacent time points. **Figure S7E** shows the resulting graph when applied to our reprogramming data (2i conditions). The STITCH graph shows iPSCs are largely arising from the Stromal region (that is, the majority of edges connecting to the iPSC region come from the Stromal region). This inference is biologically implausible, as the Stromal cells express strong signatures of senescence and apoptosis. This method appears to fails on our data because it does not model the rapid proliferation of iPSCs — and thus concludes that iPSCs at later time points must come from other sources. (It might be possible to modify STITCH to incorporate cell growth by connecting each cell to a different number of neighbors, based on an estimate of growth).

scDiff. This method (Rashid et al., 2017) produces a tree of clusters by clustering cells at each time point, moving cells between time points to account for asynchronicity, and assigning to each cluster a single parent cluster. Applied to our data (serum conditions), the method fails to identify iPS, Neural, Trophoblast and Stromal as coherent categories. It produces a tree with 54 leaves, only 4 of which consist of day 18 cells. Some of the leaves consist of day 2 cells. The method appears to fail on our data because its fully unsupervised approach fails to identify meaningful cell sets.

GPfates. This method (Lönnberg et al., 2017) identifies trajectories by fitting a mixture of Gaussian processes to model a set of branching trajectories over time. Applied to our data (2i conditions), GPfates identifies trajectories to incoherent locations (**Figure S7F**). Multiple trajectories lead to cells sets containing both iPS and Stromal cells. This implies that iPSCs have significant ancestry in the Stromal region, where apoptotic and senescent programs are highly expressed. The method appears to fail on our data because its fully unsupervised approach does not identify meaningful cell sets and it does not model cell growth.

III. Sampling bias

In principle, sampling bias could be introduced in sample preparation (in which trypsinized cells are filtered to remove clumps prior to encapsulating the single cell suspension) or in single cell library preparation. To determine whether the proportion of cell types observed in our single-cell data accurately reflected the proportion of cell types in the biological sample, we performed two experiments.

First, we examined the effect of the filtering process by comparing bulk RNA-seq profiles of material collected before and after filtering. Samples were collected in triplicate at days 4, 8, 12, 14, and 16 in serum and 2i conditions. To test the effect of filtering, we compared the correlations between groups (prefiltered and post-filtered) to the variation within each group. We observed that the pre- and post-filtered samples were indistinguishable at all time-points, with the exception of day 16 in serum conditions (for which the pre- *vs*. post- correlation is lower than the pre- *vs*. pre- correlation and the post- *vs*. post- correlation.

Second, we examined the effect of the overall process, including both sample and library preparation. We collected bulk RNA-seq profiles directly from cells in the plate on days 12 and 16 in both 2i and serum (4 profiles). We compared these profiles to additional scRNA-seq data collected in singlicate at these days and conditions, as well as to the scRNA-seq data collected in duplicate in our main experiment (12 profiles, of which one was discarded as discordant with all of the time points in our main experiment). We examined whether the cell type proportions in the single-cell data were consistent with the bulk RNA-seq profile, based on gene signatures of each cell type. The results were consistent at all time-points, with the exception of day 16 in serum conditions (at which trophoblasts appear to be underrepresented by ~3-fold in the single-cell data).

To test whether such an underrepresentation of trophoblasts at day 16 in serum conditions would have an effect on our inferred trajectories, we reweighted the empirical distributions in our optimal transport framework and repeated our analyses. Because the reprogramming process was essentially complete by day 16, the reweighting had no impact on any of our biological conclusions (and had no significant on the optimal transport results apart from slightly increasing transitions to stromal cells from day 16 to day 18).

IV. Pilot study

In our pilot study, we collected 65,000 expression profiles over 16 days at 10 distinct time points (and 9 in serum). We compare results from the larger study to the pilot study in **Figure S1B,C**, where we show trends in expression along trajectories to each major cell set: iPSCs, Neural-like, Trophoblast-like (placenta-like in pilot), and Stromal. We find that the expression trends are reasonably similar. Moreover, by comparing the ancestor divergence plots for the two studies, we find that in both studies the stromal population gradually diverges early in the time course and there is a sharp divergence of iPSC from Neural and Trophoblast just after removal of Dox at day 8.

DATA AND SOFTWARE AVAILABILITY

We have uploaded our data to NCBI Gene Expression Omnibus. The identification number is:

Single cell RNA-seq raw data	GSE122662

Our data is also available on the Broad Single Cell Portal:

https://portals.broadinstitute.org/single_cell/study/optimal-transport-analysis-of-ipsc-reprogramming

Our software package is available on GitHub:

https://github.com/broadinstitute/wot

ADDITIONAL RESOURCES

We have developed an interactive software package complete with simulated examples and tutorials:

https://broadinstitute.github.io/wot/

Supplemental Information

SUPPLEMENTAL FIGURE LEGENDS

Figure S1. Related to Figure 2: Validation, stability, and comparison to pilot study.

(**A**) Bright field images of day 2 (Phase1-(Dox)), day 4 (Phase1-(dox)) and day 18 cells during reprogramming in (Phase-2(2i)) and (Phase-2(serum)) culture conditions. BF (bright field). GFP (Oct4-GFP). (**B-C**) Comparison to pilot dataset. (**B**) Trends in signature scores along ancestor trajectories to iPSC, Stromal, Neural, and Trophoblast cell sets. Trends for the pilot dataset are shown with open circles and trends for the large dataset are shown with solid lines. (**C**) Shared ancestry results for pilot dataset (solid lines) and for the larger dataset (dashed lines). (**D,E,F**) Validation by geodesic interpolation for serum conditions over 2-day intervals (**D**), for 2i over 1-day intervals (**E**). As in Figure 2J (which shows serum over 1-day intervals), the red curve shows the performance of interpolating held-out time points with optimal transport. The green curve shows the batch-to-batch Wasserstein distance for the held-out time points, which is a measure of the baseline noise level. The blue and teal curves show the performance of two null models: interpolating according to the independent coupling including growth (blue) or without growth (teal). (**F**) Validation by geodesic interpolation for serum conditions over 1-day intervals with alternate null models. The purple curve shows the distance between the third time point and the middle time point, and the orange curve shows the distance between the first time point and the middle time point. (**G,H,I**) Unbalanced transport can be used to tune growth rates. (**G**) When the unbalanced regularization parameter is large (λ =16), growth constraints are imposed strictly, and the input growth (x-axis; determined by gene signatures- see STAR Methods) is well-correlated to the output growth (y-axis; implicit growth rate determined from the transport map). (**H**) When the unbalanced parameter is small (λ =1), the growth constraints are only loosely imposed, allowing implicit growth rates to adjust and better fit the data. (**I**) The correlation of output vs input growth as a function of λ.

Figure S2. Related to Figure 3: Divergence of Stromal and MET fates during the initial stages of reprogramming.

(**A**) Cells from the stromal region were re-embedded by FLE, and scored for signatures of long-term cultured MEFs (left) or stromal cells in the embryonic mesenchyme (right) found in the Mouse Cell Atlas. (**B**) Day 0 MEFs (D0; black dots) we re-embedded together with cells from the stromal set (red dots) in a TSNE plot. (**C**) The Stromal region is a terminal destination as evidenced by (1) the large flow of cells into the region around day 9 (green spike, first and second panels) and (2) essentially zero flow out of the region (blue curves, first and second panels). By contrast, the MET region is a transient state as evidenced by the blue curves in the right two panels showing significant transitions out of MET. (**D**) *Fut9*+ and *Shisa8*+ expression patterns visualized in a fate-divergence layout. Each dot represents a single cell, colored by expression of either *Fut9* (left) or *Shisa8* (right). The x-axis shows time of collection and the y-axis shows the log-likelihood ratio of obtaining MET vs Stromal fate, as predicted by optimal transport. (**E**) Ectopic OKSM expression levels are predictive of MET fate. The y-axis shows correlation between OKSM

expression and the log-likelihood of obtaining MET fate. Color (red vs blue) distinguishes the two batches at each time point (x-axis).

Figure S3. Related to Figure 4: iPSCs.

(**A**) False discovery rate q-values for expression of 2 cell signatures on iPSC-specific FLE. (**B**) Heatmap showing trends in expression of 1479 variable genes (STAR-Methods) along the ancestor trajectory to iPSCs. Color indicates fold-change in expression relative to day 0 (white). Each row shows the mean expression trend for a single gene, where the mean is computed with respect to the ancestor distribution. Genes are clustered into groups with similar trends. Terms on the right indicate significant gene set enrichment (GSEA, all adjusted p-values < 0.01) in one of several databases (M, MSigDB; BP, GO biological process; W, WikiPathways; C, chromosome; CC, GO cellular component).

Figure S4. Related to Figure 5: Trophoblast and Neural subtypes.

(**A**) Expression of individual marker genes (red color bars, log(TPM +1); see also Table S2) for each subtype on the trophoblast FLE (as in Figure 5C). TP, trophoblast progenitors; SpA-TGC, spiral artery trophoblast giant cells; SpTB, spongiotrophoblasts; LaTB, labyrinthine trophoblasts. (**B**) Cells with a gene signature of extra-embryonic endoderm (XEN) arise in a single batch on day 15.5 (red color bar, average z-score). (**C**) Performance of CNV inference. Shown are precision and recall precision and recall at an FDR of 10% (intersecting red lines) for our CNV inference in published scRNA-Seq data that include annotated, clonal CNVs. (**D-F**) Cells in the neural region were re-embedded by tSNE and annotated with various features. (**D**) Marker gene expression (red color bar, log(TPM + 1)) of neural subtypes on the neural tSNE. OPC refers to oligodendrocyte precursor cells. (**E**) Cells with significant expression (black dots) of indicated signatures from the Allen Mouse Brain Atlas on the neural tSNE at an FDR of 10%. (**F**) Cells in the neural region present from days 12.5-14.5 (left) or days 17-18 (right).

Figure S5. Related to Figure 6: Temporal patterns of paracrine signaling.

(**A**) Temporal pattern of the net potential for paracrine signaling between contemporaneous cells in 2i condition. Each dot represents the aggregated interaction score across all ligand-receptor pairs for a given combination of clusters from (**B**) (see STAR Methods for details). (**B**) Cell clusters determined by Louvain-Jaccard community detection algorithm. (**C**-**E**) Changes in the standardized interaction scores for top ligand-receptor pairs between ancestors of stromal cells and ancestors of iPSCs (**C**), neural-like cells (**D**), and trophoblast cells (**E**).

Figure S6. Related to Figure 7: Impact of *Obox6* + and GDP9 on reprogramming

(**A-C**) Log-likelihood ratio of obtaining iPSC vs non iPSC fate on each day (x-axis) in serum. *Obox6*$^{+}$ cells in red. (**D**) Percentage of Oct4-EGFP^{+} cells at day 16 of reprogramming from secondary MEFs by lentiviral overexpression of *Oct4, Klf4, Sox2*, and *Myc* (OKSM) combined with either *Zfp42, Obox6*, or an empty control, in either 2i or serum conditions. Oct4-EGFP^{+} cells were measured by flow cytometry. Plot includes the percentage of Oct4-EGFP^{+} cells in three

biological replicates (for *Zfp42* and *Obox6* overexpression, or an empty control) from five independent experiments (Exp). (**E, F**) Number of Oct4-EGFP^{+} colonies at day 16 of reprogramming from primary MEFs by lentiviral overexpression of individual *Oct4, Klf4, Sox2*, and *Myc* combined with either *Zfp42*, *Obox6*, or an empty control in (**E**) 2i and (**F**) serum conditions. Plot includes the number of Oct4-EGFP^{+} cells in three biological replicates (for *Zfp42* and *Obox6* overexpression, or an empty control) from two independent experiments (Exp). (**G**) The number of Oct4-EGFP^{+} cells at day 15 of reprogramming from four independent experiments (Exp) where mouse recombinant GDF9 were added at three different concentration. (**H,I**) Impact of GDF9 on cell proportions. (**H**) tSNE of day 15 cell profiles collected in serum condition supplemented with GDF9 (1 μg/ml) and controls from four independent experiments. Cells are colored by five cell sets by graph-clustering. (**I**) Proportion of cells from each cluster in (**H**) in each experiment.

Figure S7. Related to Figure 2: Benchmarking analysis

(A) Monocle2 computes a graph upon which each cell is embedded. The graph, which consists of 5 segments, is visualized in the upper-left pane. The 5 segments are visualized on our FLE in the 5 remaining panels of (**A**). Segment 1 (green) consists of day 0 cells together with day 18 Stromal cells. Segments 2 and 3 consist of cells from day 2 - 8 that supposedly arise from Segment 1 cells. Segment 3 gives rise to Segments 4 (purple) and 5 (red). Segment 4 contains the cells we identify as on the MET region and Segment 5 contains the iPSCs, Trophoblasts, and Neural populations, which Monocle2 infers come directly from the non-proliferative cells in segment 3. (**B**) The URD tree is displayed in the first panel, and the 7 segments are numbered and color coded. Each remaining panel displays the cells from a single segment on the FLE. Segment 1 (magenta) contains the day 0 MEF cells. The first bifurcation occurs on day 0.5, where segment 2 (consisting of day 0.5 cells) splits off from segment 3 (consisting of day 12-18 Stromal cells). Segment 2 splits to give rise to Segment 4 (consisting of day 2 cells) and Segment 5 consisting of day 12-18 Trophoblasts and Epithelial cells. Segment 4 splits on day 3 to give rise to Segment 6 (consisting of a diverse population including day 3 cells and day 14-18 iPSCs) and Segment 7 (consisting of a diverse population including day 3 cells and day 12-18 Neural-like cells). (**C**) The fate bias probabilities computed by FateID visualized on our FLE. Color: fate bias probability in barycentric coordinates. Pure green falls near the Trophoblast vertex in the triangular legend and represents 100% chance of Trophoblast fate, while teal, which falls on the edge of the triangle between Trophoblast and Stromal, represents 50% likelihood for each of these two fates and 0% for iPSC. Black points (at the center of the barycentric triangle) have an equal chance of obtaining any of the three fates. Note that bright green and red colors exist before day 8, indicating early fate specification, and note that Day 0 is essentially all blue but there are essentially no blue cells near day 3.5. (**D**) Our clusters are visualized on the left and the graph computed by Approximate Graph Abstraction is on the right. Note that cluster 1 connects to cluster 58. (**E**) The STITCH graph visualized on our FLE. Cells are colored by time of collection and edges of the STITCH graph are indicated with lines connecting cells. An abundance of edges connects the Stromal region to the iPSC region. (**F**) The 3 trajectories inferred by GPfates. Trajectories 2-3 all terminate in both the Stromal and iPSC region.

Figure S1

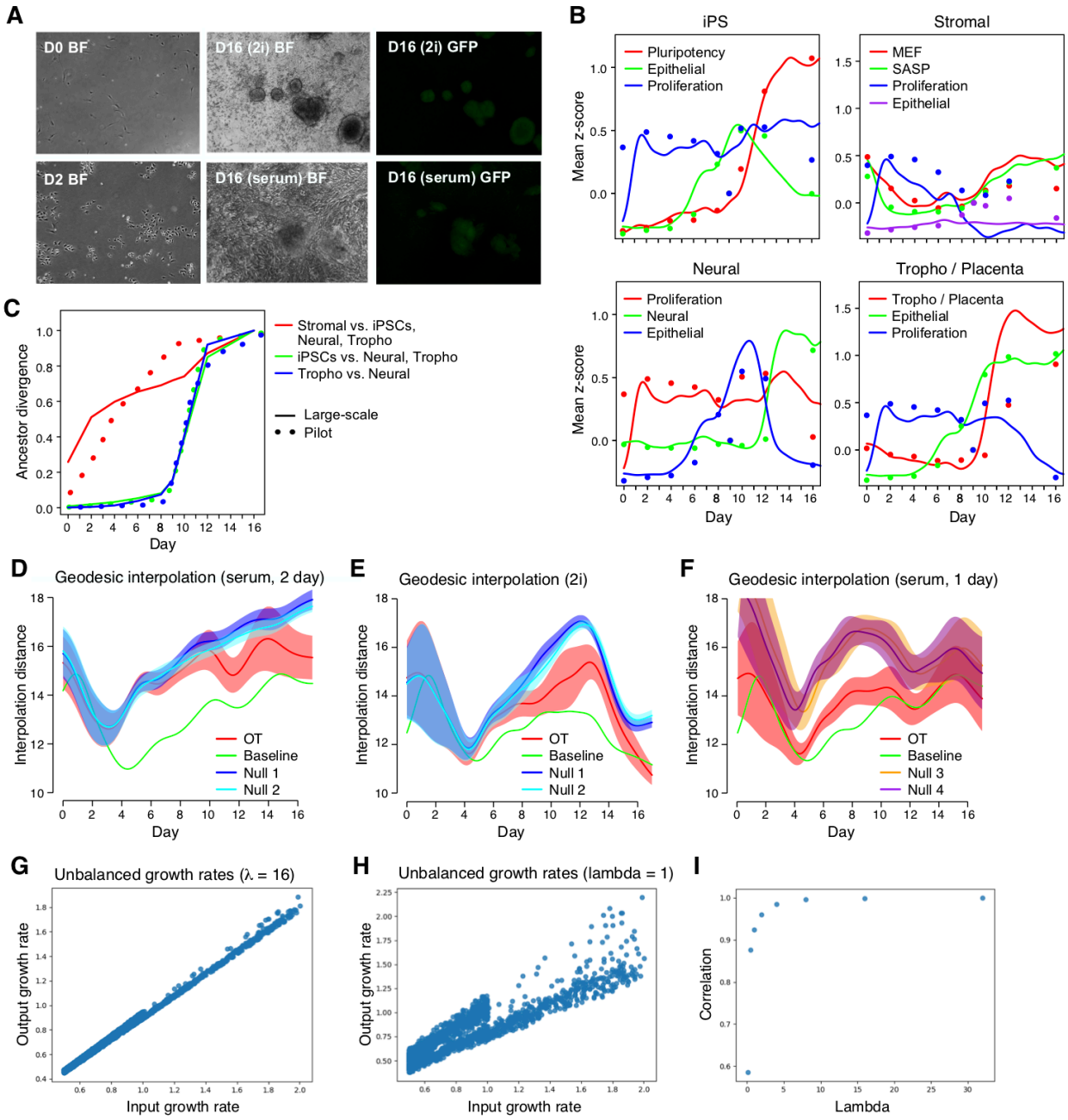
A
D0 BF
D16 (2i) BF
D16 (2i) GFP
D2 BF
D16 (serum) BF
D16 (serum) GFP
B
iPS
Pluripotency
Epithelial
Proliferation
Stromal
MEF
SASP
Proliferation
Epithelial
Neural
Proliferation
Neural
Epithelial
Tropho / Placenta
Tropho / Placenta
Epithelial
Proliferation
Mean z-score
Day
C
Ancestor divergence
Stromal vs. iPSCs, Neural, Tropho
iPSCs vs. Neural, Tropho
Tropho vs. Neural
Large-scale
Pilot
Day
D
Geodesic interpolation (serum, 2 day)
Interpolation distance
OT
Baseline
Null 1
Null 2
Day
E
Geodesic interpolation (2i)
Interpolation distance
OT
Baseline
Null 1
Null 2
Day
F
Geodesic interpolation (serum, 1 day)
Interpolation distance
OT
Baseline
Null 3
Null 4
Day
G
Unbalanced growth rates (λ = 16)
Output growth rate
Input growth rate
H
Unbalanced growth rates (lambda = 1)
Output growth rate
Input growth rate
I
Correlation
Lambda

Figure S2

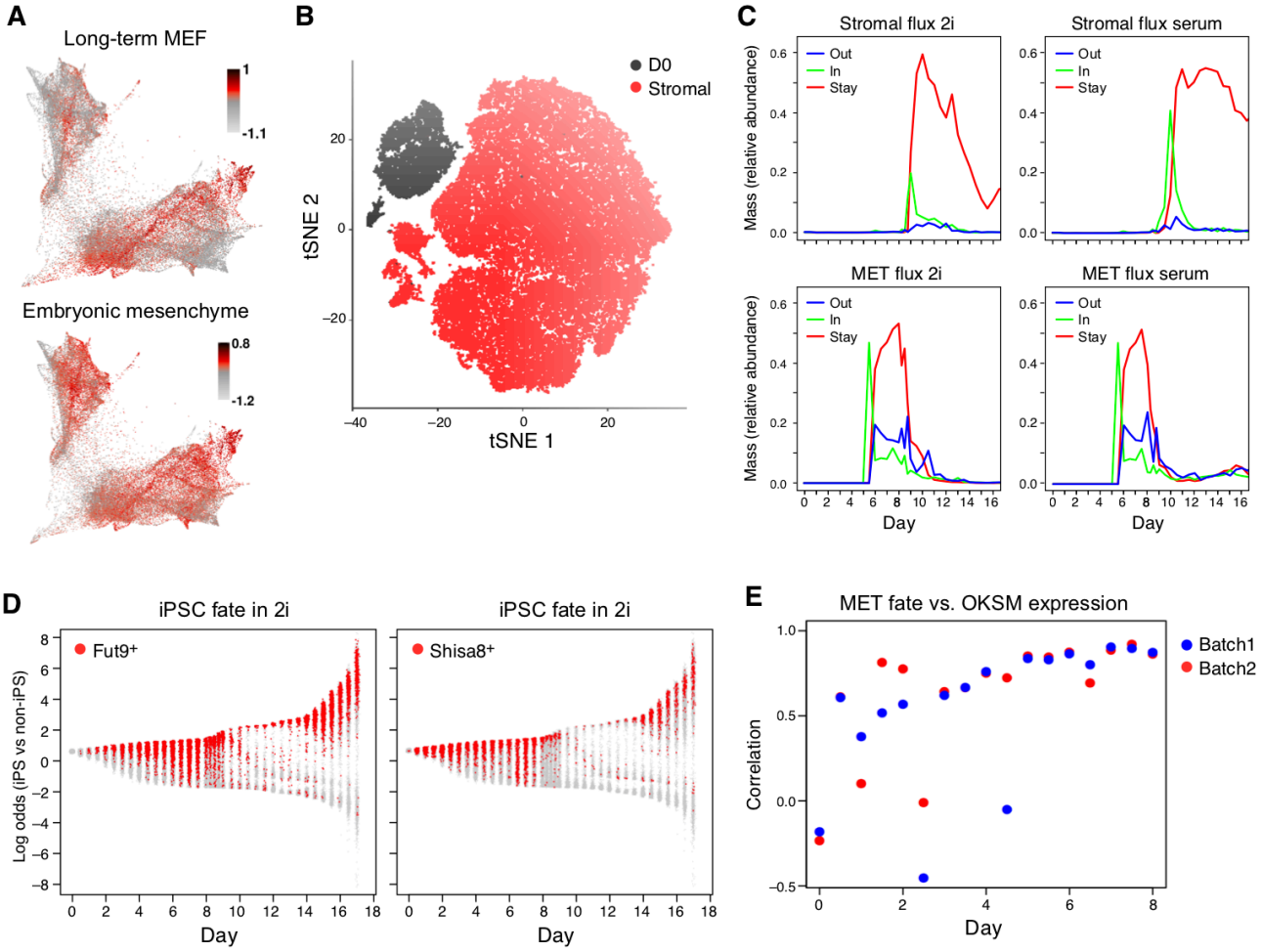
A
Long-term MEF
1
-1.1
Embryonic mesenchyme
0.8
-1.2
B
D0
Stromal
tSNE 2
tSNE 1
C
Stromal flux 2i
Stromal flux serum
MET flux 2i
MET flux serum
Out
In
Stay
Mass (relative abundance)
Day
D
iPSC fate in 2i
iPSC fate in 2i
Fut9+
Shisa8+
Log odds (iPS vs non-iPS)
Day
E
MET fate vs. OKSM expression
Batch1
Batch2
Correlation
Day

Figure S3

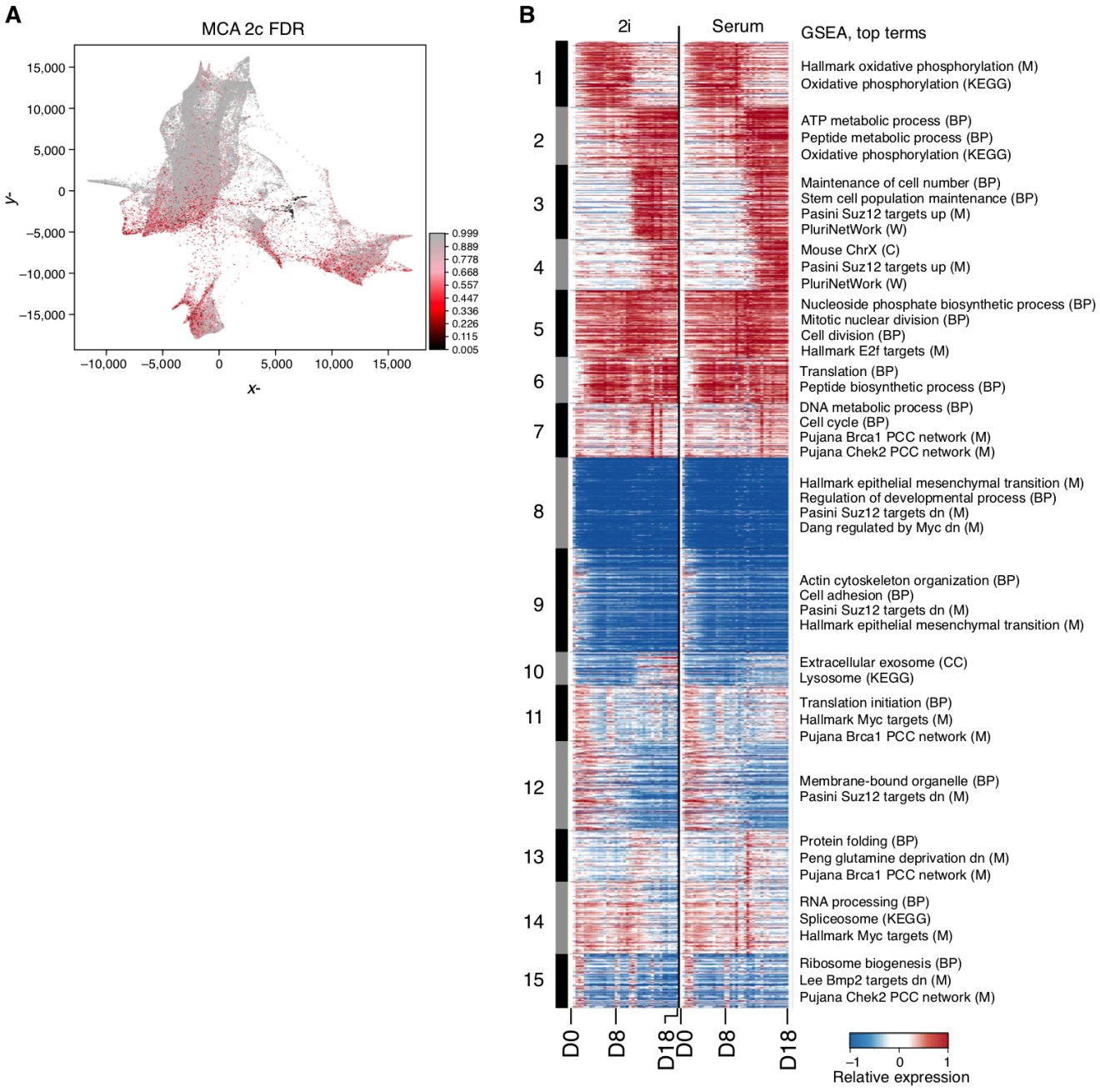
A
MCA 2c FDR
15,000
10,000
5,000
0
−5,000
−10,000
−15,000
y-
−10,000
−5,000
0
5,000
10,000
15,000
x-
0.999
0.889
0.778
0.668
0.557
0.447
0.336
0.226
0.115
0.005
B
2i
Serum
GSEA, top terms
1
Hallmark oxidative phosphorylation (M)
Oxidative phosphorylation (KEGG)
2
ATP metabolic process (BP)
Peptide metabolic process (BP)
Oxidative phosphorylation (KEGG)
3
Maintenance of cell number (BP)
Stem cell population maintenance (BP)
Pasini Suz12 targets up (M)
PluriNetWork (W)
4
Mouse ChrX (C)
Pasini Suz12 targets up (M)
PluriNetWork (W)
5
Nucleoside phosphate biosynthetic process (BP)
Mitotic nuclear division (BP)
Cell division (BP)
Hallmark E2f targets (M)
6
Translation (BP)
Peptide biosynthetic process (BP)
7
DNA metabolic process (BP)
Cell cycle (BP)
Pujana Brca1 PCC network (M)
Pujana Chek2 PCC network (M)
8
Hallmark epithelial mesenchymal transition (M)
Regulation of developmental process (BP)
Pasini Suz12 targets dn (M)
Dang regulated by Myc dn (M)
9
Actin cytoskeleton organization (BP)
Cell adhesion (BP)
Pasini Suz12 targets dn (M)
Hallmark epithelial mesenchymal transition (M)
10
Extracellular exosome (CC)
Lysosome (KEGG)
11
Translation initiation (BP)
Hallmark Myc targets (M)
Pujana Brca1 PCC network (M)
12
Membrane-bound organelle (BP)
Pasini Suz12 targets dn (M)
13
Protein folding (BP)
Peng glutamine deprivation dn (M)
Pujana Brca1 PCC network (M)
14
RNA processing (BP)
Spliceosome (KEGG)
Hallmark Myc targets (M)
15
Ribosome biogenesis (BP)
Lee Bmp2 targets dn (M)
Pujana Chek2 PCC network (M)
D0
D8
D18
D0
D8
D18
−1
0
1
Relative expression

Figure S4

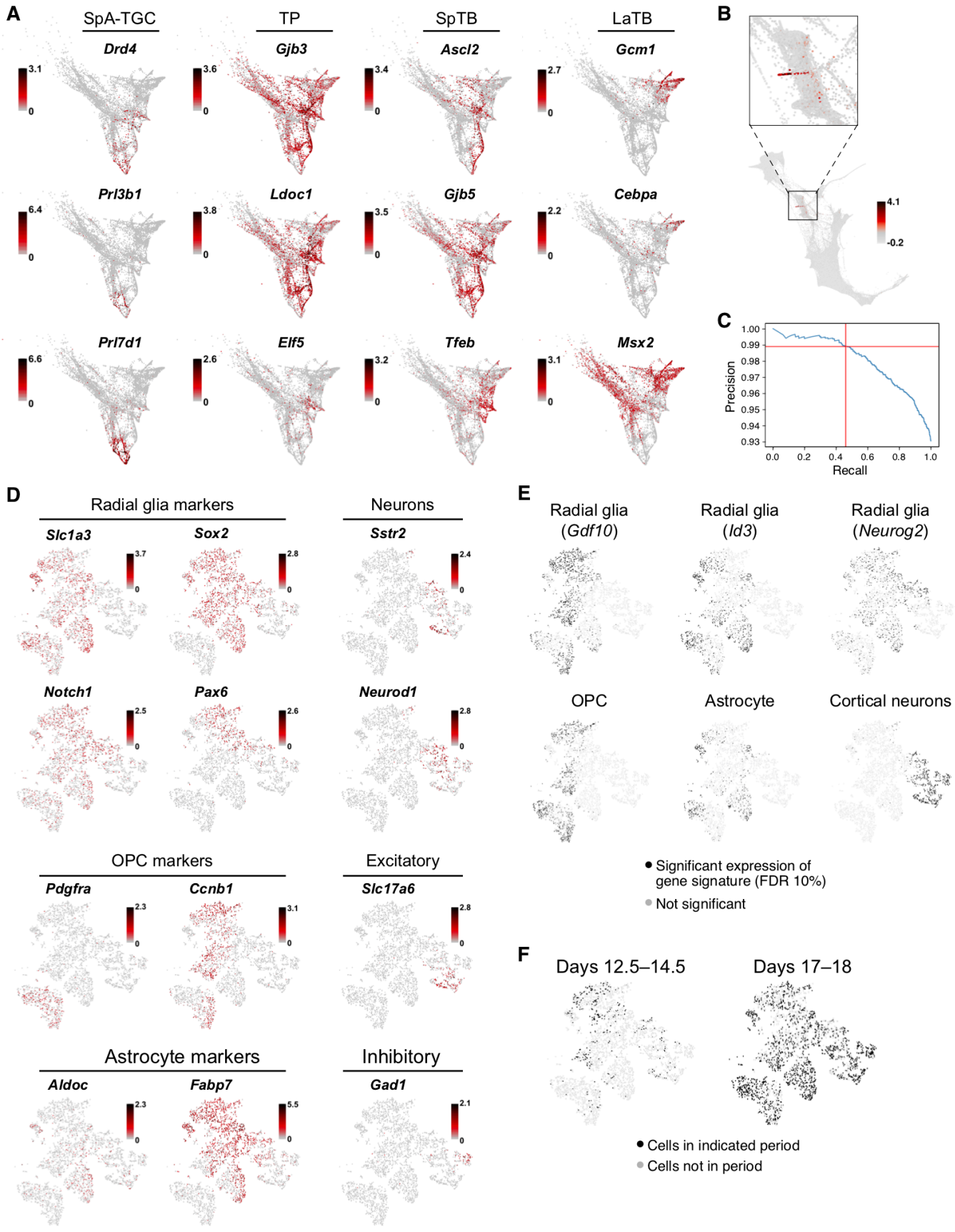
A
SpA-TGC
TP
SpTB
LaTB
Drd4
Gjb3
Ascl2
Gcm1
Prl3b1
Ldoc1
Gjb5
Cebpa
Prl7d1
Elf5
Tfeb
Msx2
B
4.1
-0.2
C
Precision
Recall
D
Radial glia markers
Neurons
Slc1a3
Sox2
Sstr2
Notch1
Pax6
Neurod1
OPC markers
Excitatory
Pdgfra
Ccnb1
Slc17a6
Astrocyte markers
Inhibitory
Aldoc
Fabp7
Gad1
E
Radial glia (Gdf10)
Radial glia (Id3)
Radial glia (Neurog2)
OPC
Astrocyte
Cortical neurons
Significant expression of gene signature (FDR 10%)
Not significant
F
Days 12.5–14.5
Days 17–18
Cells in indicated period
Cells not in period

Figure S5

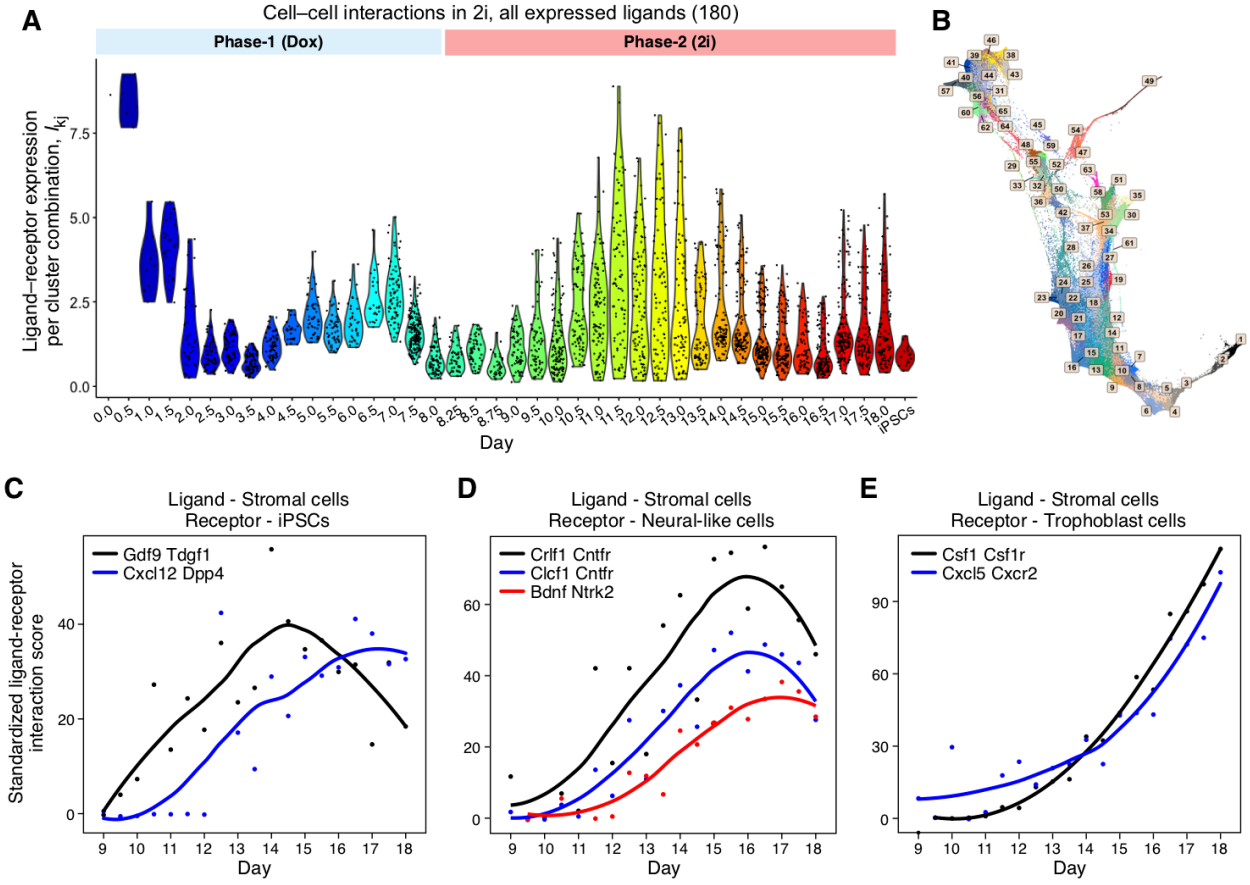
A
Cell–cell interactions in 2i, all expressed ligands (180)
Phase-1 (Dox)
Phase-2 (2i)
Ligand–receptor expression per cluster combination, I_{kj}
Day
iPSCs
B
C
Ligand - Stromal cells
Receptor - iPSCs
Gdf9 Tdgf1
Cxcl12 Dpp4
Standardized ligand-receptor interaction score
Day
D
Ligand - Stromal cells
Receptor - Neural-like cells
Crlf1 Cntfr
Clcf1 Cntfr
Bdnf Ntrk2
Day
E
Ligand - Stromal cells
Receptor - Trophoblast cells
Csf1 Csf1r
Cxcl5 Cxcr2
Day

Figure S6

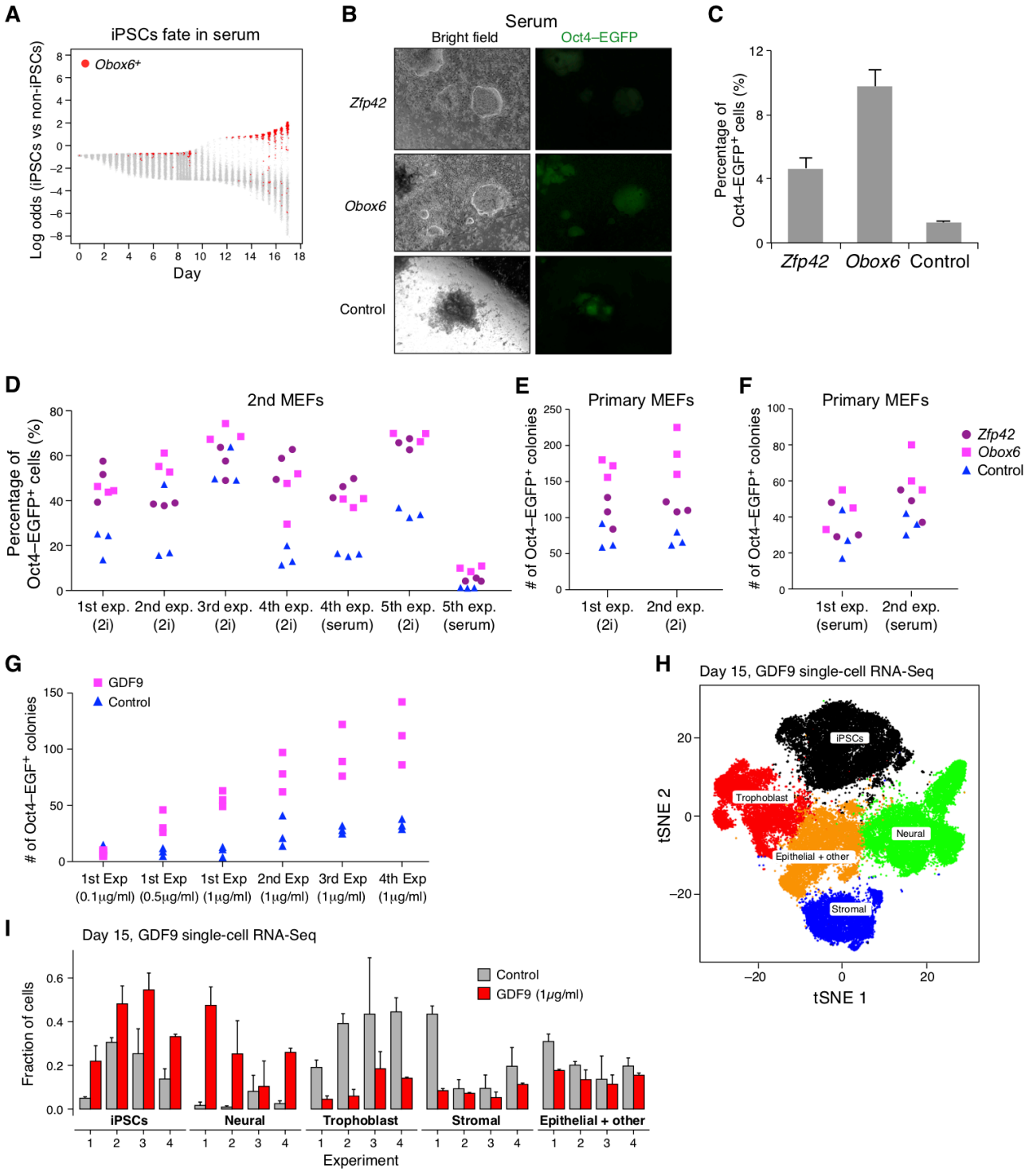
A
iPSCs fate in serum
Obox6+
Log odds (iPSCs vs non-iPSCs)
Day
B
Serum
Bright field
Oct4–EGFP
Zfp42
Obox6
Control
C
Percentage of Oct4–EGFP+ cells (%)
Zfp42
Obox6
Control
D
2nd MEFs
Percentage of Oct4–EGFP+ cells (%)
1st exp. (2i)
2nd exp. (2i)
3rd exp. (2i)
4th exp. (2i)
4th exp. (serum)
5th exp. (2i)
5th exp. (serum)
E
Primary MEFs
# of Oct4–EGFP+ colonies
1st exp. (2i)
2nd exp. (2i)
F
Primary MEFs
# of Oct4–EGFP+ colonies
Zfp42
Obox6
Control
1st exp. (serum)
2nd exp. (serum)
G
GDF9
Control
# of Oct4–EGF+ colonies
1st Exp (0.1μg/ml)
1st Exp (0.5μg/ml)
1st Exp (1μg/ml)
2nd Exp (1μg/ml)
3rd Exp (1μg/ml)
4th Exp (1μg/ml)
H
Day 15, GDF9 single-cell RNA-Seq
iPSCs
Trophoblast
Neural
Epithelial + other
Stromal
tSNE 2
tSNE 1
I
Day 15, GDF9 single-cell RNA-Seq
Control
GDF9 (1μg/ml)
Fraction of cells
iPSCs
Neural
Trophoblast
Stromal
Epithelial + other
Experiment

Figure S7

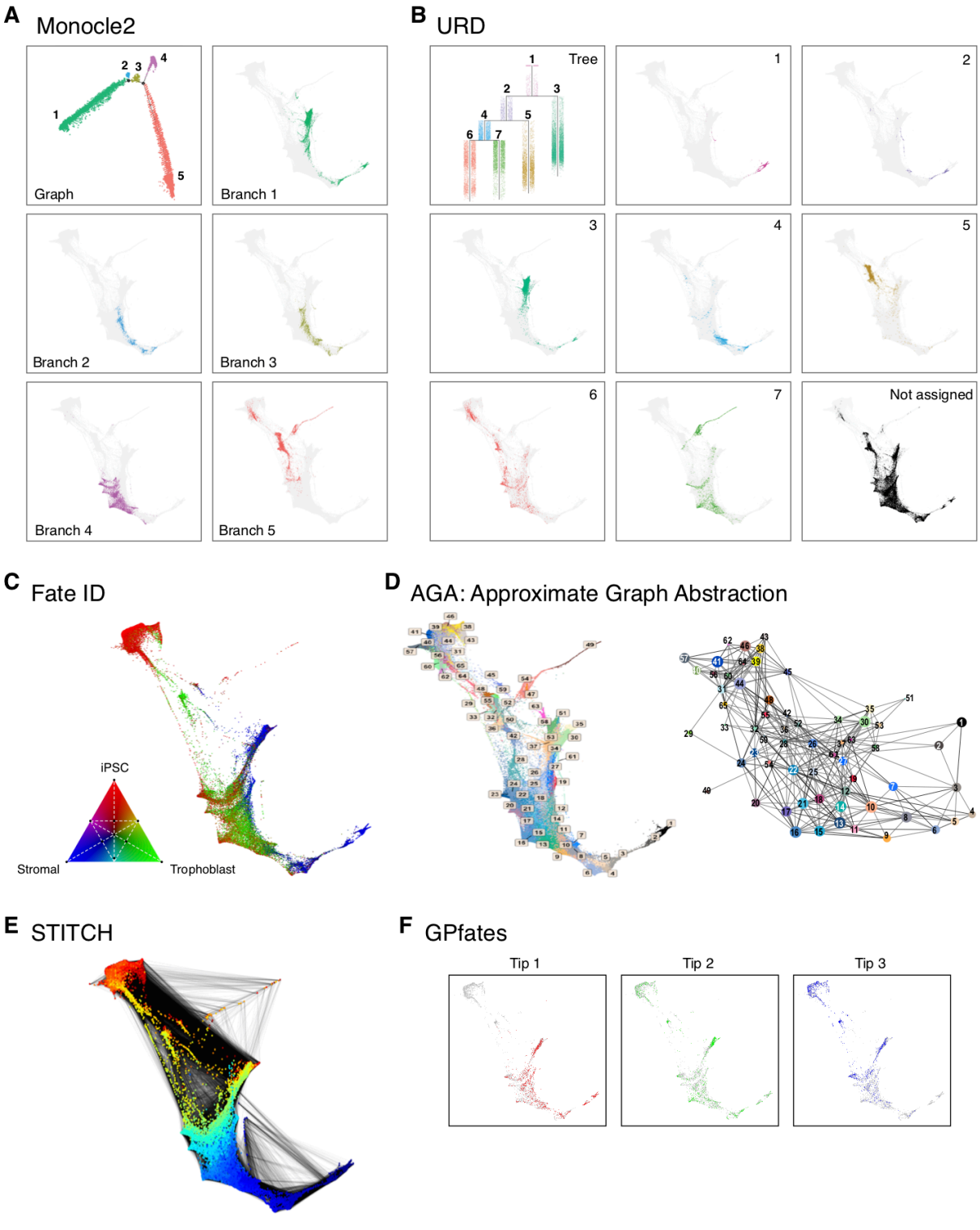
A
Monocle2
Graph
Branch 1
Branch 2
Branch 3
Branch 4
Branch 5
B
URD
Tree
1
2
3
4
5
6
7
Not assigned
C
Fate ID
iPSC
Stromal
Trophoblast
D
AGA: Approximate Graph Abstraction
E
STITCH
F
GPfates
Tip 1
Tip 2
Tip 3

Supplemental Tables

Table S1: Summary of single cell sequencing statistics and sample information.

Table S2: List of genes comprising gene signatures.

Table S3: Differential genes between top ancestors of MET vs. top ancestors of stromal cells.

Table S4: List of genes for 15 groups of genes along the successfully reprogrammed trajectory reported in Figure S3B

Table S5: Potential ligand-receptor pairs between stromal cells and iPSCs, neural-like cells, and trophoblast cells ranked by standardized interaction scores.

Table S6: Categorization of single cell trajectory inference methods.

Supplemental Movie

Movie S1: Visualizing the flow of cells through time in the FLE.